Micro Scale Lithium Ion Battery Modeling with the Finite Element Method

by

Miklos Zoller

A dissertation submitted in partial satisfaction of the

requirements for the degree of

Doctor of Philosophy

in

Civil and Environmental Engineering

in the

Graduate Division

of the

University of California, Berkeley

Committee in charge:

Professor Sanjay Govindjee, Chair
Professor Robert L. Taylor
Professor Nitash Balsara

Fall 2020

Micro Scale Lithium Ion Battery Modeling with the Finite Element Method

Abstract

Micro Scale Lithium Ion Battery Modeling with the Finite Element Method

by

Miklos Zoller

Doctor of Philosophy in Civil and Environmental Engineering

University of California, Berkeley

Professor Sanjay Govindjee, Chair

Novel research is currently being performed on commercialization of higher capacity anode materials. Additionally, optimized battery technology for electric vehicles puts increasing demand on faster charging protocols. Both of these demands are theoretically very achievable today, but they inevitably have shortcomings of a decreased battery cycle life and a reduction in battery performance. The shortcomings can be attributed to large mechanical stresses and the rapid growth of corrosive aging mechanisms occurring at electrode-electrolyte interfaces. This dissertation will focus on the study of these unwanted phenomena at the battery's microstructural length scale to aid current research in lithium ion battery optimization. This dissertation combines various existing works to formulate the foundation for a complete multiphysics battery model with the incorporation of corrosive reactions hindering the life cycle and performance of the battery. The reactions that are considered include the formation and growth of the solid electrolyte interphase and plated lithium metal. We will illustrate the implications and limitations of common battery modeling methods with our more detailed microstructural model of a battery cell. We use the finite element method to solve the general governing equations and implement surface reaction kinetics via appropriate Butler-Volmer expressions. We use our model to illustrate the limitations of common experimental techniques, such as the Galvanostatic Intermittent Titration Technique and the Potentiostatic Intermittent Titration Technique, which are used to determine important material transport properties. We then demonstrate how small changes in electrode particle geometry can result in large changes on the mechanical stress and the reaction rates of unwanted chemical reactions. Lastly, we will calculate sensitivity measures through a global sensitivity analysis of the finite element material parameters. These results indicate which material parameters should be experimentally verified and used cautiously in battery modeling.

To my parents ...

Contents

List of Figures

List of Tables

Acknowledgments

Most importantly, I would like to give extreme gratitude for the patience, guidance, and mentoring my advisor Sanjay Govindjee has given me. He has been more than helpful throughout my five and a half years at Berkeley as a teacher and mentor. I am extremely honored to say that he is my advisor and attribute any future success to him. I will miss the stressful meetings, homework assignments, and the informal meetings at the gym.

In addition, I would like to thank Professor Robert Taylor, who has helped me tremendously in understanding and implementing the finite element method. He has been another huge inspiration, especially throughout the tail end of the PhD during the infamous 2020 pandemic. I am grateful for all of the other hyper intelligent professors I have met at Berkeley, including but not limited to Professor Papadopoulos, Professor Li, Professor Moura, Professor Persson, Professor Filippou, Professor Armero, and Professor Harley. I loved my academic experience here through undergrad and my graduate career because of the amazing teachers and staff, especially Shelley Okimoto.

Of course I have to thank my amazing family for supporting and encouraging me to push myself academically ever since I was in grade school. I love all of you and especially want to thank my mother Jenny, my step father Peter, my sister Gioconda, and my late father Marino for the continual motivation. I want to dedicate my dissertation to all of them, because I know without them I would not be in this current position.

Moreover, this dissertation is dedicated to the amazing friends and colleagues I have made in the last 9.5 years. As one can imagine, being drowned in math equations and textbooks can be overwhelming sometimes, but my friends have always been there to cheer me up. From the first couple days as an undergraduate student to the tail end of my Phd graduation, my friends, such as Nikhil Agarwal, Jordan Mautner, Kevin Kai, Jing Liong, Xavier Linn, Jorge Archbold, Sofia Hamilton, Neil Garde, Max Kalmanovich, Pranay Patil, Jessica Zhao, Caroline Lefever, Vyha Do, Veer Bhalla, and Daniela Martinez have been a tremendously fun support system. Albeit, I admit a little too much fun sometimes.

Lastly, with the monetary assistance from the Achievement Rewards for College Scientists Foundation, I was able to focus on my research and coursework during my initial graduate years. I am extremely grateful to call myself an ARCS scholar. I look forward to meeting future scholars at future research symposiums.

Chapter 1

Introduction

1.1 Background

The most common energy storage system is currently the lithium ion battery. This type of battery consists of an anode, cathode, a porous separator, and current collectors attached to the end of each electrode. The electrodes store the battery capacity within the electrode active material particles. The separator allows the transport of lithium ions between the anode and cathode during charging and discharging periods. The current collectors allow the transfer of electrons through the electrical circuitry. Chemical reactions, involving the oxidation and reduction of lithium compounds, generate electric current which then power our electronic devices. During discharge, lithium ions and electrons flow from the anode to the cathode via the electrolyte separator and current collectors, respectively. During this process, the anode gets oxidized, while the cathode is reduced. During charging, an external current is applied and the reverse mechanism occurs. For commercial anode and cathode materials, the phenomena responsible for lithium ions to be stored within the atomic structure of the material is either a phase transformation or ion intercalation between layered sheets of atoms.[1] The reader can visualize a simplified illustration of a battery cell in Figure 1.1.

Conventionally, the cathode is regarded as the positive electrode and the anode as the negative electrode. Both are porous structures in which the pores are filled with additional electrolyte and binding agents to ensure the electrical conductivity and mechanical stability of the entire electrode. The particles in both the anode and cathode that store charge are called active particles. The larger surface area to volume ratio between active particles and the electrolyte enhances chemical reaction rates, lithium ion diffusion, and consequently power capacity. Therefore, there exists an optimal porosity for each configuration for better overall battery capacity and performance. Ramadesigan et al. (2010) discovered that appropriately configured electrode porosity distributions can decrease electrical resistance by

---

[1]Phase transformation materials involve a transformation of the molecule's crystal structure, while intercalation refers to the process of atoms diffusing through layered atomic lattices.

a significant margin. This leads to an increase in cell performance and higher electrode capacity. For most lithium ion batteries, the majority material of the cathode is a metal oxide and that of the anode is graphite due to its long term durability. Common cathodic materials include: Lithium Cobalt Oxide, Lithium Manganese Oxide, Lithium Iron Phosphate, Lithium Nickel Manganese Cobalt Oxide, and Lithium Nickel Cobalt Aluminum Oxide. Each material is used for different applications depending on the need for specific battery life or discharge capacity. Table 1.1 gives a brief description of the nominal voltage, specific energy capacity, and cycle life of these cathode materials used with a graphite anode. Lastly, the electrolyte will consist of lithium salts in a mixture of solvents, which are typically ethylene carbonate and dimethyl carbonate.

Material	Formula	Voltage [V]	Energy [Wh/kg]	Cycle Life
Lithium Cobalt Oxide	$LiCoO_2$	3.6	150-200	500-100
Lithium Manganese Oxide	$LiMn_2O_4$	3.7	100-150	300-700
Lithium Nickel Manganese Cobalt Oxide	$LiNiMnCoO_2$	3.7	150-220	1000-2000
Lithium Iron Phosphate	$LiFePO_4$	3.3	90-120	> 2000

Table 1.1: Common lithium-ion cathode material properties with an anode consisting of graphite (Battery University, 2019).

1.2 Motivation

The vast majority of current battery technology seeks to extend the capacity of the electrode materials and allow for faster charging rates. Additionally, the incorporation of solid state electrolytes is being studied for better thermal stability and performance. These improvements are challenging, but current research shows that they are theoretically very achievable. Before discussing the research and theory in these fields, we first define what the solid electrolyte interphase (SEI) is. The SEI was first discovered by researchers in the 1970s (Peled, 1979). It is a solid layer covering the surface of anode active particles and forms on the first charge cycle due to the chemical instability of electrolyte compounds and lithium ions. This instability, which occurs at the interface of the active particle and surrounding electrolyte, causes a dissolution of electrolyte compounds which then react with available surface electrons and lithium ions. This reaction takes places instead of the desired reaction of lithium intercalation into the active particle due to the reduction potential[2] of many electrolyte so-

---

[2]The reduction potential of a chemical compound is a measure of the affinity of the molecule for acquiring or losing electrons. This potential is commonly used in oxidation/reduction reactions, which is the main reaction in many types of fuel cells.
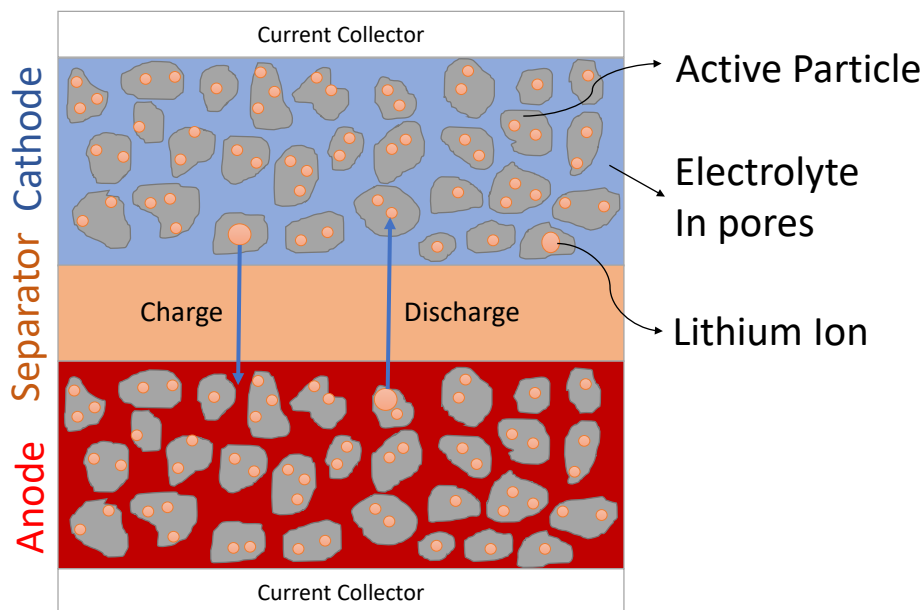
Figure 1.1: Illustration of lithium ion battery composed of current collectors, porous electrodes, and the electrolyte separator. Ions are shown as circular orange dots, and the grey active particles range in size and shape. Realistically, the particles are connected to one another, but they are depicted as shown to qualitatively illustrate the variance in size and shape.

lutes being greater than that of pure lithium. Because a lithium ion battery is assembled in the discharged state, the SEI forms during the first charging period and is necessary for cessation of continued SEI growth.

The chemical reactions that are responsible for the final SEI compound are highly complicated and are not quite yet fully understood, see Verma, Maire, and Novák (2010). From X-ray diffraction images (Bhattacharya, Reza Riahi, and Alpas, 2014), we can see that the SEI is composed of a denser inorganic layer adjacent to the electrode-SEI interface and a more porous organic layer adjacent to the electrolyte-SEI interface. The dense inorganic layer does not facilitate the transfer of electrons but allows the diffusion of lithium ions to be inserted into the active particle as desired. Goodenough and Kim (2009) postulate a proper reduction potential stability window of lithium salts dissolved in the electrolyte solvent. Their work is related to molecular orbital theory and is schematically illustrated in Figure 1.2. The figure gives an oversimplified schematic of stable energy levels for the electrolyte in comparison to anode and cathode compounds. The diagram does not include the effect of certain salts and additives dissolved in the electrolyte. Unfortunately, for most electrolyte compounds it is energetically more favorable to reduce the solvent molecules instead of lithium insertion into

the active particle. Daniel and Besenhard (2011) (Ch. 16) provides an extensive overview of SEI formation and reduction potentials for various electrolyte compounds.
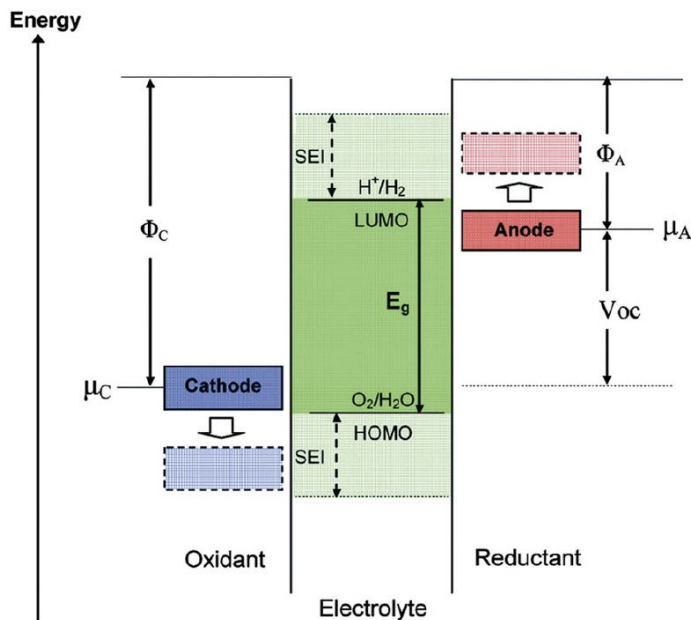
Figure 1.2: Open circuit energy diagram taken from Wang et al. (2018). Φ_A and Φ_C are the anode and cathode electric potentials. E_g is the electrolyte's reduction potential stability window. μ_A and μ_C are the equilibrium reduction potentials of the anode and cathode.

1.2.1 High Capacity Electrodes

Currently, there are a few available anode materials that theoretically allow for an order of magnitude greater capacity than a conventional graphite anode. These materials undergo a much more significant phase transformation as compared to graphite, which results in a much larger expansion of the atomic lattice. One of the most commonly studied higher capacity anodes is silicon. These type of materials allow for much larger stoichiometric ratios of the lithium ions to the host molecules. For example, the stoichiometric ratio of a lithium silicon battery is $Li_{22}Si_5$, while that of graphite is only LiC_6. Thus, silicon anodes have a theoretical capacity of 3600 mAh/g while graphite's theoretical capacity is merely 372 mAh/g. The larger energy density comes at the cost of large volumetric expansions on the order of 300% of the original material size resulting in large stresses and component fractures when constrained by the battery casing. The large expansion also degrades the adhesion of the conductive network between silicon and carbon binder particles creating a larger internal electrical resistance within the electrode matrix. Ryu et al. (2004) discusses the reduction in battery life due to silicon expansion. Ultimately, this reduces the life cycle of

lithium-silicon batteries. Nitta et al. (2015) provides a comprehensive review on current and future electrode material chemistries. Overall the consensus is that intercalation compounds provide long term durability but are unable to provide a high capacity density. The smaller volumetric expansion of graphite results in good mechanical and electrochemical stability, which is why it is the most common commercialized anode.

The second shortcoming of these higher capacity materials is the destabilization of the SEI layer and any deposited surface film growth, such as plated lithium. The continuous expansion and contraction of these materials cracks these surface films and creates additional pores. More electrolyte is able to fill into these pores, which allows for continued reactions between the available lithium ions. This grows the thickness of the SEI layer and deposited lithium layer even further. Because of this, cell resistance increases due to the increase in SEI thickness, ion diffusivity decreases, and irreversible consumption of lithium ions increases as well. The SEI layer is less electrically conductive compared to the active particle which results in a higher potential drop for the same current applied due to increased electrical resistance. The end result is a decrease in cell efficiency and battery capacity.

1.2.2 Faster Charging Rates

The next key area in research is the application of faster charging rates. The shortcoming of this is another chemical instability of lithium ions near the surface of the active particles. Metallic lithium is plated on the surface contributing to additional loss of lithium ions and a decrease in cell efficiency. The reaction mechanism behind this is similar to that of SEI formation. At fast charging rates, pure lithium deposition is energetically more favorable than lithium intercalation into the active particle due to the reduction potential of both compounds being very close to each other. In addition, low temperature operations, over-charging, and low anode/cathode capacity ratios result in more lithium plating. At lower temperatures, the reaction rate of lithium intercalcation decreases, which causes the accumulation of lithium ions at the active particle surface resulting in lithium deposition instead of intercalation. Overcharging not only causes an accumulation of lithium at the surface but also raises the active particle's electric potential above that of the Fermi level of lithium metal resulting in a higher affinity for plating. A low anode/cathode capacity ratio symbolizes that the anode reaches its maximum concentration quicker than that of the cathode material. As the anode is almost fully charged, its lithium intercalation rate decreases. However, there is an abundance of lithium ions shuttled to the anode's surface from the bulk concentration in the cathode, and then react with available electrons resulting in lithium deposition.

Lithium plating typically covers the SEI and increases anode polarization at the electrolyte/active particle interface. This then promotes further lithium plating. As charging continues, the available sites for intercalation decrease and the deposition rate of lithium increases as the transport rate of lithium ions from the electrolyte exceeds the intercalation rate. As a result, lithium plating grows with charging time. It should also be noted that lithium plating is generally not uniform over the surface of active particles and can result in dendrites. Dendrites can quickly grow through the electrolyte separator, come into contact

with the cathode, and short circuit the entire battery cell. As an example, a few Samsung phones were infamous for sudden explosions because of this catastrophic phenomena (Loveridge et al., 2018). Figure 1.3 depicts available lithium ions from the surrounding electrolyte resulting in three reactions that can occur at the active material's surface. If lithium intercalation is hindered, the remaining lithium ions can react with solvent compounds in the electrolyte to form the SEI or combine solely with free electrons resulting in metallic deposition.
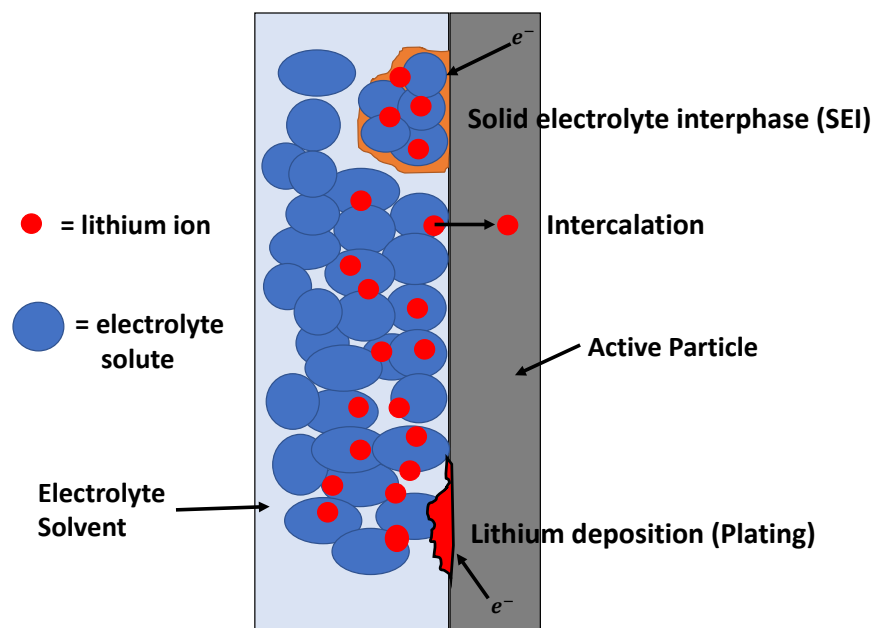
Figure 1.3: Illustration of the three reactions that occur at the battery's anode.

1.2.3   Solid State Electrolytes

Lastly, research on the use of solid state electrolytes has become popular due to their thermal and mechanical stability in terms of short circuiting and dendrite prevention. The stiffness of a solid material in lieu of a liquid filled electrolyte separator prevents the rapid growth of dendrites, which consequently mitigates battery short circuiting. Hassoun and Scrosati (2015) describes some of the shortcomings of solid state electrolyte manufacturing and performance. It is difficult to create a smooth junction at the electrode and electrolyte interface. Solid electrolyte materials also have low electrical conductivities compared to available liquid electrolytes and require the use of expensive elements to remedy this. Our research does not aim to specifically tackle this question but will be formally crafted so that solid electrolytes can be incorporated.

1.3 Literature Review
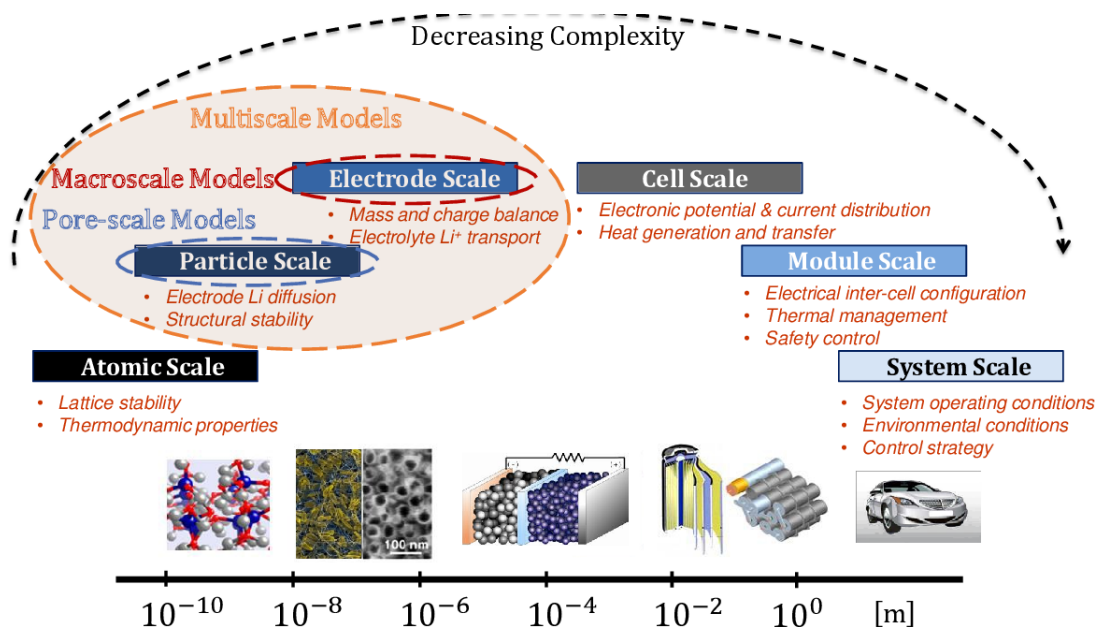
Figure 1.4: Illustration of increasing complexity for various battery modeling techniques (Arunachalam, 2017; Lee, Smith, and Kim, 2011).

Various battery models exist in the literature currently. These range in complexity from atomistic models derived from first principle calculations or molecular dynamics to high order system level models at the electric vehicle level (Moura et al., 2010). Molecular simulations can vary from studying the intercalation process of an electrode (Ayudinol et al., 1997) to understanding the possibility of using a new cathode material (Alfaruqi et al., 2019). Within this wide range of length scales, there are a variety of simulation subsets available. We will be interested in utilizing continuum mechanics at its finest scale, which consequently is at the micro scale level of the battery. Before we delve into the governing relations, we will briefly summarize prominent publications that motivated our work. The reader is referred to Grazioli, Magri, and Salvadori (2016) for a brief discussion on the necessary physics for a proper computational battery model.

1.3.1 Porous Electrode Theory

To properly model the electrochemistry, one needs an appropriate physical theory for the constituents in a battery cell. The pioneering works of Newman and Tobias (1962), Newman and Tiedemann (1975), and Doyle, Fuller, and Newman (1993) are a standard in electro-chemical modeling. These works involve the homogenization of an idealized microstructure

to determine macroscopic electrode behavior. At the micro scale, they assume spherical active particles are uniformly and continuously dispersed throughout the porous electrode. Liquid electrolyte fills the remaining pores and is always in continuous contact with the active material. The macroscopic response is then achieved by a volume averaged homogenization, which yields that the independent variables of the particles and electrolyte coexist simultaneously at every spatial point. The porosity, tortuousity, and average surface area per unit volume of the active particles are some of the key parameters describing the homogenization process. The governing physics involved can be briefly summarized by the following two conservation laws applied separately for the solid state active particles and liquid phase electrolyte solution: (1) mass balance of lithium and (2) charge conservation.

These laws in total generate four coupled partial differential equations (PDE), two for the solid particle state and two for the liquid electrolyte state. They result in a time dependent advection diffusion PDE for each mass balance equation and time independent version of Ampere's law for each charge conservation equation. At a macro-scale, the volumetric source (or sink) rate of ionic species is described by a Butler-Volmer equation. Jokar et al. (2016) gives a brief review of this simplified "psuedo-two-dimensional" model applied specifically to lithium ion batteries. It should be noted that porous electrode theory has been applied to other battery systems. It is widely used and applicable in any fuel cell simulation software due to its robustness and ease of implementation. The reader is suggested to Tiedemann (2008) for a wide review of various publications concerning this theory applied to the lead-acid battery as one example.

Smith and Bazant (2017) extends the applicability of this theory by rederiving the constitutive laws for the inclusion of phase transformations and more complicated chemical energy landscapes. This work utilizes the chemical potential and its gradient in the constitutive laws for lithium flux within the active particle. It generalizes the chemical potential to allow for arbitrary free energy landscapes. This model allows for phase segregation of the active particles instead of purely assuming a one phase material particle. The work stems from non-equilibrium thermodynamics in which the constitutive equations are derived from a suitable definition of the free energy. Bazant (2012) provides an extensive derivation of a thermodynamically consistent theory for porous electrodes and even includes small strain intercalation effects on the kinetic reaction rate and ion diffusion. An application of this theory studying phase boundary separation in $LiFePO_4$ with phase field theories is presented in Cogswell and Bazant (2012). Note that these works do not consider thermal aspects. An extension to thermal energy conservation is presented in Latz and Zausch (2011). The authors derive a thermodynamically consistent theory for the constitutive relations but neglect mechanical deformations.

1.3.2 Coupled Electrochemical and Mechanical Models

We are interested in not only the electrochemical behavior of lithium ion cells, but also the mechanical deformation state. When constrained, large deformations could eventually lead to plastic deformation and fracture of the battery pack. Experimental results (Safari

et al., 2009) indicate that the primary capacity loss of a battery cell is through mechanical degradation. The adhesion of the conductive matrix of the electrode weakens, which results in loss of particle contact. Mechanical models are traditionally split into using small strain or finite deformation theory. Finite deformation is complicated because the strain measures are nonlinear, as explained in Gurtin (1982).

Similar to porous electrode theory, many multiscale homogenization theories have been presented and used in the literature. Salvadori, Bosco, and Grazioli (2014) considers a representative volume element (RVE) at the micro scale of the electrode, which would be able to realistically consider the microstructure of the cell; see Figure 1.5. The geometry at this level can be arbitrary and also models the conductive binder. The authors extended this work in Salvadori, Grazioli, and Geers (2015) and Salvadori et al. (2015) for ionic transport in the electrolyte. Latz and Zausch (2015) also allows for any desired three dimensional geometry and includes fluid motion of the electrolyte, which is often neglected in the battery literature. Zhang, Krischok, and Linder (2016), Wu (2019), and Pannala et al. (2015) are other notable multiscale works among others. These various authors all derive thermodynamically consistent governing equations and constitutive relations using infinitesimal kinematics and mechanical pressure effects on ion diffusion. Wu and Lu (2019) models the additional pressure effect on lithium reaction kinetics with an idealized spherical particle RVE.

Other interesting publications utilizing asymptotic homogenization are those by Ciucci and Lai (2011) and Richardson, Denuault, and Please (2012). The authors assume periodic microstructures at multiple length scales and then derive governing macroscopic laws from an in depth homogenization procedure. Zhao et al. (2019) gives a current review on many coupled mechanical and electrochemical models. The shortcomings of these multiscale approaches is the use of linear kinematics, no incorporation of SEI formation or lithium plating, and the neglect of thermal properties of the battery cell. Ultimately, these models are very complete and accurate, but the computational cost is very high.

Research is surging in the study of higher capacity anodes, such as silicon, and consequently the implementation of finite deformation, plasticity, and fracture theories due to the large expansions these materials exhibit. Bower, Guduru, and Sethuraman (2011), Bucci, Y.M., and Carter (2016), and Dal and Miehe (2015), present their model from a thermodynamic perspective utilizing mass, charge, and momentum conservation laws. These models are formulated specifically for solid active particles. Ganser et al. (2019) presents a similar theory to active particles but with the specific application to binary solid state electrolytes. Bower and Guduru (2012) extended this theory for plasticity with pressure gradient effects on lithium intercalation reaction rates. Bower et al. (2015) and Bucci et al. (2017) use these theories to study stress effects on lithium silicon particles.

Hu et al. (2017), Gwak and Ju (2019), and Wang, Siegel, and Garikipati (2017) present fully coupled electrochemical, mechanical, and thermal models. Hu et al. (2017) studies the stress distribution affecting lithium ion concentration in hollow spheres. Gwak and Ju (2019) also uses a complete multiphysics model in a multi-scale approach to study the phase segregation and thermal changes in lithium iron phosphate cathodes. Wang, Siegel, and Garikipati (2017) analyzes porosity changes during charging and discharging periods for

graphite with nickel manganese cobalt oxide (NMC) battery cells. The authors improve on this by modeling the electrode's conductive binder and the fluid motion of the electrolyte in Wang and Garikipati (2018).
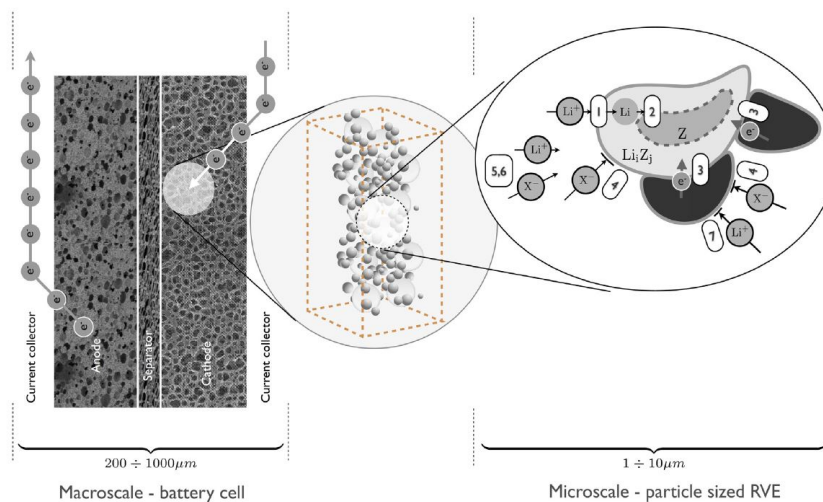
Figure 1.5: Representative volume element (RVE) of an example multi-scale theory (Salvadori, Grazioli, and Geers, 2015).

1.3.3   SEI and Lithium Plating

The formation of the SEI on the first cycle is crucial to prevent further reduction of electrolyte compounds while still allowing the diffusion of lithium ions through the film layer. Peled (1979) first introduced the concept of the SEI by noting it is an electrically insulating but ionically conducting layer formed on the surface of the electrode particle. As explained above, one wants the electrolyte electric potential to be within stable ranges at the interfaces of the electrodes. Otherwise, electrolyte molecules can be reduced, a side reaction can occur, and the formation of the SEI continues. Illustrations of this at the atomistic scale have been simulated by numerous publications through density functional theory (DFT), Monte Carlo methods, and molecular dynamics (MD). A complete list of DFT calculations of stable potential ranges for various electrolyte compounds and influence of other factors enhancing SEI growth is given in Wang et al. (2018) and Horstmann, Single, and Latz (2019).

   The same chemical stability discussed above occurs for lithium deposition. Specifically looking at graphitic anodes, Liu et al. (2016) discusses the major causes of lithium plating and attributes a majority of its growth to the very close equilibrium electric potentials of graphite and pure lithium metal. The intercalation reaction at the active particle and electrolyte surface generates an electric current, which increases the particle's surface potential. This

is known as anode polarization, in which the current associated with a chemical reaction increases the surface potential of electrode materials. Continued polarization makes the surface potential of the active particle fall below the equilibrium potential of metallic lithium, which favors lithium deposition instead of the intercalation reaction. Any event slowing the diffusion of solvated lithium ions in the electrolyte, intercalation reaction rate, or diffusion of lithium into the active particle will eventually result in more lithium deposition. The deposition rate is enhanced by low temperatures, high charging rates, and overcharging. Low temperatures reduce the reaction rates of lithium intercalation. High charging rates and overcharging allow for the accumulation and saturation of lithium at the electrode surface which is then available to react with surface electrons.

Phase field theories, which are common in solidification modeling, have been applied to SEI growth and lithium plating. The use of an interfacial energy gradient and introduction of an order parameter allows one to smooth the interfacial boundary conditions. Simulations of this type, which include Guan, Liu, and Lin (2015), Guan, Liu, and Gao (2018), and Deng, Wagner, and Muller (2013) among others, allow one to visualize the propagating boundary through time. Phase field theories have also been incorporated for dendrite modeling as well in Yurkiv et al. (2018) and Liang et al. (2012).

At the continuum level, the SEI is most commonly modeled as a side reaction via the Butler-Volmer equation. Christensen and Newman (2004) was one of the first to introduce this concept and their theory has been included in many porous electrode models thereafter. The dissertation of Christensen (2005) utilizes this theory for the formation of two common SEI compounds and incorporates mechanical failure mechanisms in a finite deformation setting. However, they are limited by assuming a spherical particle model, which would not be able to take into account arbitrary porosity or geometrical effects. Pinson and Bazant (2013) and Kindermann et al. (2017) utilize the Butler-Volmer equation as a side reaction and are able to accurately predict cell voltage profiles after many charge/discharge cycles. Ge et al. (2017) and Barai, Higa, and Srinivasan (2017) also perform similar calculations but focus on lithium plating and dendrite formation. The prominent work by Yang et al. (2017) has two side reactions terms, one for the SEI and one for plating, and accurately captures the long term capacity fade of a cell. They note that the there is a transition range in which the initial capacity fade is attributed to SEI growth. Then, after a number of charging cycles, plating is the major contribution and grows exponentially with time. As the SEI continues to grow, anode porosity decreases resulting in larger electrolyte potential gradients. Once the anode particle's potential becomes negative in reference to that of pure lithium, metallic deposition will occur and continues exponentially as more lithium is consumed.

1.4 Dissertation Outline

As outlined above, one of the primary goals of battery modeling is to predict performance and to design better batteries. We currently have the knowledge and ability to address the motivational issues stated earlier, such as the use of higher capacity anodes in conjunction

with the ability to charge our battery cells at a quicker rate. Researchers often tackle these respective shortcomings separately, but we seek to develop a comprehensive battery model that can address both issues simultaneously. This dissertation aims to extract ideas from existing publications to couple the battery's mechanical, electrochemical, and thermal governing equations with appropriate incorporation of the common aging mechanisms of SEI and lithium plating growth. In addition, we seek to model the active particle and electrolyte elements separately so that arbitrary porous geometries can be considered.

Chapter 2 will properly define independent and dependent variables that will be used. Additionally, it will provide an overview of the physical governing equations, reaction kinetics, and derivations of constitutive relations for the dependent variables. Chapter 3 will discuss the finite element method (FEM), the solution method we use, and the overall structure of the user element subroutines that needed to be coded. Within the solution structure, the development of interface elements was required to properly account for boundary conditions emanating from the reaction kinetics. We will showcase a few test cases showing the efficacy of the active particle user elements, electrolyte elements, and a full battery cell utilizing particle, electrolyte, and interface elements. Chapter 4 uses the FEM model to reproduce two commonly used experimental techniques in determining an electrode's diffusion coefficient. The results show the sensitivity of the analytical solutions derived and possible errors in current experimental analysis. Chapter 5 demonstrates the effect of deviations on electrode particle geometry in relation to stress distributions and reaction rate kinetics. Chapter 6 utilizes global sensitivity analysis on finite element solutions in relation to input material properties. The sensitivity measures generated provide useful indications on which battery parameters should be experimentally verified and used cautiously in computer simulations. Lastly, Chapter 7 concludes this dissertation by commenting on our analyses, limitations of our current model, and future works for the research presented herein.

Chapter 2

Governing Equations and Relations

This chapter will define the primary variables used in this dissertation. We will first give a brief overview of the necessary conservation laws for a complete multiphysics battery model. Then, constitutive relations will be derived from the first and second law of thermodynamics. Lastly, this chapter will discuss appropriate mathematical approximations to model the reaction kinetics occurring at electrode-electrolyte interfaces.

2.1 Conservation Laws

In the derivation of the governing PDEs, we assume linear elastic mechanics. For notation, $\mathbf{x_0}$ will denote the vector describing the initial reference position of a material point. At a new time t, the new position vector is $\mathbf{x}(t)$, which yields $\mathbf{u}(t) = \mathbf{x}(t) - \mathbf{x_0}$ as the displacement. Taking time derivatives d/dt of the displacement gives the velocity $\mathbf{v}(t) = \dot{\mathbf{u}}(t) = \dot{\mathbf{x}}(t)$. We can then obtain the velocity gradient $d\mathbf{v}/d\mathbf{x} = \mathrm{grad}(\dot{\mathbf{x}})$ and the acceleration, $\mathbf{a}(t) = \dot{\mathbf{v}}(t) = \ddot{\mathbf{x}}(t)$. We define the infinitesimal strain tensor as $\boldsymbol{\varepsilon} = \frac{1}{2}\left(\nabla\mathbf{u} + \nabla\mathbf{u}^T\right)$ and strain rate tensor as $\dot{\boldsymbol{\varepsilon}}$, which both are symmetric second order tensors (see Chadwick (1999)).

Additionally, at each material point the concentration c of a particular chemical species (i.e. lithium ion concentration in cathode, electrolyte solution, or anode) is defined as the number of moles of the species per unit volume [mol/m^3]. The electric potential ϕ is described in Volts [V], and the temperature T will be given in degrees Kelvin [K]. All variables are also a function of position and time. For clarity, we give reference units in brackets [·].

2.1.1 Linear Momentum Conservation

Considering an arbitrary volume of a material region, the balance of linear momentum (see Chadwick (1999)) yields the first governing equation for the active particle,

$$\mathrm{div}\,\boldsymbol{\sigma} + \rho\mathbf{b} = \rho\mathbf{a}, \tag{2.1}$$

where $\mathbf{b}$ is the body force per unit mass [N/kg], ρ is the mass density [kg/m^3], and $\boldsymbol{\sigma}$ is the Cauchy stress tensor [N/m^2]. Balance of angular momentum enforces the symmetry of the

Cauchy stress such that $\boldsymbol{\sigma}^T = \boldsymbol{\sigma}$. The constitutive relation for $\boldsymbol{\sigma}$ in terms of $\{\mathbf{u}, c, \phi, T\}$ will be given shortly.

2.1.2 Mass Conservation

We now consider the lithium ion concentration in the volume P of the material (Hariharan, Tagade, and Ramachandran, 2018). The change in lithium concentration within P will be equal to the flux $\mathbf{j}$ [mol/m²s] entering or leaving through the volume's boundary ∂P. We assume that within P lithium ions do not react with other compounds, such that there are no volumetric source or sink terms. Therefore, we can take a time derivative yielding

$$\frac{d}{dt} \int_P c\, dV = -\int_{\partial P} \mathbf{j} \cdot \mathbf{n}\, dA\,, \tag{2.2}$$

where $\mathbf{j}$ is the flux through the surface with outward normal $\mathbf{n}$. Using the divergence theorem and bringing the time derivative inside the integral yields,

$$\int_P \left(\frac{\partial c}{\partial t} + \mathrm{div}\mathbf{j} \right) dV = 0\,, \tag{2.3}$$

and by the localization theorem, we have the second governing equation,

$$\frac{\partial c}{\partial t} + \mathrm{div}\mathbf{j} = 0\,. \tag{2.4}$$

2.1.3 Charge Conservation

We derive the time independent version of Ampere's law with the full set of PDEs given in Maxwell's equations (Latz and Zausch, 2015). This is in contrast with porous electrode theory (Newman and Tiedemann, 1975), which immediately assumes electroneutrality. Using appropriate assumptions, electroneutrality will be the final result as expected. The entire set of electromagnetic conservation equations are,

$$\mathrm{div}\mathbf{D} = q\,, \tag{2.5}$$

$$\nabla \times \mathbf{H} = \mathbf{i} + \frac{d\mathbf{D}}{dt}\,, \tag{2.6}$$

$$\nabla \times \mathbf{E} = -\frac{d\mathbf{B}}{dt}\,, \tag{2.7}$$

$$\mathrm{div}\mathbf{B} = 0\,. \tag{2.8}$$

These equations are commonly referred to as Gauss's law, Ampere's law, Faraday's law, and Gauss's law for magnetism, respectively (Eringen and Maugin, 1989). As written, q is the free charge density [C/m³], $\mathbf{B}$ is the magnetic flux density measured in Tesla [T], $\mathbf{D}$ is the electric displacement [C/m²], $\mathbf{i}$ is electric current density [C/m²s], $\mathbf{H}$ is the magnetic field

[C/m · s], and $\mathbf{E}$ is the electric field [V/m]. The electric field is the gradient of the electric potential, i.e. $\mathbf{E} = -\nabla\phi$. To make a complete definition of the electric displacement, we define the polarization $\mathbf{P}$ which then yields

$$\mathbf{D} = \epsilon_0\mathbf{E} + \mathbf{P}\,, \tag{2.9}$$

with ϵ_0 being the permittivity of free space. We now assume that we are dealing with a linear and isotropic dielectric medium with the polarization aligned proportional to the electric field,

$$\mathbf{P} = \chi\epsilon_0\mathbf{E}, \tag{2.10}$$

where χ is the electric susceptibility of the dielectric. Equation (2.9) then simplifies to

$$\mathbf{D} = \epsilon\mathbf{E} = -\epsilon\nabla\phi \tag{2.11}$$

with $\epsilon = \epsilon_0(1 + \chi)$. The total magnetic field is defined in terms of the magnetic flux density and magnetization $\mathbf{M}$,

$$\mathbf{H} = \frac{1}{\hat{\mu}_0}\mathbf{B} - \mathbf{M} \tag{2.12}$$

with $\hat{\mu}_0$ being the permeability of free space. We use the notation of $\hat{\mu}_0$ in lieu of μ_0 to distinguish between the chemical potential that is defined shortly. This is in contrast to its variable definition commonly used in electromagnetics. Next we assume steady state neutral charge $q = 0$, any magnetization effects are negligible $\mathbf{M} = 0$, the total magnetic field generated by the current in the cell is negligible $\mathbf{B} = 0$, and any relativistic effects are ignored. Therefore, the final nonzero equations only include Gauss's law and Ampere's law,

$$\operatorname{div}\mathbf{D} = 0\,, \tag{2.13}$$

$$\mathbf{i} + \frac{d\mathbf{D}}{dt} = 0\,. \tag{2.14}$$

Taking the divergence of Equation (2.14) and utilizing the time derivative of Equation (2.13), we obtain the simplified version of Ampere's law for charge conservation,

$$\operatorname{div}\mathbf{i} = 0\,. \tag{2.15}$$

2.1.4 Energy Conservation

For the last relation, we define the thermal flux vector $\mathbf{q}$ [J/m^{2}s] for a surface ∂P with outward normal $\mathbf{n}$. Additionally, h is the heat generated per unit volume [J/m^3], ρ is the material mass density [kg/m^3], and C_p is the specific heat per unit mass [J/K · kg]. The evolution of the temperature field is governed by

$$\rho C_p\frac{\partial T}{\partial t} + \operatorname{div}\mathbf{q} = h\,, \tag{2.16}$$

where the heat source term will be given by Joule heating (Latz and Zausch, 2015),

$$h = \mathbf{i} \cdot \mathbf{E}\,. \tag{2.17}$$

2.1.5 Summary

In summary, the four governing equations we seek to solve are:

$$\mathrm{div}\boldsymbol{\sigma} + \rho\mathbf{b} = \rho\ddot{\mathbf{u}}, \tag{2.18}$$

$$\frac{\partial c}{\partial t} + \mathrm{div}\mathbf{j} = 0, \tag{2.19}$$

$$\mathrm{div}\mathbf{i} = 0, \tag{2.20}$$

$$\rho C_p \frac{\partial T}{\partial t} + \mathrm{div}\mathbf{q} = h. \tag{2.21}$$

2.2 Constitutive Relations

This section will be split into derivations of the constitutive relations for the active particle and electrolyte separately. This is common in the literature (Newman and Thomas-Alyea, 2012) as the solid and liquid phases behave differently.

2.2.1 Active Particle

To derive the constitutive equations, we set up the necessary thermodynamic energy and entropy relations; see Zemansky and Dittman (1981) and Kovetz (2000). The total power expended on the system changes the system's internal energy rate (Latz and Zausch, 2015),

$$\rho \dot{u} = \text{div}\left(\boldsymbol{\sigma}\dot{\mathbf{x}}\right) + \rho \mathbf{b} \cdot \dot{\mathbf{x}} - \text{div}\left(\mathbf{q}\right) - \text{div}\left(\mathbb{E} \times \mathbb{H}\right) + \rho h + u_{mix}\dot{c} - \nabla u_{mix} \cdot \mathbf{j}\,, \tag{2.22}$$

where u_{mix} is the internal energy of the diffusing species (Bucci, Y.M., and Carter, 2016), $\mathbb{E} = \mathbf{E} + \dot{\mathbf{x}} \times \mathbf{B}$ is the Galilei invariant electric field, and $\mathbb{H} = \mathbf{B}/\mu_0 - \dot{\mathbf{x}} \times \mathbf{D}$ is the Galilei invariant magnetic field. Following previous work in Kovetz (2000), the electromagnetic term can be simplified to

$$-\text{div}\left(\mathbb{E} \times \mathbb{H}\right) = \mathbf{i} \cdot \mathbf{E} + \mathbf{E} \cdot \frac{\partial \mathbf{D}}{\partial t} + \left[(\mathbf{E} \cdot \mathbf{D})\mathbf{1} - \mathbf{E} \otimes \mathbf{D}\right] : \text{grad}(\dot{\mathbf{x}})\,. \tag{2.23}$$

Using Equation (2.11) and assuming $\mathbf{B} = \mathbf{0}$, we define the Maxwell stress tensor (see Griffiths (2013), pgs. 362-366) as

$$\boldsymbol{\sigma}^M = \epsilon \mathbf{E} \otimes \mathbf{E} - \epsilon(\mathbf{E} \cdot \mathbf{E})\mathbf{1}\,, \tag{2.24}$$

and we substitute this relation into Equation (2.22) yielding

$$\rho \dot{u} = \text{div}\left(\boldsymbol{\sigma}\dot{\mathbf{x}}\right) + \rho \mathbf{b} \cdot \dot{\mathbf{x}} - \text{div}\left(\mathbf{q}\right) + \mathbf{i} \cdot \mathbf{E} + \mathbf{E} \cdot \frac{\partial \mathbf{D}}{\partial t} - \boldsymbol{\sigma}^M : \text{grad}(\dot{\mathbf{x}}) + \rho h + u_{mix}\dot{c} - \nabla u_{mix} \cdot \mathbf{j}\,. \tag{2.25}$$

In the static case where $\ddot{\mathbf{x}} = 0$, we can expand the mechanical term and make note of the symmetry of the Cauchy stress $\boldsymbol{\sigma}$ and the Maxwell stress $\boldsymbol{\sigma}^M$ so that the velocity gradient $\text{grad}(\dot{\mathbf{x}})$ can be replaced by the symmetric strain rate $\dot{\boldsymbol{\varepsilon}}$. Equation (2.25) then becomes

$$\rho \dot{u} = (\text{div}(\boldsymbol{\sigma}) + \rho \mathbf{b}) \cdot \dot{\mathbf{x}} + \left(\boldsymbol{\sigma} - \boldsymbol{\sigma}^M\right) : \dot{\boldsymbol{\varepsilon}} - \text{div}\left(\mathbf{q}\right) + \mathbf{i} \cdot \mathbf{E} + \mathbf{E} \cdot \frac{\partial \mathbf{D}}{\partial t} + \rho h + u_{mix}\dot{c} - \nabla u_{mix} \cdot \mathbf{j}\,, \tag{2.26}$$

and we can simplify the equation above using mechanical equilibrium to obtain

$$\rho \dot{u} = \left(\boldsymbol{\sigma} - \boldsymbol{\sigma}^M\right) : \dot{\boldsymbol{\varepsilon}} - \text{div}\left(\mathbf{q}\right) + \mathbf{i} \cdot \mathbf{E} + \mathbf{E} \cdot \frac{\partial \mathbf{D}}{\partial t} + \rho h + u_{mix}\dot{c} - \nabla u_{mix} \cdot \mathbf{j}\,. \tag{2.27}$$

Next, the entropy s is governed by the inequality

$$\rho \dot{s} \geq -\text{div}\left(\frac{\mathbf{q}}{T}\right) + \rho \frac{h}{T} - \text{div}\left(s_{mix}\mathbf{j}\right)\,, \tag{2.28}$$

where s_{mix} is the entropy of the diffusing species. Expanding out the divergence terms, this inequality becomes

$$\rho \dot{s} \geq \frac{1}{T^2} \mathbf{q} \cdot \nabla T - \frac{1}{T} \operatorname{div}(\mathbf{q}) + \rho \frac{h}{T} - \mathbf{j} \cdot \nabla s_{mix} - s_{mix} \operatorname{div}(\mathbf{j}) \,. \tag{2.29}$$

Since temperature is strictly positive, we can multiply Equation (2.29) by T and use mass conservation, Equation (2.4), to obtain

$$\rho T \dot{s} \geq \frac{1}{T} \mathbf{q} \cdot \nabla T - \operatorname{div}(\mathbf{q}) + \rho h - T \mathbf{j} \cdot \nabla s_{mix} + T s_{mix} \dot{c} \,. \tag{2.30}$$

We can solve for ρh in Equation (2.27) and substitute this into Equation (2.30), which gives a new inequality

$$
\begin{aligned}
0 \geq{}& \rho(\dot{u} - T\dot{s}) + \frac{1}{T} \mathbf{q} \cdot \nabla T + \mathbf{j} \cdot (\nabla u_{mix} - T \nabla s_{mix}) \\
& - (u_{mix} - T s_{mix}) \dot{c} - (\boldsymbol{\sigma} - \boldsymbol{\sigma}^M) : \dot{\boldsymbol{\varepsilon}} - \mathbf{i} \cdot \mathbf{E} - \mathbf{E} \cdot \dot{\mathbf{D}} \,.
\end{aligned}
\tag{2.31}
$$

The Helmholtz specific free energy is $\psi = u - Ts$, and the chemical potential is $\mu = u_{mix} - T s_{mix}$[1] (see Bucci, Y.M., and Carter (2016) or Bower, Guduru, and Sethuraman (2011)). With these new definitions, Equation (2.31) simplifies to

$$0 \geq \rho \dot{\psi} + \rho s \dot{T} + \frac{1}{T} \mathbf{q} \cdot \nabla T + \mathbf{j} \cdot (\nabla \mu + s_{mix} \nabla T) - \mu \dot{c} - (\boldsymbol{\sigma} - \boldsymbol{\sigma}^M) : \dot{\boldsymbol{\varepsilon}} - \mathbf{i} \cdot \mathbf{E} - \mathbf{E} \cdot \dot{\mathbf{D}} \,. \tag{2.32}$$

Next, we additively decompose the total strain tensor into three separate tensors: a tensor involving the mechanical deformation, one involving the concentration swelling, and one involving the thermal swelling. One can perform this decomposition in linear elasticity, such that

$$
\begin{aligned}
\boldsymbol{\varepsilon} &= \boldsymbol{\varepsilon}_{mech} + \boldsymbol{\varepsilon}_{swell} + \boldsymbol{\varepsilon}_{thermal} \,, & (2.33) \\
\boldsymbol{\varepsilon} &= \boldsymbol{\varepsilon}_{mech} + \frac{\Omega}{3}(c - c_0)\mathbf{1} + \frac{\alpha}{3}(T - T_0)\mathbf{1} \,, & (2.34)
\end{aligned}
$$

where Ω is the swelling coefficient defined as the isotropic expansion due to lithium insertion/intercalation from an initial concentration c_0 to the current concentration c. Additionally, α is the volumetric thermal expansion of the material defined from an initial temperature T_0. We can define a hydrostatic pressure term, $p = -\frac{1}{3} \operatorname{tr} \left(\boldsymbol{\sigma} - \boldsymbol{\sigma}^M \right)$

$$
\begin{aligned}
0 \geq{}& \rho \dot{\psi} + (\rho s + \alpha p)\dot{T} + \frac{1}{T} \mathbf{q} \cdot \nabla T + \mathbf{j} \cdot (\nabla \mu + s_{mix} \nabla T) \\
& - (\mu - \Omega p)\dot{c} - (\boldsymbol{\sigma} - \boldsymbol{\sigma}^M) : \dot{\boldsymbol{\varepsilon}}_{mech} - \mathbf{i} \cdot \mathbf{E} - \mathbf{E} \cdot \dot{\mathbf{D}} \,.
\end{aligned}
\tag{2.35}
$$

---

[1]The chemical potential describes the change in energy of the system due to the addition or removal of a chemical species with all other species' concentrations in the mixture remaining constant.

We assume that the Helmholtz free energy ψ will be a function of mechanical strain, concentration, electric displacement, and temperature,

$$0 \geq \left(\rho \frac{\partial \psi}{\partial \boldsymbol{\varepsilon}_{mech}} - \boldsymbol{\sigma} + \boldsymbol{\sigma}^M \right) : \dot{\boldsymbol{\varepsilon}}_{mech} + \left(\rho \frac{\partial \psi}{\partial c} - \mu + \Omega p \right) \dot{c} + \left(\rho \frac{\partial \psi}{\partial \mathbf{D}} - \mathbf{E} \right) \cdot \dot{\mathbf{D}}$$
$$+ \left(\rho \frac{\partial \psi}{\partial T} + \rho s + \alpha p \right) \dot{T} + \frac{1}{T} \mathbf{q} \cdot \nabla T + \mathbf{j} \cdot (\nabla \mu + s_{mix} \nabla T) - \mathbf{i} \cdot \mathbf{E} \,. \tag{2.36}$$

For Equation (2.36) to be strictly negative semi-definite and following the Coleman and Noll approach (Coleman and Noll, 1963), the following constitutive laws must hold,

$$\boldsymbol{\sigma} = \rho \frac{\partial \psi}{\partial \boldsymbol{\varepsilon}_{mech}} + \boldsymbol{\sigma}^M \,, \tag{2.37}$$

$$\mu = \rho \frac{\partial \psi}{\partial c} + \Omega p \,, \tag{2.38}$$

$$\mathbf{E} = \rho \frac{\partial \psi}{\partial \mathbf{D}} \,, \tag{2.39}$$

$$s = -\frac{\partial \psi}{\partial T} - \frac{\alpha}{\rho} p \,, \tag{2.40}$$

$$\mathbf{i} = \mathbf{K} \mathbf{E} \,, \tag{2.41}$$

$$\mathbf{j} = -\mathbf{M}(c, T) \left(\nabla \mu + \beta \nabla T \right) \,, \tag{2.42}$$

$$\mathbf{q} = -\boldsymbol{\Lambda} \nabla T \,, \tag{2.43}$$

where $\mathbf{K}$ is the electric conductivity in tensor form, $\mathbf{M}$ is the ion mobility tensor, β is a parameter related to the thermomigration of the species[2], and $\boldsymbol{\Lambda}$ is the heat conductivity tensor. $\mathbf{M}$ is in general a function of concentration and temperature. In our work, we ignore β, which is common in the modeling of solids that we are interested in. We assume isotropic functional forms for the electric conductivity, ionic mobility, and heat conduction tensors,

$$\mathbf{K} = \kappa \mathbf{1} \,, \tag{2.44}$$

$$\mathbf{M} = \frac{Dc}{RT} \mathbf{1} \,, \tag{2.45}$$

$$\boldsymbol{\Lambda} = \lambda \mathbf{1} \tag{2.46}$$

where κ is the material specific electric conductivity [S/m], D is the diffusion coefficient of lithium in the solid material [m^2/s], λ is the thermal conductivity [W/m $\cdot$ K], and $R = 8.314 \, \text{J/K} \cdot \text{mol}$ is the universal gas constant. $\mathbf{K}$, $\mathbf{M}$, and $\boldsymbol{\lambda}$ need to be positive semi-definite

---

[2]β is related to the Soret effect in which a temperature gradient induces atoms to diffuse in a certain manner. Positive thermodiffusion occurs when atoms move from high to low temperatures, and negative thermodiffusion is also possible depending on the species. This effect is commonly ignored in solids and will be ignored in our work as well. Note Latz and Zausch (2011) and Latz and Zausch (2015) take the Soret effect into account in their formulations.

tensors for Equation (2.36) to hold. Therefore, κ, D, and λ are required to be greater than or equal to zero as c and T already hold this property.

We postulate the free energy density with linear kinematics and ideal solution behavior. This mimics Bucci, Y.M., and Carter (2016) and Bower, Guduru, and Sethuraman (2011) using finite deformation theory and non-ideal solution behavior. The Helmholtz free energy of the system is

$$\rho\psi\left(\boldsymbol{\varepsilon}_{mech}, c, \mathbf{D}, T\right) = \frac{1}{2}\boldsymbol{\varepsilon}_{mech} : \mathbb{C} : \boldsymbol{\varepsilon}_{mech} + \mu_0 c + RTc\ln(c) + zFc\phi + \frac{1}{\epsilon}\mathbf{D}\cdot\mathbf{D}, \quad (2.47)$$

where μ_0 is the reference chemical potential, z is the valency of the material, and $\mathbb{C}$ is the elastic moduli tensor [N/m^2]. This specific form of the free energy only considers the lithium interaction with the material and neglects lithium diffusion or mixing with other species. Therefore, taking gradients of ψ defines the primary constitutive equations for the stress, chemical potential, and electric field, respectively:

$$\boldsymbol{\sigma} = \mathbb{C} : \boldsymbol{\varepsilon}_{mech} + \boldsymbol{\sigma}^M, \quad (2.48)$$

$$\mu = \mu_0 + RT\left(\ln(c) + 1\right) + zF\phi + \Omega p, \quad (2.49)$$

$$\mathbf{E} = \frac{1}{\epsilon}\mathbf{D}. \quad (2.50)$$

Using appropriate substitution, we are left with the following relations

$$\boldsymbol{\sigma} = \mathbb{C} : \left[\nabla^{sym}\mathbf{u} - \frac{\Omega}{3}(c - c_{ref})\mathbf{1} - \frac{\alpha}{3}\left(T - T_0\right)\mathbf{1}\right] + \epsilon\nabla\phi \otimes \nabla\phi - \epsilon(\nabla\phi \cdot \nabla\phi)\mathbf{1},$$

$$\mathbf{i} = -\kappa\nabla\phi,$$

$$\mathbf{q} = -\lambda\nabla T,$$

$$\mathbf{j} = -D\nabla c - \frac{DzF}{RT}c\nabla\phi - \frac{D\Omega}{RT}c\nabla p.$$

Note that the chemical potential gradient does not take into account temperature gradients, as thermo-migration is not very prominent in solids. Next, we can try to simplify the stress and flux terms to determine which terms are negligible. Beginning with the Maxwell stress, we note that $\epsilon = \epsilon_R\epsilon_0$ where ϵ_0 is the permittivity of free space and ϵ_R is the relative permittivity of the medium. The relative permittivity is on the order of 10^1 and $\epsilon_0 = 8.85 \times 10^{-12}$C/V·m. For the length scale we desire to simulate, typical electric potential differences within electrodes (neglecting the electrical double layer at active particle and electrolyte interface)[3], are on the order of millivolts (10^{-3} V). Additionally, many battery electrodes have a characteristic length of 100×10^{-6} m. Therefore, a potential gradient term is $O(10^1)$ and the Maxwell stress term is on the order of 10^{-10} Pa, which is extremely small

---

[3]The electric double layer models the large potential drop between a reduced and oxidized surface in which surface charge builds up due the separation of ions and electrons from the host molecule. This results in a variation of electric potential on the scale of nanometers.

compared to mechanical, swelling, and thermal stresses that are typically on the order of MPa (Christensen, 2005). In the flux term, We approximate the order of magnitude for the terms, $z \approx 1$, $F \approx 10^5$, $R \approx 10$, $T \approx 10^2$, $c \approx 10^4$, $\Omega \approx 10^{-6}$, $\Delta p \approx 10^7$. Separately, these terms are

$$
\begin{aligned}
\Delta c &\approx 10^4 \,, \\
\frac{zF}{RT} c \Delta \phi &\approx 10^7 \,, \\
\frac{\Omega}{RT} c \Delta p &\approx 10^2 \,,
\end{aligned}
$$

where the diffusion constant and length scale Δx is common in all terms. We can see that the pressure gradient term is not significant compared to the potential gradient and diffusive terms. Therefore, the final constitutive equations that will be used for the active particle take the form:

$$
\boldsymbol{\sigma} = \mathbb{C} : \left[\nabla^{sym} \mathbf{u} - \frac{\Omega}{3}(c - c_{ref})\mathbf{1} - \frac{\alpha}{3}(T - T_0)\mathbf{1} \right] , \tag{2.51}
$$

$$
\mathbf{j} = -D\nabla c - \frac{DzF}{RT} c \nabla \phi \,, \tag{2.52}
$$

$$
\mathbf{i} = -\kappa \nabla \phi \,, \tag{2.53}
$$

$$
\mathbf{q} = -\lambda \nabla T \,. \tag{2.54}
$$

One can visualize the nonlinearity in the second term for the ionic flux. The concentration c is not only multiplied by the potential gradient $\nabla \phi$ but also divided by the temperature T. The remaining constitutive relations, however, are affine with respect to the independent variables.

2.2.2 Electrolyte

This section derives the electrolyte constitutive equations, which are based on previous literature (Hariharan, Tagade, and Ramachandran, 2018; Smith and Bazant, 2017; Newman and Tiedemann, 1975). The following assumptions are used.

1. We model a binary lithium salt comprised of a cation and anion with valency z_i, which are dissolved in a solution mixture.

2. The simulation of the electrolyte is at a length scale large enough so that any molecular polarization effects can be neglected and electroneutrality can be used.

3. Pressure and thermal gradient effects are also neglected in the gradient of the chemical potential.

For a given ion i in solution, the chemical potential is

$$\mu_i = \mu_{0i} + RT \ln(a_i) + z_i F \phi, \tag{2.55}$$

where z_i is the valency of the corresponding ion and a_i is the activity of the ion. The activity can be decomposed in terms of an activity coefficient γ_i and the molar concentration c_i,

$$\mu_i = \mu_{0i} + RT \left[\ln \gamma_i + \ln c_i\right] + z_i F \phi. \tag{2.56}$$

As derived in the previous section, the driving force for the migration of ions is the gradient of the chemical potential,

$$\nabla \mu_i = RT \left[\nabla \ln c_i + \nabla \ln \gamma_i\right] + z_i F \nabla \phi. \tag{2.57}$$

One can rewrite this expression in terms of partial derivatives of the activity coefficient,

$$\nabla \mu_i = RT \frac{\nabla c_i}{c_i} \left[1 + \frac{\partial \ln \gamma_i}{\partial \ln c_i}\right] + z_i F \nabla \phi. \tag{2.58}$$

The ionic flux is then related to the chemical potential by the relation

$$\mathbf{j}_i = -M_i(c_i, T) \nabla \mu_i, \tag{2.59}$$

$$\mathbf{j}_i = -\frac{D_i}{RT} c_i \nabla \mu_i, \tag{2.60}$$

$$\mathbf{j}_i = -D_i^{eff} \nabla c_i - \frac{D_i z_i F}{RT} c_i \nabla \phi, \tag{2.61}$$

with $D_i^{eff} = D_i \left[1 + \frac{\partial \ln \gamma_i}{\partial \ln c_i}\right]$. The electric current associated with each ion is given as

$$\mathbf{i}_i = z_i F \mathbf{j}_i, \tag{2.62}$$

$$\mathbf{i}_i = -z_i F D_i^{eff} \nabla c_i - \kappa_i \nabla \phi, \tag{2.63}$$

where $\kappa_i = (z_i F)^2 c_i \frac{D_i}{RT}$ is the effective electronic conductivity of the ion. The total electric current is obtained by the sum of the individual current fluxes $\mathbf{i} = \sum_i \mathbf{i}_i$. By utilizing the electroneutrality and binary salt assumption, $\sum_i z_i F c_i = 0$, one is able to find that at any given point the concentration of the cation mixed in solution is equal to the concentration of the anion, $c_+ = c_-$. Denoting the lithium concentration simply as c, the total electric current is

$$\mathbf{i} = -\kappa_{eff} \nabla \phi - \nabla \ln c \frac{RT}{F} \sum_i \frac{\kappa_i}{z_i} \left[1 + \frac{\partial \ln \gamma_i}{\partial \ln c_i}\right], \tag{2.64}$$

with $\kappa_{eff} = \sum_i \kappa_i$, which is a measurable property of the electrolyte and is more applicable. This expression can also be written in terms of the individual diffusion constants of the ions,

$$\mathbf{i} = -\frac{F^2 c}{RT} \nabla \phi \sum_i z_i^2 D_i - F \nabla c \sum_i z_i D_i. \tag{2.65}$$

One can define the transference number in terms of the conductivities, $t_i = \frac{\kappa_i}{\kappa_{eff}}$. The transference number relates the amount of charge carried by the particular ion. For a binary electrolyte, which is common for lithium ion battery solutions, $z_+ = +1$ and $z_- = -1$. The mean molar activity coefficient is defined as

$$\gamma_\pm = \sqrt{\gamma_+ \gamma_-} \, , \tag{2.66}$$

which simplifies the expression above to

$$\begin{aligned}
\mathbf{i} = -\kappa_{eff}\nabla\phi + \nabla\ln c \frac{RT\kappa_{eff}}{F}\left(2(1-t_+)\left[1 + \frac{\partial\ln\gamma_\pm}{\partial\ln c}\right]\right) \\
- \nabla\ln c\frac{RT\kappa_{eff}}{F}\left[1 + \frac{\partial\ln\gamma_+}{\partial\ln c}\right] .
\end{aligned} \tag{2.67}$$

For binary electrolytes in lithium cells, the transference number can also be defined in terms of the diffusivities as $t_i = \frac{D_i}{D}$ with $D = D_+ + D_-$ leading to

$$\mathbf{i} = -\kappa_{eff}\nabla\phi + \nabla\ln c\frac{RT\kappa_{eff}}{F}\left(2(1-t_+)\left[1 + \frac{\partial\ln\gamma_\pm}{\partial\ln c}\right]\right) - DF\nabla c\left[1 + \frac{\partial\ln\gamma_+}{\partial\ln c}\right] . \tag{2.68}$$

The last term can be written in terms of the cation chemical potential gradient $\nabla\mu_+$,

$$\mathbf{i} = -\kappa_{eff}\nabla\phi + \nabla\ln c\frac{RT\kappa_{eff}}{F}\left(2(1-t_+)\left[1 + \frac{\partial\ln\gamma_\pm}{\partial\ln c}\right]\right) - \frac{Fc}{RT}D\nabla\mu_+ . \tag{2.69}$$

In modeling the electric current, the last term is traditionally neglected in comparison to the other terms (Hariharan, Tagade, and Ramachandran, 2018), as one assumes that the flux generated due to the coupling between the total diffusivity to the cation chemical potential gradients is negligible. Thus, the total current and associated flux are

$$\mathbf{i} = -\kappa_{eff}\nabla\phi + \nabla\ln c\frac{RT\kappa_{eff}}{F}\left(2(1-t_+)\left[1 + \frac{\partial\ln\gamma_\pm}{\partial\ln c}\right]\right) , \tag{2.70}$$

$$\mathbf{j} = -D_+^{eff}\nabla c - \frac{D_+ F}{RT}c\nabla\phi , \tag{2.71}$$

with D_+ being the lithium diffusion coefficient in the electrolyte solvent.

Considering the mechanical properties, we will assume that the liquid electrolyte filling the pores in the electrode can be modeled as a solid. Realistic battery operating conditions do not yield any significant accelerations or velocity gradients. The motion of the liquid electrolyte follows the swelling of the surrounding active particles. This simplifies the model, but also is also a limitation. We are not accurately depicting the quantitative flow of the electrolyte or considering any strain rate dependence, which could physically occur under certain conditions. Lastly, as in the active particle case, the heat flux is still assumed to be isotropic and flows in the opposite direction of the temperature gradient. Therefore, the final two constitutive laws for the electrolyte are the same form as the active particle,

$$\boldsymbol{\sigma} = \mathbb{C} : \left[\frac{1}{2}\left(\nabla\mathbf{u} + \nabla\mathbf{u}^T\right) - \frac{\Omega}{3}(c - c_{ref})\mathbf{1} - \frac{\alpha}{3}(T - T_0)\mathbf{1}\right] , \tag{2.72}$$

$$\mathbf{q} = -\lambda\nabla T . \tag{2.73}$$

2.2.3 Reaction Kinetics

During charging, the applied electric current raises the potential energy of the cathode putting the cell in a non-equilibrium state, see Bazant (2012) for reference. Initially, this raises the electric potential of the cathode active particle higher than that of its equilibrium potential with the surrounding electrolyte which then oxidizes the neutral lithium ions in the cathode. This forces the lithium ions to leave the active particle and react with the electrolyte solution. This reaction causes a potential difference and concentration gradient in the electrolyte forcing lithium ions to flow towards the anode. At the anode's active particle surface, the lithium ions combine with free electrons, which are simultaneously released from the oxidation reaction occurring at the surface of cathode material particles. Electrons are shuttled through the electrical circuitry connecting the current collectors. This generates an incoming flux of lithium ions entering the anode active particle. Continued charging will essentially deplete the cathode's source of lithium ions and electrons, while the anode hopefully reaches its full capacity. This is the idealized scenario and is more complicated in realistic settings. Considering the anode's active particle surface during charging, there are essentially three main reactions that can occur:

1. lithium intercalation into the active particle,

2. plating of lithium metal,

3. and reduction of electrolyte compounds resulting in SEI formation.

Figure (2.1) below depicts lithium ions in orange circles and the three reactions that we seek to model.
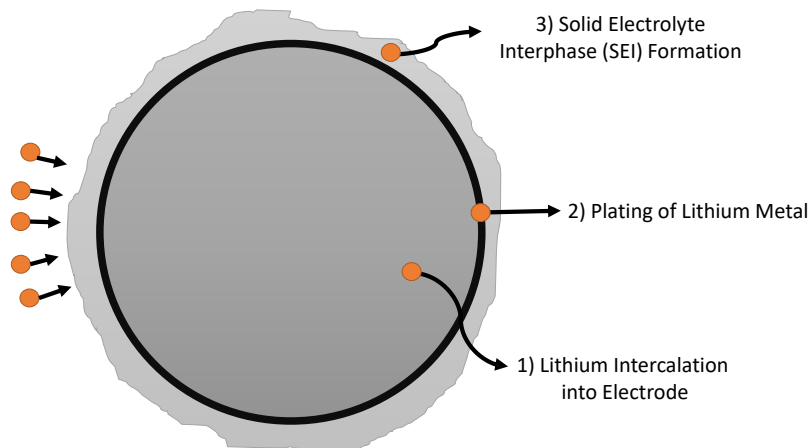
Figure 2.1: Figure of possible chemical reactions: 1) lithium intercalation into the electrode atomic structure, 2) metallic deposition, or 3) the formation of the solid electrolyte interphase.

As described before, the desired reaction is lithium intercalation, but initial SEI formation is inevitable. Lithium plating typically occurs after a full SEI layer has formed, and is formed immediately adjacent to the active particle's surface.[4] In a simplified setting with a graphitic anode, each reaction is chemically described by the following equations,

$$xLi^+ + C_6 + xe^- \rightleftharpoons Li_xC_6 \qquad \text{(Intercalation)}$$
$$Li^+ + e^- \rightarrow Li(s) \qquad \text{(Plating)}$$
$$\delta C + \alpha Li^+ + R \rightarrow RLi_\alpha C_\delta \qquad \text{(SEI)}$$
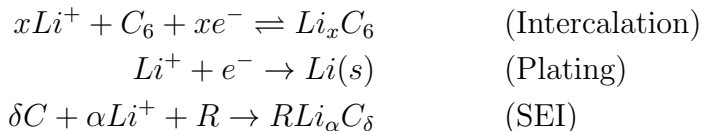
with R being an arbitrary electrolyte solute that reacts with the lithium to form the SEI (Yang et al., 2017). Following previous works of Safari et al. (2009) and Kindermann et al. (2017) among others, we can mathematically model each of these reactions by a Butler-Volmer expression. Butler-Volmer reaction kinetics are based on an Arrhenius relation for the activation energy required for forward and reverse reactions to occur. An assumption is made on the minimum energy required for the reaction coordinate to surpass an appropriate transition state. Traditionally, this assumption is that the work required is linearly dependent on the electrical work's contribution to the Gibbs energy. Bazant (2012) provide an extensive review on chemical kinetics and further extends their non-equilibrium theory for including mechanical strain effects on the reaction rate (Cogswell and Bazant, 2012).

We will now focus on the the modeling of the intercalation reaction. In each of the following equations, c_S and ϕ_S will denote the concentration and potential of lithium ions at the active particle's surface, and c_E and ϕ_E will denote the concentration and potential of lithium ions at the electrolyte's surface. Both surfaces are adjacent to one another and are located at the particle-electrolyte interface. The intercalation reaction rate is primarily driven by the reaction rate constant k_R and the surface overpotential η given by

$$\eta = \phi_S - \phi_E - U_0(c_S, T) - i_T R_{film} \,. \tag{2.74}$$

Here U_0 is the measured half cell open circuit voltage, i_T is the total electric current flowing through the film interface, and R_{film} is the electrical resistance of the film interface. The open circuit voltage U_0 is a function of active particle surface lithium concentration and temperature. U_0 relates the equilibrium potential value of an electrode half cell at a specified concentration. Historically, there are many variants of the Butler-Volmer equation to describe lithium intercalation/de-intercalation as shown in Falconi (2017). Each expression is based on slight variances in energy landscape assumptions, and proposed functional forms

---

[4]This is for typical charging rates. Higher charging rates or low temperatures increase the reaction kinetics of plating compared to the intercalation rate, which will result in lithium plating or dendrite formation even in the first few charging cycles (Tippmann et al., 2014).

for a positive intercalation reaction are

$$R_{BV}^{(1)} = k_R^{(1)}\sqrt{c_E}\sqrt{c_S}\sqrt{c_S^{max} - c_S}\left[\exp\left(-\frac{\alpha z F}{RT}\eta\right) - \exp\left(\frac{(1-\alpha)zF}{RT}\eta\right)\right], \qquad (2.75)$$

$$R_{BV}^{(2)} = k_R^{(2)}c_S^{max}c_E^{\alpha}\left[\frac{c_E}{c_{E0}}(1 - \frac{c_S}{c_S^{max}})\exp\left(\frac{-\alpha z F}{RT}\eta\right) - \frac{c_S}{c_S^{max}}\exp\left(\frac{(1-\alpha)zF}{RT}\eta\right)\right] \quad (2.76)$$

$$R_{BV}^{(3)} = k_R^{(3)}\left(c_S^{max} - c_S\right)^{\alpha}c_S^{1-\alpha}c_{E0}^{\alpha}\left[\frac{c_E}{c_{E0}}\exp\left(\frac{-\alpha z F}{RT}\eta\right) - \exp\left(\frac{(1-\alpha)zF}{RT}\eta\right)\right], \quad (2.77)$$

where c_{E0} [mol/m^3] is the initial lithium ion concentration in the electrolyte, c_S^{max} is the maximum lithium concentration in the active particle, and α is a unitless factor depicting if the forward or reverse reaction is favored. Commonly, $\alpha = 1/2$ and these equations can be simplified. Each final expression $R_{BV}^{(1)}$, $R_{BV}^{(2)}$, and $R_{BV}^{(3)}$ have the same units of [mol/m^{2}s], but have varying units for the reaction rates. Given the definition for each $R_{BV}^{(i)}$, $[k_R^{(1)}] = $ [m$^{5/2}/\sqrt{\text{mol}} \cdot$ s], $[k_R^{(2)}] = $ [m$^{1+3\alpha}$/mol$^{\alpha}$s], and $[k_R^{(3)}] = $ [m$^{1+3\alpha}$/mol$^{\alpha}$s]. They are all valid expressions for modeling the intercalation reaction, but we choose to work with Equation (2.75) as it is most commonly seen in the literature.

In modeling the SEI reaction and lithium plating, we describe these reactions by additional Butler-Volmer expressions. Previous works of Yang et al. (2017), Pinson and Bazant (2013), and Kindermann et al. (2017) utilize porous electrode theory in conjunction with side reactions occurring at the anode active particle and electrolyte interface. Since porous electrode models describe the active particle and electrolyte simultaneously at the same material point, then their junctions are consequently occurring at every spatial point and are modeled accordingly. Our work does not assume this as the electrode particles and electrolyte will be separated geometrically. The rate of SEI formation is dependent on the solute surface concentration of the electrolyte solvent, initial reaction rate constant, and equilibrium potential of the SEI reduction compound. The SEI reaction is

$$R_{SEI} = -k_{0,SEI}C_{EC}^S \exp\left[-\frac{\alpha_{C,SEI}zF}{RT}\left(\phi_S - \phi_E - U_{SEI} - i_T R_{film}\right)\right], \qquad (2.78)$$

where $k_{0,SEI}$ [m/s] is the initial reaction rate constant, C_{EC}^S [mol/m^3] is the surface concentration of the solute dissolved in the electrolyte solvent, z is the valency of the SEI compound formed, and U_{SEI} is the equilibrium potential of this compound. However, the equilibrium potential of the SEI is not consistent in the literature (Safari et al., 2009). Common values are in the range of $U_{SEI} = \{0.2, 2.0\}$ V with respect to Li$^+$/Li(s). Chapter 16 of the Handbook of Battery Materials (Daniel and Besenhard, 2011) is a great source for various reduction potentials of SEI compounds. Since we are assuming the surface concentration of the electrolyte solvent is constant, we add in an exponential decaying factor dependent on the SEI film thickness to model the decrease in the reaction rate as the SEI layer grows,

which mimics Lin et al. (2013). The final reaction rate then becomes,

$$R_{SEI} = -\exp\left(-\lambda_{SEI}\delta_{SEI}\right) k_{0,SEI} C_{EC}^{S} \exp\left[-\frac{\alpha_{C,SEI}zF}{RT}\left(\phi_S - \phi_E - U_{SEI} - i_T R_{film}\right)\right],$$
(2.79)

where λ_{SEI} [1/m] is the decay factor specifically for SEI growth and δ_{SEI} [m] is the thickness of the SEI layer.

Lithium plating is assumed to be dependent on solely surface kinetics and the variation of the overpotential with respect to lithium's equilibrium potential. We also assume an exponential decay factor that is dependent on the thickness of the deposited lithium layer, which was done in Lin et al. (2013) for SEI grow, hydrogen ion accumulation, and cathode dissolution. The plating reaction is considered as

$$R_{plate} = -\exp\left(-\lambda_{plate}\delta_{plate}\right) k_{0,plate} \exp\left[-\frac{\alpha_{C,plate}F}{RT}\left(\phi_S - \phi_E - i_T R_{film}\right)\right],$$
(2.80)

where the equilibrium potential of pure lithium is taken to be zero (Ge et al., 2017).[5] In Equation (2.80), λ_{plate} [1/m] is the decay factor specifically for the plating reaction, δ_{plate} [m] is the thickness of plated lithium at the surface, and $k_{0,plate}$ [mol/m^{2}s] is the initial reaction rate of lithium plating.

Note that both reactions use a cathodic approximation[6] and are a consumption of lithium ions hence the negative signs. The surface concentration change of the SEI and lithium can be found by a material balance at the interface,

$$\frac{\partial c_{SEI}}{\partial t} = -R_{SEI} - R_{plate}\beta\,,$$
(2.81)

$$\frac{\partial c_{plate}}{\partial t} = -R_{plate}(1 - \beta)\,,$$
(2.82)

with β being a parameter controlling the amount of plated lithium reacting with the surrounding electrolyte and converting into the SEI compound. Both concentrations are calculated with unit thickness such that each yield units of [mol/m^2]. The total film thickness $\delta_{film} = \delta_{SEI} + \delta_{plate}$ can be found by the surface concentration of SEI and lithium metal,

$$\delta_{film} = \underbrace{\frac{c_{SEI}M_{SEI}}{\rho_{SEI}}}_{\delta_{SEI}} + \underbrace{\frac{c_{plate}M_{plate}}{\rho_{plate}}}_{\delta_{plate}}\,,$$
(2.83)

where M_i and ρ_i are the molar mass and density of the species i. Lastly, we assume that the electrical resistance will only be dependent on the conductivity of the SEI and film thickness,

$$R_{film} = \omega_{SEI}\frac{\delta_{film}}{\kappa_{SEI}}\,,$$
(2.84)

---

[5]It is common in the battery literature that potentials are defined in reference to pure lithium.

[6]A cathode reaction is one in which the reduction of compounds occurs. We can model SEI formation and lithium plating this way, so that it represents an irreversible consumption of ions and the SEI or metallic lithium does not convert back into available lithium ions for intercalation into the active particle.

with ω_{SEI} being the volume fraction of the SEI layer's mass in reference to the entire mass of the film. This neglects the metallic lithium contribution to the resistance as its electrical conductivity is much higher than that of the formed SEI compound (Yang et al., 2017). One can see that these equations are highly nonlinear especially with the voltage drop given in terms of the total electric current, which is defined as

$$i_T = F \left(R_{BV} + z R_{SEI} + R_{plate} \right) ,$$
(2.85)

where z is the valency of the reduced SEI compound. The film resistance is also proportional to the accumulated SEI concentration and yields a highly nonlinear expression in all the reaction expressions listed above. These nonlinear reactions require special implementation in the finite element code.

Chapter 3

Finite Element Method

This chapter will first discuss the necessary non-dimensionalization of the governing equations and constitutive relations given in the previous chapter. Then, we will provide an overview of the finite element method and a description on the set of user elements implemented in the software program FEAP (Taylor and Govindjee, 2020). Lastly, we will illustrate the capability of our newly defined user elements with elementary test cases.

3.1 Non-dimensional Governing Equations

A numerical solution to the above set of highly non-linear PDEs is performed using the finite element method (FEM). For the implementation into element modules, the equations are first developed in a non-dimensional form. This is motivated by the extreme range of parameters which was found to result in algebraic equations with a very large condition number. Very large condition numbers would prove the accuracy in our analyses to be useless due to numerical precision as demonstrated in Trefethen and Bau (1997). Interestingly, this problem is not discussed widely in the literature and the convergence issues with high charging rates is only briefly discussed in a few publications (Wang, Siegel, and Garikipati (2017) for example).

We utilize 6 independent variable dimensions: length (L), time (τ), molar concentration (c_{ref}), mass (M), temperature (T_{ref}), and voltage (ϕ_{ref}). The concentration variable c_{ref} differs from mass M due to the mole scale associated with it. In the subsequent section, an over bar over a variable $\bar{\cdot}$ will denote a non-dimensional parameter, such that the corresponding

variable scales are given as:

$$
\begin{aligned}
\mathbf{x} &= L\bar{\mathbf{x}}, \\
t &= \tau\bar{t}, \\
c &= c_{ref}\bar{c}, \\
m &= M\bar{m}, \\
T &= T_{ref}\bar{T}, \\
\phi &= \phi_{ref}\bar{\phi}.
\end{aligned}
$$

The resulting displacement vector and operators then yield,

$$
\begin{aligned}
\mathbf{u} &= L\bar{\mathbf{u}}, \\
\frac{\partial}{\partial\mathbf{x}} &= \frac{1}{L}\frac{\partial}{\partial\bar{\mathbf{x}}}, \\
\nabla &= \frac{1}{L}\bar{\nabla}.
\end{aligned}
$$

The governing equations from the previous section have the same form except given in their non-dimensional counterparts,

$$
\bar{\rho}\bar{\mathbf{b}} + \bar{\nabla}\cdot\bar{\boldsymbol{\sigma}} = \bar{\rho}\frac{\partial^2\bar{\mathbf{u}}}{\partial\bar{t}^2}, \tag{3.1}
$$

$$
\frac{\partial\bar{c}}{\partial\bar{t}} + \bar{\nabla}\cdot\bar{\mathbf{j}} = \bar{0}, \tag{3.2}
$$

$$
\bar{\nabla}\cdot\bar{\mathbf{i}} = \bar{0}, \tag{3.3}
$$

$$
\bar{\rho}\bar{C}_p\frac{\partial\bar{T}}{\partial\bar{t}} + \bar{\nabla}\cdot\bar{\mathbf{q}} = \bar{h}. \tag{3.4}
$$

With careful algebra the remaining relations are given as,

$$
\bar{\mathbf{b}} = \frac{L^2\tau^2}{M}\mathbf{b}, \tag{3.5a}
$$

$$
\frac{\partial^2\bar{\mathbf{u}}}{\partial\bar{t}^2} = \frac{\tau^2}{L}\frac{\partial^2\mathbf{u}}{\partial t^2}, \tag{3.5b}
$$

$$
\bar{\rho} = \frac{L^3}{M}\rho, \tag{3.5c}
$$

$$
\bar{C}_p = \frac{\tau^2}{ML^2}C_p. \tag{3.5d}
$$

The constitutive laws are given below and slightly vary for the active particle and electrolyte cases. Since the stress, strain, ionic flux, and thermal flux are the same for both materials, they are computationally modeled by the same non-dimensional formulation with the exception of the electric current and heat source terms. See the relations below for a complete list of non-dimensional properties. For the active particle, the new relations are shown below.

- Mechanical variables:

$$
\begin{aligned}
\bar{\boldsymbol{\sigma}} &= \bar{\mathbb{C}} : \boldsymbol{\varepsilon} \\
\bar{\mathbb{C}} &= \frac{L\tau^2}{M}\mathbb{C} \\
\boldsymbol{\varepsilon} &= \frac{\partial^{sym}\bar{\mathbf{u}}}{\partial\bar{\mathbf{x}}} - \frac{\bar{\Omega}}{3}\bar{c}\mathbf{1} - \frac{\bar{\alpha}}{3}(\bar{T} - \bar{T}_0)\mathbf{1} \\
\bar{\Omega} &= \Omega c_{ref} \\
\bar{\alpha} &= \alpha T_{ref}
\end{aligned}
$$

- Concentration variables:

$$
\begin{aligned}
\bar{\mathbf{j}} &= -\bar{D}_c\frac{\partial\bar{c}}{\partial\bar{\mathbf{x}}} - \bar{D}_\phi\frac{\bar{c}}{\bar{T}}\frac{\partial\bar{\phi}}{\partial\bar{\mathbf{x}}} \\
\bar{D}_c &= \frac{D\tau}{L^2} \\
\bar{D}_\phi &= \frac{D\tau}{L^2}\frac{zF\phi_{ref}}{RT_{ref}}
\end{aligned}
$$

- Potential variables:

$$
\begin{aligned}
\bar{\mathbf{i}} &= -\bar{\kappa}\frac{\partial\bar{\phi}}{\partial\bar{\mathbf{x}}} \\
\bar{\kappa} &= \frac{\phi_{ref}^2\tau^3}{ML}\kappa
\end{aligned}
$$

- Temperature variables:

$$
\begin{aligned}
\bar{\mathbf{q}} &= -\bar{\lambda}\frac{\partial\bar{T}}{\partial\bar{\mathbf{x}}} \\
\bar{\lambda} &= \frac{\tau^3}{M^2L}\lambda \\
\bar{h} &= \bar{h}_\phi\frac{\partial\bar{\phi}}{\partial\bar{\mathbf{x}}}\cdot\frac{\partial\bar{\phi}}{\partial\bar{\mathbf{x}}} \\
\bar{h}_\phi &= \frac{\kappa\tau^3\phi_{ref}^2}{T_{ref}LM^2}
\end{aligned}
$$

For the electrolyte material, the non-dimensional constitutive relations are shown below.

- Mechanical variables:

$$\begin{aligned}
\bar{\boldsymbol{\sigma}} &= \bar{\mathbb{C}} : \boldsymbol{\varepsilon} \\
\bar{\mathbb{C}} &= \frac{L\tau^2}{M}\mathbb{C} \\
\boldsymbol{\varepsilon} &= \frac{\partial^{sym}\bar{\mathbf{u}}}{\partial\bar{\mathbf{x}}} - \frac{\bar{\Omega}}{3}\bar{c}\mathbf{1} - \frac{\bar{\alpha}}{3}(\bar{T} - \bar{T}_0)\mathbf{1} \\
\bar{\Omega} &= \Omega c_{ref} \\
\bar{\alpha} &= \alpha T_{ref}
\end{aligned}$$

- Concentration variables:

$$\begin{aligned}
\bar{\mathbf{j}} &= -\bar{D}_c\frac{\partial\bar{c}}{\partial\bar{\mathbf{x}}} - \bar{D}_\phi\frac{\bar{c}}{\bar{T}}\frac{\partial\bar{\phi}}{\partial\bar{\mathbf{x}}} \\
\bar{D}_c &= \frac{D_+^{eff}\tau}{L^2} \\
\bar{D}_\phi &= \frac{D_+\tau}{L^2}\frac{zF\phi_{ref}}{RT_{ref}}
\end{aligned}$$

- Potential variables:

$$\begin{aligned}
\bar{\mathbf{i}} &= -\bar{\kappa}_{eff}\frac{\partial\bar{\phi}}{\partial\bar{\mathbf{x}}} + \bar{\kappa}_D\frac{\bar{T}}{\bar{c}}\frac{\partial\bar{c}}{\partial\mathbf{x}} \\
\bar{\kappa}_{eff} &= \frac{\phi_{ref}^2\tau^3}{ML}\kappa_{eff} \\
\bar{\kappa}_D &= 2(1-t_+)\left(1 + \frac{\partial\ln\gamma_\pm}{\partial\ln c}\right)\frac{R\kappa_{eff}}{F}\frac{\phi_{ref}T_{ref}\tau^3}{ML}
\end{aligned}$$

- Temperature variables:

$$\begin{aligned}
\bar{\mathbf{q}} &= -\bar{\lambda}\frac{\partial\bar{T}}{\partial\bar{\mathbf{x}}} \\
\bar{\lambda} &= \frac{\tau^3}{M^2L}\lambda \\
\bar{h} &= \bar{h}_\phi\frac{\partial\bar{\phi}}{\partial\bar{\mathbf{x}}}\cdot\frac{\partial\bar{\phi}}{\partial\bar{\mathbf{x}}} + \bar{h}_C\frac{\bar{T}}{\bar{c}}\frac{\partial\bar{c}}{\partial\bar{\mathbf{x}}}\cdot\frac{\partial\bar{\phi}}{\partial\bar{\mathbf{x}}} \\
\bar{h}_\phi &= \frac{\kappa_{eff}\tau\phi_{ref}^2}{\rho C_p L^2 T_{ref}} \\
\bar{h}_C &= 2(1-t_+)\left(1 + \frac{\partial\ln\gamma_\pm}{\partial\ln c}\right)\frac{R\kappa_{eff}}{F}\frac{\phi_{ref}\tau^3}{M^2L}
\end{aligned}$$

Albeit the relations above are quite cumbersome to deal with, the treatment of the extra multiplicative factors in the code is fairly straight forward. Lastly, one needs to employ the appropriate non-dimensional traction and flux boundary conditions for consistency,

$$\bar{\mathbf{t}} = \frac{L\tau^2}{M}\mathbf{t}, \tag{3.6}$$

$$\bar{\mathbf{j}} = \frac{\tau}{c_{ref}L}\mathbf{j}, \tag{3.7}$$

$$\bar{\mathbf{i}} = \frac{\phi_{ref}\tau^3}{M}\mathbf{i}, \tag{3.8}$$

$$\bar{\mathbf{q}} = \frac{\tau^3}{M^2 T_{ref}}\mathbf{q}. \tag{3.9}$$

These relations are needed in the interface elements that incorporate the Butler-Volmer intercalation reaction along with SEI growth and lithium plating. We consider Equation (2.75) in our interface elements, since it is the most common form used in the literature (Cogswell and Bazant, 2012). We assume a symmetry factor of $\alpha = 1/2$ and a valency of $z = 1$, which describes lithium ion intercalation. These variables simplify Equation (2.75) to a hyperbolic sine function,

$$R_{BV} = k_R\sqrt{c_E}\sqrt{c_S}\sqrt{c_S^{max} - c_S} \cdot \left[\exp\left(\frac{-F\eta}{2RT}\right) - \exp\left(\frac{F\eta}{2RT}\right)\right],$$

$$R_{BV} = 2k_R\sqrt{c_E}\sqrt{c_S}\sqrt{c_S^{max} - c_S} \cdot \sinh\left(\frac{-F\eta}{2RT}\right),$$

where $\eta = \phi_S - \phi_E - U_0(c_S, T) - i_T R_{film}$. Using the odd function properties of the hyperbolic sine function, its functional form in terms of the non-dimensional variables defined above is

$$R_{BV} = -2k_R c_{ref}^{3/2}\sqrt{\bar{c}_E}\sqrt{\bar{c}_S}\sqrt{\frac{c_S^{max}}{c_{ref}} - \bar{c}_S} \cdot \sinh\left(\frac{F\phi_{ref}}{2RT_{ref}}\frac{\bar{\eta}}{\bar{T}}\right), \tag{3.10}$$

where

$$\bar{\eta} = \bar{\phi}_S - \bar{\phi}_E - \frac{U_0}{\phi_{ref}} - \frac{i_T R_{film}}{\phi_{ref}}. \tag{3.11}$$

The reaction rates for SEI growth and lithium deposition in terms of non-dimensional variables $\bar{T}$ and $\bar{\phi}$ are,

$$R_{SEI} = -\exp\left(-\lambda_{SEI}\delta_{SEI}\right)k_{0,SEI}C_{EC}^S\exp\left(-\frac{\alpha_{C,SEI}zF\phi_{ref}}{RT_{ref}}\frac{\bar{\eta}_{SEI}}{\bar{T}}\right), \tag{3.12}$$

$$R_{plate} = -\exp\left(-\lambda_{plate}\delta_{plate}\right)k_{0,plate}\exp\left(-\frac{\alpha_{C,plate}F\phi_{ref}}{RT_{ref}}\frac{\bar{\eta}_{plate}}{\bar{T}}\right), \tag{3.13}$$

with the overpotentials defined as

$$
\begin{aligned}
\bar{\eta}_{SEI} &= \bar{\phi}_S - \bar{\phi}_E - \frac{U_{SEI}}{\phi_{ref}} - \frac{i_T R_{film}}{\phi_{ref}}, \\
\bar{\eta}_{plate} &= \bar{\phi}_S - \bar{\phi}_E - \frac{i_T R_{film}}{\phi_{ref}}.
\end{aligned}
$$

Note that Equations (3.10), (3.12), and (3.12) still have units of flux [mol/m^{2}s], and the relations given in Equations (3.6)-(3.8) are utilized for consistent constitutive relations. For example, one would need to multiply Equation (3.10) by $\tau/c_{ref}L$ to yield a unit-less reaction, i.e. $\bar{R}_{BV} = (\tau/c_{ref}L) R_{BV}$.

3.2 Weak Form

This section derives and discuses the finite element discretization of Equations (3.1) - (3.4). In the subsequent sections, we neglect the use of the over-bar on any variable for better clarity, but please note that all variables used are non-dimensional as described in the previous section. To obtain the weak form, we multiply each equation by a corresponding test function, integrate over the domain, and then appropriately apply the divergence theorem (see Ch.3 in Zienkiewicz, Taylor, and Zhu (2013)). We define the test function set as $\{\delta\mathbf{u}, \delta c, \delta\phi, \delta T\}$, the domain as P, the entire boundary of the domain as ∂P, and the unit normal pointing outward of the boundary's domain as $\mathbf{n}$. The corresponding weak form equations are:

$$
\mathbf{R}_1 = \int_{\partial P} \delta\mathbf{u} \cdot (\boldsymbol{\sigma} \cdot \mathbf{n})\, dA + \int_P \delta\mathbf{u} \cdot \rho\mathbf{b}\, dV - \int_P \frac{\partial^{sym}\delta\mathbf{u}}{\partial\mathbf{x}} : \boldsymbol{\sigma}\, dV, \tag{3.14}
$$

$$
\mathbf{R}_2 = -\int_{\partial P} \delta c(\mathbf{j} \cdot \mathbf{n})\, dA - \int_P \delta c \frac{\partial c}{\partial t}\, dV + \int_P \frac{\partial\delta c}{\partial\mathbf{x}} \cdot \mathbf{j}\, dV, \tag{3.15}
$$

$$
\mathbf{R}_3 = -\int_{\partial P} \delta\phi(\mathbf{i} \cdot \mathbf{n})\, dA + \int_P \frac{\partial\delta\phi}{\partial\mathbf{x}} \cdot \mathbf{i}\, dV, \tag{3.16}
$$

$$
\mathbf{R}_4 = -\int_{\partial P} \delta T(\mathbf{q} \cdot \mathbf{n})\, dA + \int_P \delta T h\, dV - \int_P \delta T \rho C_p \frac{\partial T}{\partial t}\, dV + \int_P \frac{\partial\delta T}{\partial\mathbf{x}} \cdot \mathbf{q}\, dV. \tag{3.17}
$$

Equations (3.14)-(3.17) are written accordingly so they can be implemented as residual equations in a nonlinear finite element code (Zienkiewicz, Taylor, and Zhu, 2013). We currently only consider two dimensional elements that either can simulate plane strain or axisymmetric conditions. For a paritcular element, the boundary ∂P can be divided into a Dirichlet boundary ∂P_D, Neumann boundary ∂P_N, or an electrode/electrolyte interface ∂P_I. Mathematically, the boundary is decomposed as $\partial P = \partial P_D \cup \partial P_N \cup \partial P_I$. At ∂P_D, the variation is a priori set to zero and hence no flux or traction term. Additionally, the continuous variables

are approximated via piece-wise C^0 continuous shape functions evaluated at nodal points,

$$\mathbf{x} = \sum_i^{nen} N_i(\mathbf{x})\mathbf{x}_i \,,$$

$$\mathbf{u} = \sum_i^{nen} N_i(\mathbf{x})\mathbf{u}_i \,,$$

$$c = \sum_i^{nen} N_i(\mathbf{x})c_i \,,$$

$$\phi = \sum_i^{nen} N_i(\mathbf{x})\phi_i \,,$$

$$T = \sum_i^{nen} N_i(\mathbf{x})T_i \,,$$

where N_i is the shape function for node number i and nen is the total number of nodes for a particular element (see Ch.6 in Zienkiewicz, Taylor, and Zhu (2013)). The Galerkin method is used, such that the test functions utilize the same shape functions but with arbitrary nodal values:

$$\delta\mathbf{u} = \sum_i^{nen} N_i(\mathbf{x})\delta\mathbf{u}_i \,,$$

$$\delta c = \sum_i^{nen} N_i(\mathbf{x})\delta c_i \,,$$

$$\delta\phi = \sum_i^{nen} N_i(\mathbf{x})\delta\phi_i \,,$$

$$\delta T = \sum_i^{nen} N_i(\mathbf{x})\delta T_i \,.$$

Equations (3.14)-(3.17) are implemented as a set of user elements in the finite element program FEAP (Taylor and Govindjee, 2020). For our work, there are three different types of material elements corresponding to: (1) active particles, (2) electrolyte, and (3) interfacial surface elements modeling the reaction boundary conditions. The active particle and electrolyte user elements can be utilized for any given mesh and material properties. The surface elements account for the highly nonlinear Butler-Volmer expressions at any active particle and electrolyte junctions. We term these elements as "interfacial elements" due to their placement at particle/electrolyte interfaces.

3.2.1   Interface Elements

Figure 3.1 demonstrates the location of an interface element and the corresponding flux boundary conditions $\{\mathbf{j} \cdot \mathbf{n}, \mathbf{i} \cdot \mathbf{n}, \mathbf{q} \cdot \mathbf{n}\}$ applied at the adjacent nodes. These are analogous to jump boundary conditions in discontinuous numerical methods, as nodes of the active particle and electrolyte elements are separate. The interface elements are defined by the adjacent nodes to the junctions of any active particle and electrolyte elements. These interface elements have zero thickness, provide no mechanical stiffness, and only employ surface reaction kinetics condition. The surface reaction kinetics are added to the existing residual equations that exist for the active particle and electrolyte, separately.
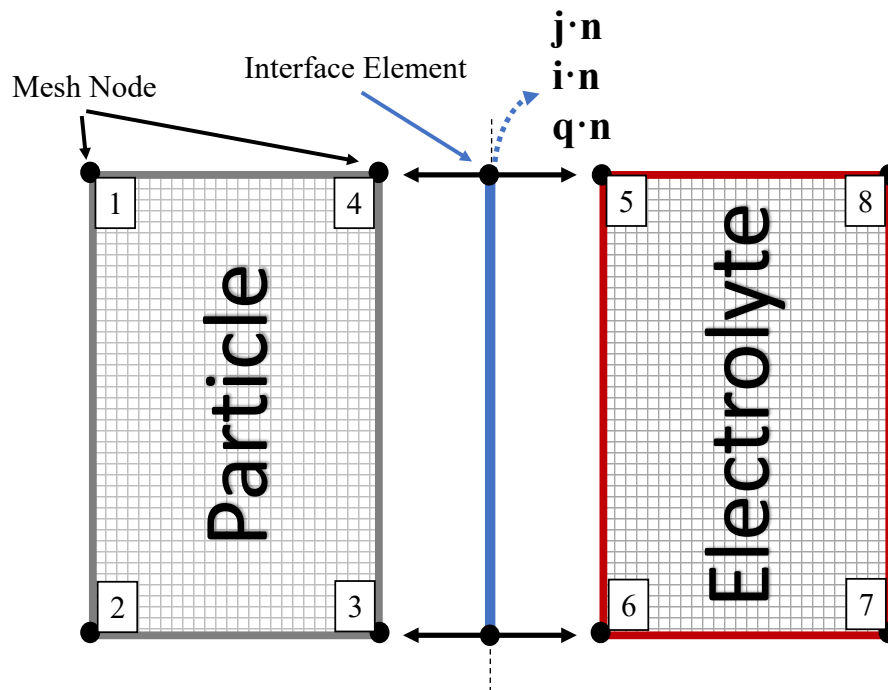
Figure 3.1: The zero thickness interface element is located at the junctions between particle and electrolyte elements and would have the [4,3,6,5] nodal values associated with it (counterclockwise nodal numbering). Computationally, nodes 4 and 5 have the same displacement $\mathbf{u}_i$ and temperature T_i nodal values, while concentration c_i and potential ϕ_i are discontinuous so that the Butler-Volmer expressions can be properly evaluated.

The interfaces are customized for specific anode and cathode materials as there is an implicit definition of the open circuit voltage coded in each. All three elements combined can then be used to describe a full battery cell omitting the modeling of the current collectors and conductive binder. The ease of changing the open circuit voltage in the Butler-Volmer elements and material parameter inputs allows one to model a wide array of full cell or half cell lithium ion batteries.

These elements utilize the nondimensional relations of Equations (3.6)-(3.8) on ∂P_I to give the flux relations in the governing weak forms. Additional boundary tractions or fluxes can occur on ∂P_N. Considering the outward normal $\mathbf{n}$ pointing from the active particle surface to the electrolyte surface, the ionic flux boundary conditions on ∂P_I are:

$$
\begin{aligned}
-\mathbf{j}_S \cdot \mathbf{n} &= R_{BV} + R_{SEI} + R_{plate}, & (3.18) \\
\mathbf{j}_E \cdot \mathbf{n} &= R_{BV}, & (3.19)
\end{aligned}
$$

where the subscripts S and E denote the active particle and electrolyte, respectively. The total flux of lithium leaving the electrolyte is just the intercalation reaction, while the flux entering the active particle is the sum of all reactions. This simulates the consumption of available lithium that was intended to enter the active particle due to the negative signs in R_{SEI} and R_{plate}. The resulting flux of ions with their corresponding valency also produces current at the surface of the particle and electrolyte, see Hariharan, Tagade, and Ramachandran (2018). This is an additional boundary condition that we have to consider. The boundary conditions for the electric current $\mathbf{i}$ are very similar as above, as there is a consumption of current needed for forming the SEI and plated Li. These boundary conditions are also in terms of the Butler-Volmer expressions and are given as,

$$
\begin{aligned}
-\mathbf{i}_S \cdot \mathbf{n} &= F\left(R_{BV} + z R_{SEI} + R_{plate}\right), & (3.20) \\
\mathbf{i}_E \cdot \mathbf{n} &= F R_{BV}. & (3.21)
\end{aligned}
$$

The electric current moving through a potential difference η generates heat. Additionally, the change in the equilibrium state U_0 of the active particle via electrical work also produces heat at the particle-electrolyte interface (see Wang (2016) or Ch.3 in Hariharan, Tagade, and Ramachandran (2018)). The resulting boundary conditions on the temperature are

$$
\begin{aligned}
-\mathbf{q}_S \cdot \mathbf{n} &= F\left(R_{BV} + z R_{SEI} + R_{plate}\right)\left(\phi_S - \phi_E - U_0 - i_T R_{film} + T\frac{\partial U_0}{\partial T}\right), & (3.22) \\
\mathbf{q}_E \cdot \mathbf{n} &= 0. & (3.23)
\end{aligned}
$$

Here, we do not specify heat generation for the electrolyte element. Because the temperature is continuous across the particle-electrolyte interface (i.e. T associated with the particle and the electrolyte nodes are the same value), we only need to specify the heat generation on one side of the interface in the code.

3.2.2 Near-incompressibility Approximation

Some battery materials are nearly-incompressible and would present numerical problems in the FEM code. These problems are attributed to the ratio of the bulk modulus K to the shear modulus μ of the material,

$$
\frac{K}{\mu} = \frac{2(1+\nu)}{3(1-2\nu)}.
$$

As the Poisson ratio $\nu \to \frac{1}{2}$, the ratio K/μ approaches infinity and causes a singularity in the constitutive relations for the Cauchy stress in terms of the displacement field. This then essentially limits the motion of the displacement degrees of freedom in a finite element mesh and results in mesh locking. Under certain conditions, the nodal mechanical degrees of freedom are fixed and unable to move appropriately. Note that this is only considering the mechanical degrees of freedom and not the concentration, electric potential, and temperature degrees of freedom in our work. Mesh locking in finite element modeling of incompressible materials is widely discussed in Hughes (2000) and Zienkiewicz, Taylor, and Zhu (2013).

There are a few common approaches in mitigating this issue and include mixed methods, penalty methods, selective reduced integration methods, and strain enhancement methods. Both mixed and penalty methods modify the variational formulation of the elastic potential energy with the addition of a constraint and a corresponding Lagrange multiplier. The constraint enforces that $\text{div}\,\mathbf{u} = 0$ if $\nu = 1/2$. In this case a newly defined constitutive relation for the Cauchy stress is needed. This typically involves the use of a pressure variable as shown in Ch. 4 of Hughes (2000).

These methods now involve seeking the solution to a separate variable in addition to the displacement field $\mathbf{u}$. The new Lagrange multiplier would be the variable that enforces the incompressibility constraint. Implementation of mixed and penalty methods are sometimes quite cumbersome. Reduced integration techniques are easier to implement as they do not require the solution to an additional variable and are proven to provide similar results.

Strain enhancement methods can also be quite cumbersome and are historically discussed in Armero (2004). We choose to use the "B-bar method" presented in Hughes (1980), which is a generalization of the mean dilation approach of Nagtegaal, Parks, and Rice (1974). The idea behind the B-bar method is to replace the volumetric contribution of the strain tensor by the average volumetric strain over the entire element. In this approach, the strain will be decomposed as

$$\bar{\varepsilon}_{ij} = \varepsilon_{ij} + \frac{1}{3} \left(\varepsilon_{vol} - \varepsilon_{kk} \right) \delta_{ij} , \tag{3.24}$$

where

$$\varepsilon_{vol} = \frac{1}{V_e} \int_{V_e} \varepsilon_{kk} \, dV , \tag{3.25}$$

and V_e is the element volume (or area in 2D). This formulation requires the use of newly defined shape functions and their derivatives to yield the corresponding strain approximation in Equation (3.24). We define N_i as the elemental piece-wise C^0 continuous shape function and $B_a = \partial N_i / \partial x_a$ as its derivative in the direction x_a. The average value $\bar{B}_a$ used in the B-bar method is defined as

$$\bar{B}_a = \frac{1}{V_e} \int_{V_e} B_a \, dV . \tag{3.26}$$

Expressions for the use of $\bar{B}_a$ to appropriately define ε_{vol} is given in Hughes (1980) for plane strain and axisymmetric conditions. These approximations only affect the displacement degrees of freedom and not the concentration, potential, or temperature nodal degrees of

freedom. In addition, it is only a utility used when incompressibility presents a significant numerical issue. More advanced treatment of incompressible materials would be to use mixed methods or other strain enhancement methods.

3.2.3 Solution Framework

To solve the coupled nonlinear system of equations, we group each residual equation into a vector $\tilde{\mathbf{R}}$ and a total displacement vector $\tilde{\mathbf{y}}$,

$$\tilde{\mathbf{R}} = \begin{bmatrix} \mathbf{R}_1 \\ \mathbf{R}_2 \\ \mathbf{R}_3 \\ \mathbf{R}_4 \end{bmatrix} \quad , \quad \tilde{\mathbf{y}} = \begin{bmatrix} \mathbf{u} \\ c \\ \phi \\ T \end{bmatrix}$$

We seek the solution to $\tilde{\mathbf{R}} = 0$ and use the Newton-Raphson method with an implicit Backward Euler time integration scheme to solve for $\tilde{\mathbf{y}}$. At each Newton iteration k, the solution variables are updated as

$$\tilde{\mathbf{y}}^{k+1} = \tilde{\mathbf{y}}^k - \left(\frac{d\tilde{\mathbf{R}}}{d\tilde{\mathbf{y}}} \right)^{-1} \Bigg|_k \cdot \tilde{\mathbf{R}}^k . \tag{3.27}$$

FEAP handles this process automatically. One needs to only specify the residual equations, stiffness relations, and corresponding nodal degrees of freedom in the user elements. Special attention is given to the growth of the SEI thickness δ_{SEI} and plating thickness δ_{plate}, which are needed to model further film growth in Equation (2.83). We treat the variables δ_{SEI}, δ_{plate}, and i_T explicitly in time. These are saved as history variables in FEAP and it greatly reduces the complication in solving for the stiffness $d\tilde{\mathbf{R}}/d\tilde{\mathbf{y}}$. Utilizing the mass balance expressions for c_{SEI} and c_{plate}, the change in film thickness for a given time step $n+1$ and time increment Δt is then equal to

$$\Delta \delta_{film}^{n+1} = \frac{-\Delta t M_{SEI}}{\rho_{SEI}} \left(R_{SEI}^n + \beta R_{plate}^n \right) - \frac{\Delta t M_{plate}}{\rho_{plate}} \left(1 - \beta \right) R_{plate}^n \tag{3.28}$$

where R_{SEI} and R_{plate} are the values at the previous time step n. The molar masses and densities are assumed to be constants.

3.3 Test Case Simulation: Active Particle User Element

We will begin the simulation section by checking the physics for the active particle user element. We seek to ensure that we obtain the correct displacement profiles for benchmark loading conditions. We are using material parameters from Wang and Garikipati (2018) for

a LiC$_6$ particle. These properties are given in Table 3.1 with the reference dimensions used in Table 3.2. A two dimensional mesh is generated with FEAP and consists of a circular active particle with 432 4-node bilinear quadrilateral elements. The solution is assumed to be two-dimensional using a plane strain condition for the elastic behavior and the computation being carried on the full mesh. The radius R is $50\,\mu$m, the initial concentration is uniform and equal to $c = 2500\,\text{mol/m}^3\,(0.1\,c_{ref})$. The initial temperature is also uniform and equal to $T_0 = 298\,\text{K}\,(1.0\,T_{ref})$ and the remaining displacements are initially set to zero. The potential and displacement are fixed at the center of the particle with additional mechanical rollers applied at the x=0 and y=0 axes to prevent rigid body rotations, i.e. $\phi(x = 0, y = 0) = 0$, $u_x(x = 0, y) = 0$, and $u_y(x, y = 0) = 0$. Figure 3.2 gives an illustration of the mesh and mechanical boundary conditions. The dashed red lines indicate the position of the mechanical rollers. Dirichlet boundary conditions are not specified for the concentration and temperature fields.

There is an applied electric current along the outer surface, which is equal to $12\,\text{A/m}^2$ with a corresponding ionic flux of $1.2437 \times 10^{-4}\,\text{mol/m}^2\text{s}$,

$$\mathbf{i} \cdot \mathbf{n} = 12\,\frac{\text{A}}{\text{m}^2},$$

$$\mathbf{j} \cdot \mathbf{n} = 1.2437 \times 10^{-4}\frac{\text{mol}}{\text{m}^2\text{s}},$$

along $\sqrt{x^2 + y^2} = R$. The flux value is chosen so that it represents 1/F of the current, which is common in the electrochemical literature to model the resulting flux of lithium ions during charging. Additionally, there are no mechanical forces or heat sources in the simulation.

We carried out the solution for a simulation time of 1 hour and evaluated the concentration, potential, displacement, and temperature profiles in time. These are shown in Figures 3.3, 3.4, 3.5, and 3.6, respectively. We qualitatively obtain the correct results with quadratic convergence as expected for the Newton-Raphson method (LeVeque, 2007). The potential field, which can be analytically solved for is radially symmetric and linear. The concentration grows as a function of time and accumulates at the outer edge. The particle's outer edge concentration reaches a maximum value of $0.942\,c_{ref}$ at the end of the 1 hour simulation. Ion motion is primarily due to the convective term in the constitutive relation, as the potential gradient forces ions to migrate towards the center of the particle. Because of the higher concentration field at the outer edges, we see larger displacements there. Due to the lithium swelling coefficient, there is a maximum surface displacement of about $2.33\,\mu$m, which corresponds to about 5% strain. This strain magnitude is reasonably common for LiC$_6$ particles. Therefore, we see that the mechanics are qualitatively accurate. It is interesting to note that the temperature did not increase at all given a fairly high electric current. This possibly could be attributed to the high specific heat of the material or lack of appropriate convection or Dirichlet boundary conditions. It should be noted that without any applied $\mathbf{q} \cdot \mathbf{n}$ boundary conditions, the particle is considered to be adiabatic. From the outputted displacement, there is about a 0.1 K uniform increase in T, which is very negligible in any battery simulation.
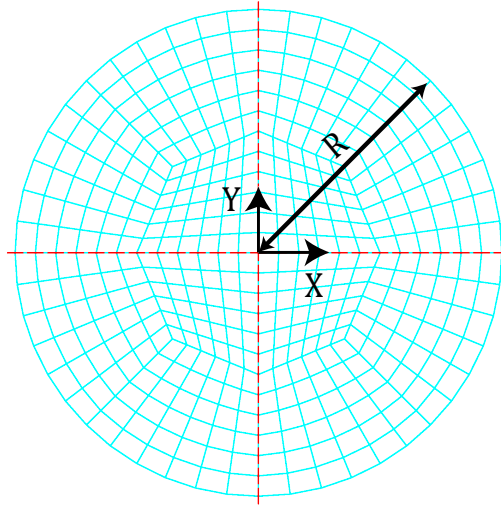
Figure 3.2: Finite element mesh in light blue with mechanical Dirichlet boundary conditions imposed in red.

Parameter	Unit	Value	Description
E	N/m^2	5.93×10^9	Young's Modulus
ν	-	0.3	Poisson ratio
ρ	kg/m^3	2.5×10^3	Density
Ω	m^3/mol	6.0×10^{-6}	Lithium swelling coefficient
α	1/K	9.615×10^{-6}	Thermal expansion coefficient
T_0	K	298.0	Initial Temperature
C_P	J/kg·K	7.0×10^2	Specific heat
λ	W/m·K	1.04	Thermal conductivity
D	m^2/s	5.0×10^{-13}	Diffusion coefficient
κ	S/m	1.5×10^2	Electrical conductivity

Table 3.1: Material parameters taken from Wang and Garikipati (2018) for LiC$_6$.

Parameter	Unit	Value	Description
L	m	10^{-6}	Reference length
τ	s	0.01	Reference time
c_{ref}	mol/m^3	25,000	Reference concentration
M	kg	0.001	Reference mass
T_{ref}	K	298.0	Reference temperature
ϕ_{ref}	V	1.0	Reference potential

Table 3.2: Reference dimensions.

(a) Initial uniform concentration, $c = 0.1c_{ref}$

(b) $t = 0.33$ hr

(c) $t = 0.66$ hr

(d) $t = 1.0$ hr
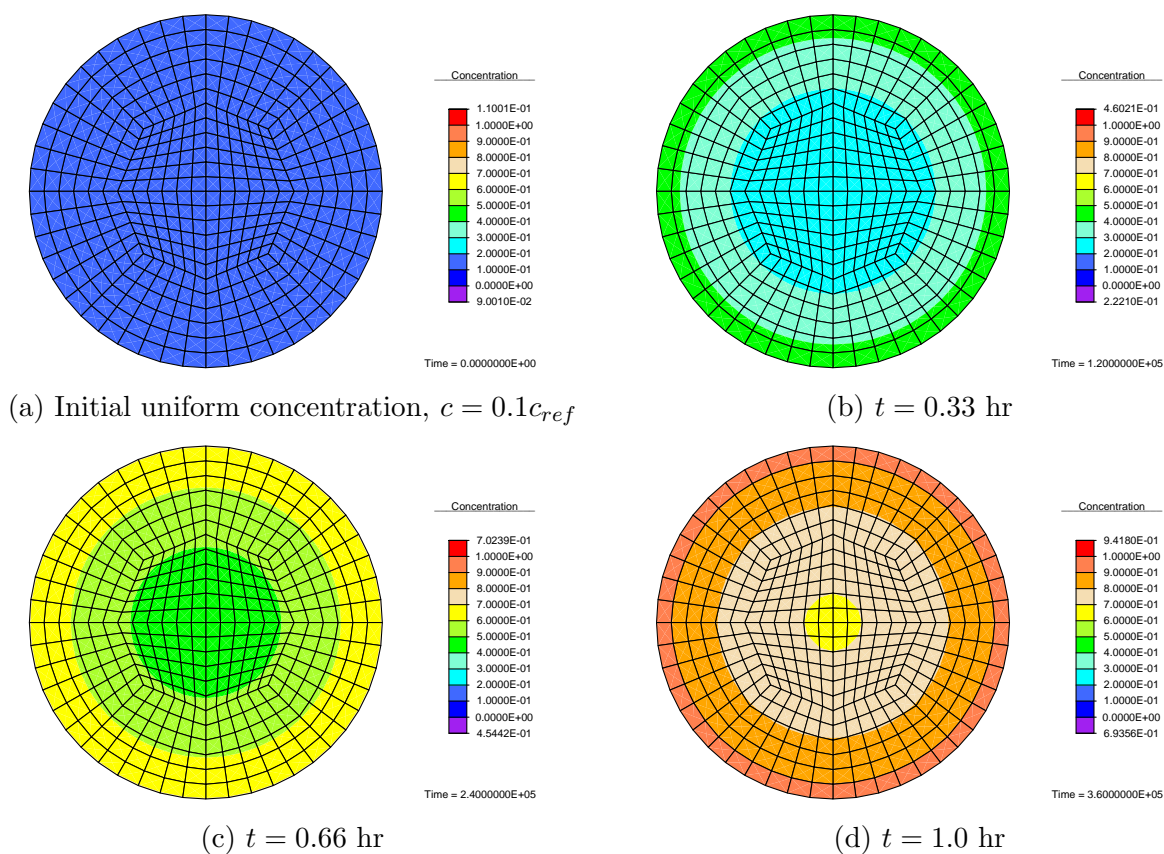
Figure 3.3: Non-dimensional concentration c/c_{ref} as time progresses. As expected, the concentration accumulates most near the edge where the ionic flux $\mathbf{j} \cdot \mathbf{n}$ is applied.
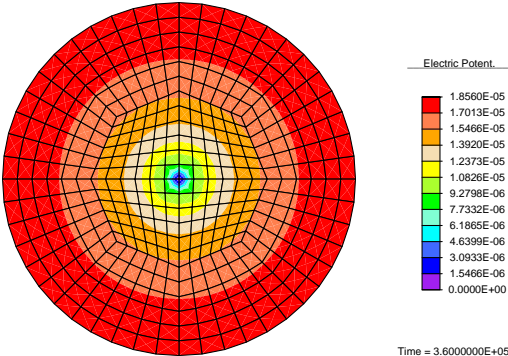
Figure 3.4: Non-dimensional potential distribution ϕ/ϕ_{ref} and the end of the simulation. For a uniformly applied surface current, the potential field is symmetrically linear and qualitatively satisfies Ampere's law for the given loading.

(a) X-displacement
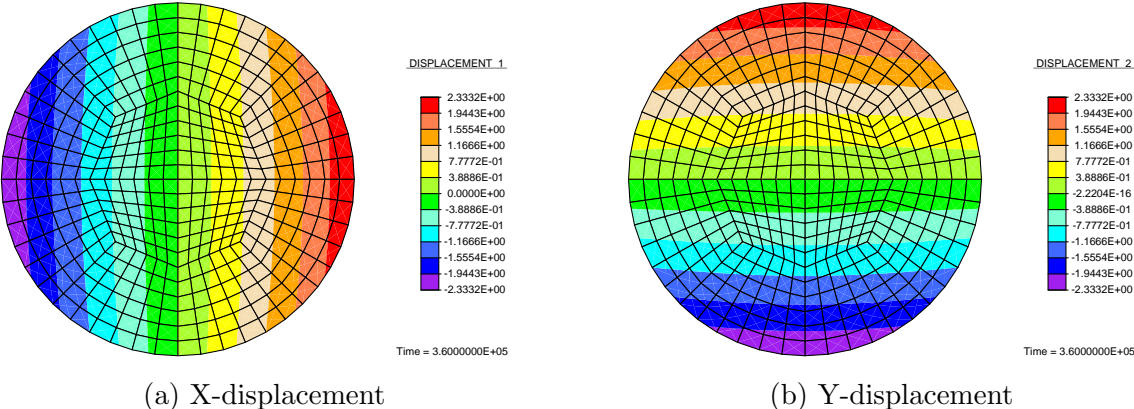
(b) Y-displacement

Figure 3.5: Non-dimensional displacement profile $\mathbf{u}/L$ and the end of the simulation. For a reference length of 10^{-6} m, the figure displays approximately a 2.33 μm displacement or 5% strain.

(a) Initial temperature

(b) Final temperature
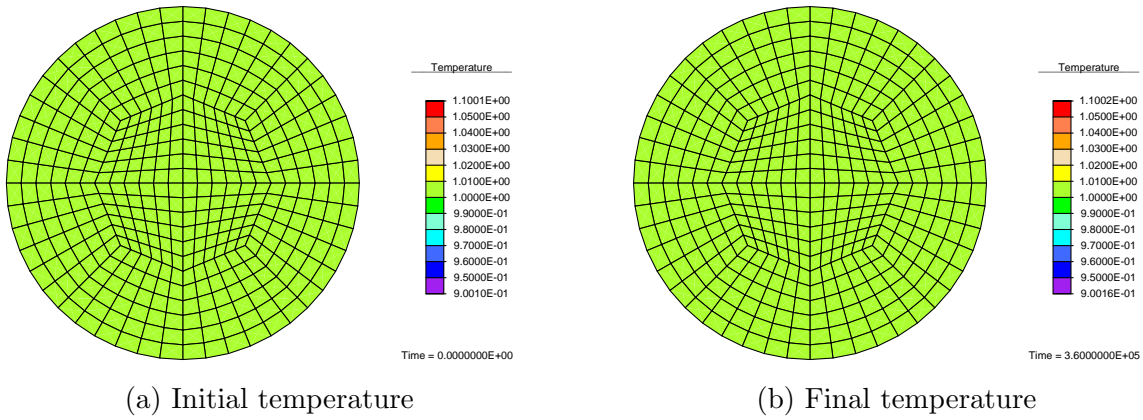
Figure 3.6: The non-dimensional temperature field T/T_{ref} remains essentially the same from time $t = 0$ to $t = 3600\,\text{s}$.

3.4 Test Case Simulation: Electrolyte User Element

Using the same geometry and similar boundary conditions of the previous case, we seek to test the physics of the electrolyte element. Due to the similarity between the constitutive relations of the electrolyte and active particle, we expect very similar results. Some material parameters were taken from Shi et al. (2011) while others were adjusted to mimic realistic physical properties. All user element material parameters are given in Table 3.3 with reference dimensions given in Table 3.2. The elastic modulus and Poisson ratio values were chosen to imitate a nearly incompressible fluid. We also wish to study how the temperature field changes with an applied surface thermal flux and two mechanical point forces. We've chosen a more in depth analysis for the electrolyte element since the constitutive relations are slightly more complicated. Now all four fields $\{\mathbf{u}, c, \phi, T\}$ should be changing with time.

At the outer $y = 50\,\mu\text{m}$ edge where $x = 0$, we apply compressive normal forces of 15 N. Figure 3.7 shows the previous section's mesh with newly applied loading. We reduce the applied $\mathbf{i} \cdot \mathbf{n}$ and $\mathbf{j} \cdot \mathbf{n}$ to $5\,\text{A/m}^2$ and $5.1822 \times 10^{-5}\text{mol/m}^2\text{s}$, respectively, along $\sqrt{x^2 + y^2} = R$. Lastly, there is an applied heat flux at the outer edge of $0.5\,\text{J/m}^2\text{s}$. In this test case, we use an initial concentration of $c = 1000\,\text{mol/m}^3\,(0.04c_{ref})$ and an initial temperature of $T_0 = 298.0\,\text{K}\,(1.0T_{ref})$.

Parameter	Unit	Value	Description
E	N/m^2	1.0×10^9	Young's Modulus
ν	-	0.49	Poisson ratio
ρ	kg/m^3	1.21×10^3	Density
Ω	m^3/mol	1.0×10^{-6}	Lithium swelling coefficient
α	1/K	12.46×10^{-6}	Thermal expansion coefficient
T_0	K	298.0	Initial Temperature
C$_P$	J/kg·K	1.8×10^3	Specific heat
λ	W/m·K	0.099	Thermal conductivity
D_+^{eff}	m^2/s	3.23×10^{-10}	Diffusion coefficient
κ_{eff}	S/m	1.0	Electrical conductivity
t_0	-	0.33	Transference number
$\partial \ln \gamma_{\pm} / \partial \ln c$	-	0.33	Thermodynamic factor

Table 3.3: Material parameters for an electrolyte user element. Some properties were taken from Shi et al. (2011) to model polypropylene.
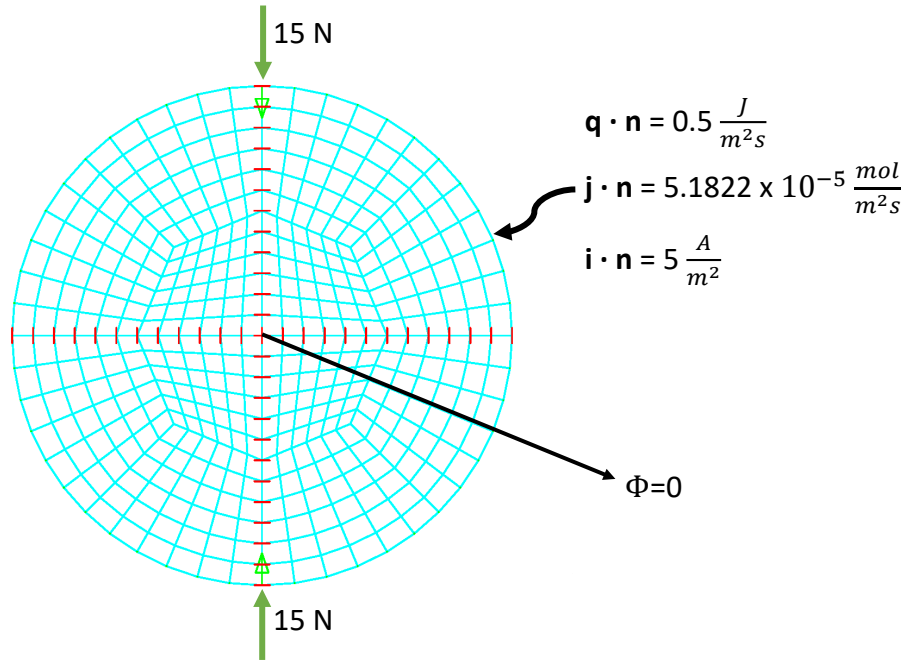
Figure 3.7: FEM mesh is shown in light blue with 432 4-node bilinear quadrilateral elements (all electrolyte user elements). The solution is assumed to be two dimensional with plane strain elasticity conditions. The mechanical boundary constraints are shown in red with the applied load of 15 N in green.

Again we carried out the solution for a simulation time of 1 hour and saw more interesting results compared to the case above. At the instant when the applied 15 N forces are applied, there are initially large displacements going in the direction of the load at the top and bottom edges. This is shown in Figure 3.9 with an initial outward expansion shown in Figure 3.8 due to the Poisson ratio effect. As lithium concentration and temperature increase in time, isotropic swelling occurs and eventually outweighs the displacement due to the mechanical points forces. The initial negative y displacement (u_y/L in the figure) changes to a positive value after 1 hour of running the simulation. If we choose to run the model for a much longer time, the volumetric expansion due to lithium intercalation and temperature changes completely outweighs the concentrated loads and the displacement fields are qualitatively the same as the test case in the previous section. In a realistic scenario, this continued expansion causes further stresses on adjacent active particles and the battery cell structure.

Because of the high diffusion coefficient D of the electrolyte material and symmetric loading, the concentration in Figure 3.10 remains essentially uniform at each instant in time. Changing the plotting range yields a slight spatial variance, but compared to the active particle concentration gradient this variation is negligible. The same occurs in Figure 3.12 for the temperature field as the thermal conductivity of the particle instantaneously spreads

the applied heat from the outer surface to the center of the particle. We quickly studied how the temperature varies without the applied heat flux. We saw that without the applied loading the temperature remains at T_0 even with Ohmic heating acting as a source term similar to the active particle simulation above. Even though the magnitude of the applied heating is theoretical, it was used to qualitatively simulate the exothermic reaction produced by intercalation kinetics at the active particle and electrolyte interface.

The potential plot in Figure 3.11 does not depict this phenomena well, but the instantaneous potential field shown was essentially linear. The electrolyte element responds well to the initial assumptions on its behavior for small concentration gradients and temperature changes. It is interesting to see that the magnitude of the potential field actually decreases with time. Recalling the constitutive relation for the electric current,

$$\mathbf{i} = -\kappa_{eff}\nabla\phi + \nabla\ln c \frac{RT\kappa_{eff}}{F}\left(2(1-t_+)\left[1 + \frac{\partial\ln\gamma_\pm}{\partial\ln c}\right]\right) ,$$

as the temperature and concentration gradient increase, the potential gradient must decrease to satisfy the constant current entering the electrolyte. Therefore, the potential distribution is not exactly linear in this case, which is expected. Also note that the value of the outer potential is an order of magnitude higher than the potential in the active particle case and the applied electric current is half that of the previous case. Further analysis of combined active particle and electrolyte elements in conjunction with the Butler-Volmer interface elements will be presented in subsequent sections.
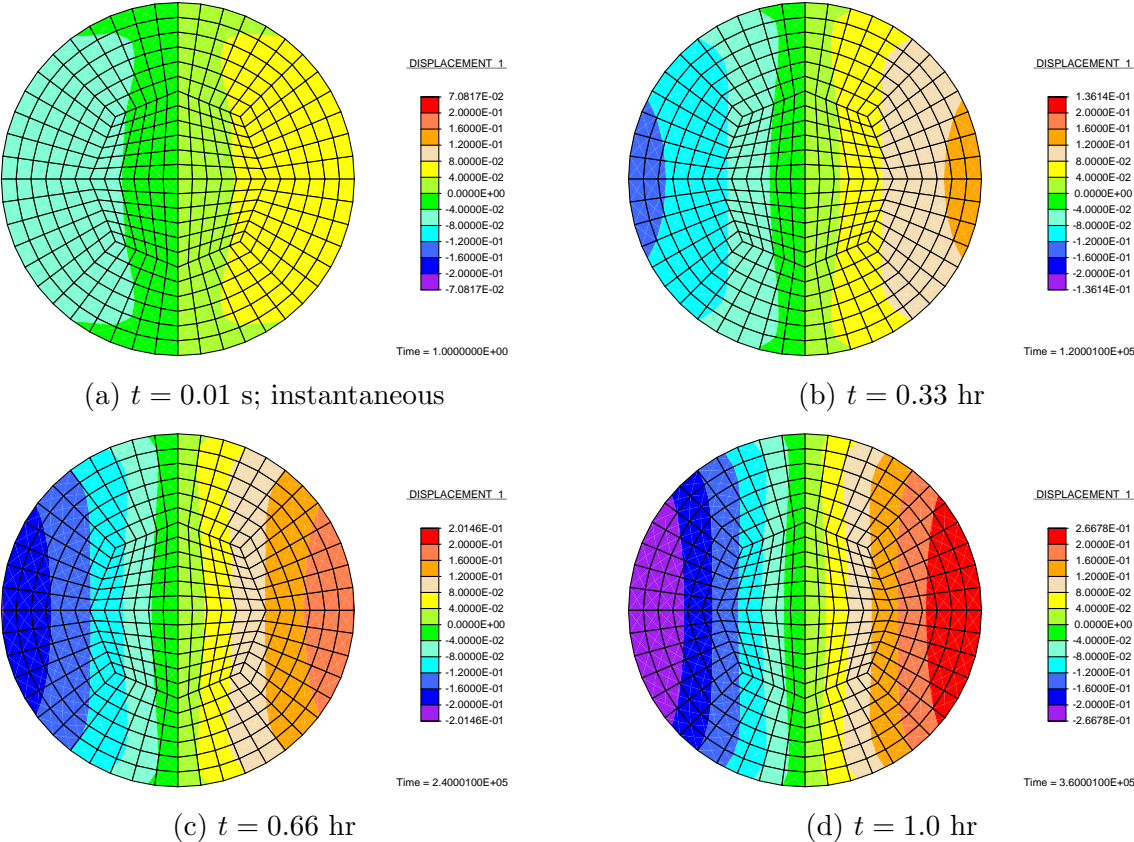
Figure 3.8: Non-dimensional x displacement u_x/L. One can see from (a) that there is greater expansion at the top and bottom of the mesh due to the concentrated load. As time progresses, the isotropic swelling due to the concentration and temperature fields cause the entire particle to expand and the Poisson effect of the load becomes less prominent.

(a) $t = 0.01$ s; instantaneous

(b) $t = 0.33$ hr

(c) $t = 0.66$ hr

(d) $t = 1.0$ hr
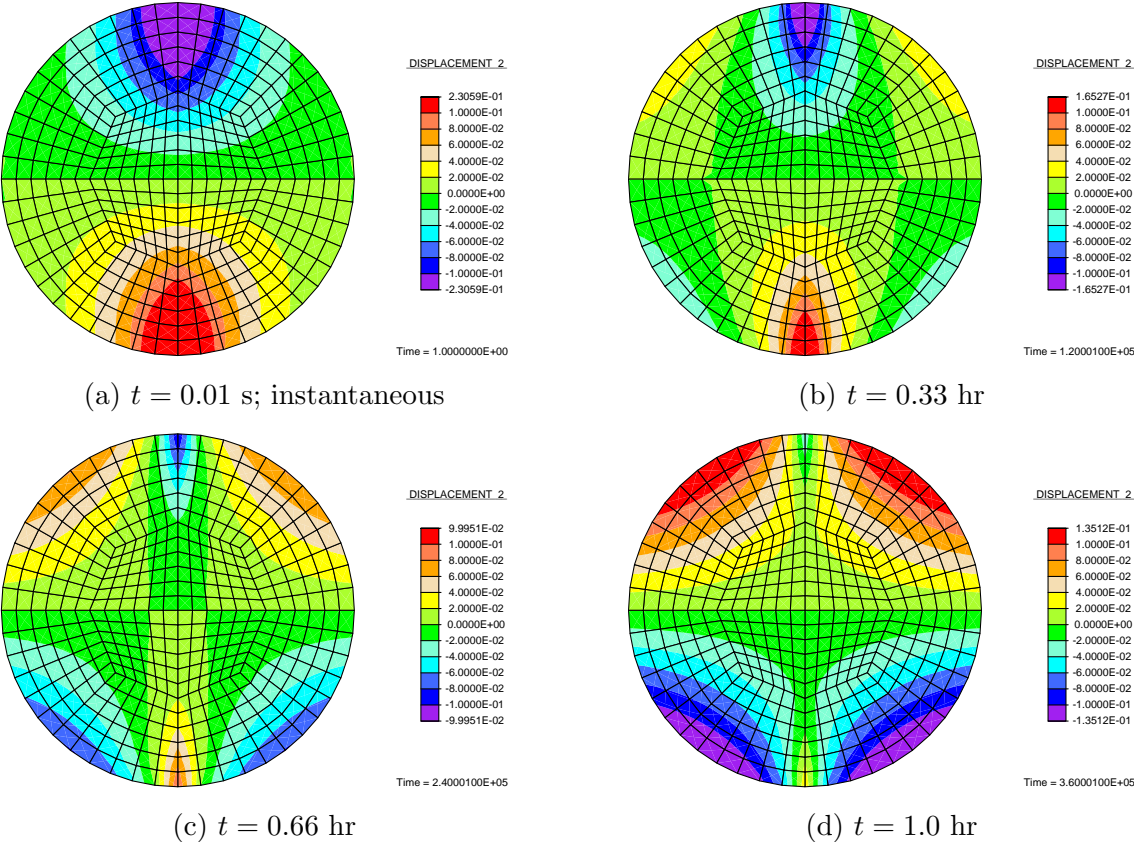
Figure 3.9: Non-dimensional y displacement u_y/L. The concentrated load causes an initial large negative displacement in (a). The resulting Poisson effect is shown in Figure 3.8. Due to the uniformly increasing ion concentration and temperature fields, the particle outwardly expands in all directions. As the simulation continues to run, we see in (d) the beginning of a positive displacement at the top and bottom surface.

(a) Initial concentration, $c = 0.04\,c_{ref}$

(b) $t = 0.33$ hr

(c) $t = 0.66$ hr

(d) $t = 1.0$ hr
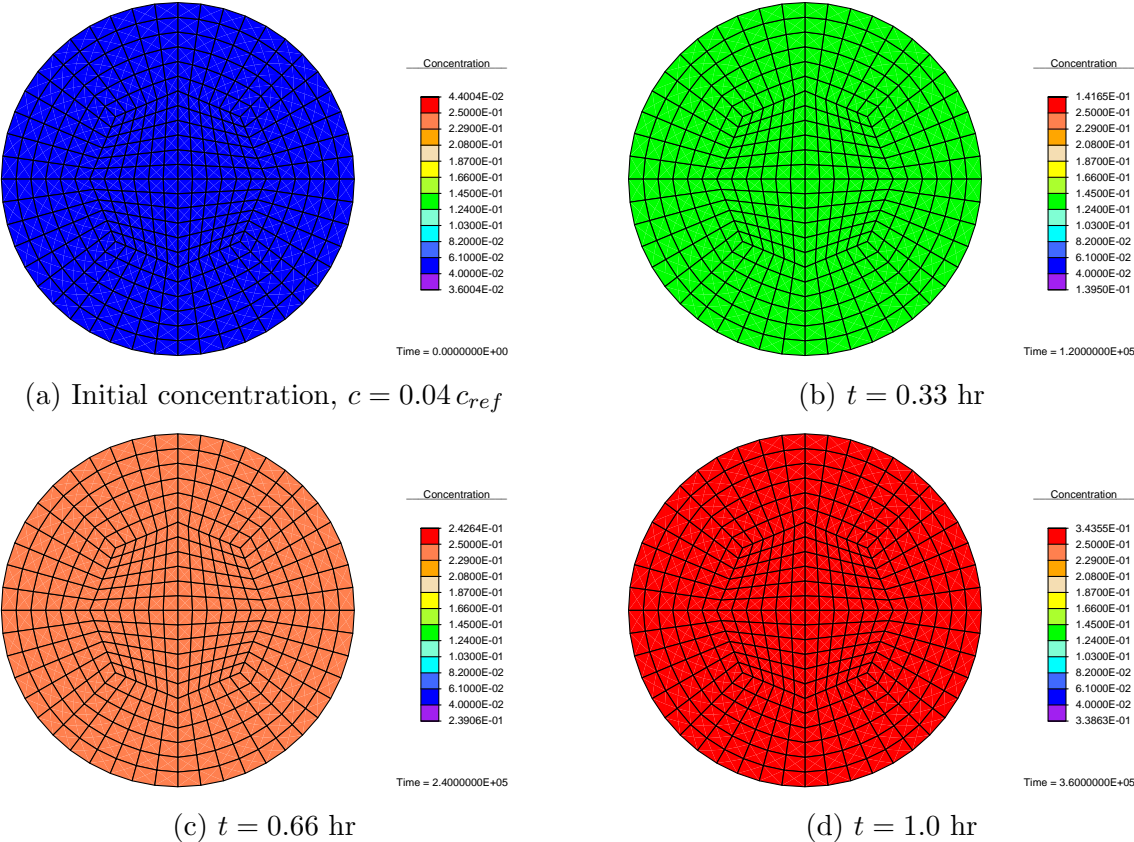
Figure 3.10: Non-dimensional concentration c/c_{ref}.

(a) Instantaneous potential, $t = 0.01\,\mathrm{s}$

(b) $t = 0.33$ hr

(c) $t = 0.66$ hr

(d) $t = 1.0$ hr
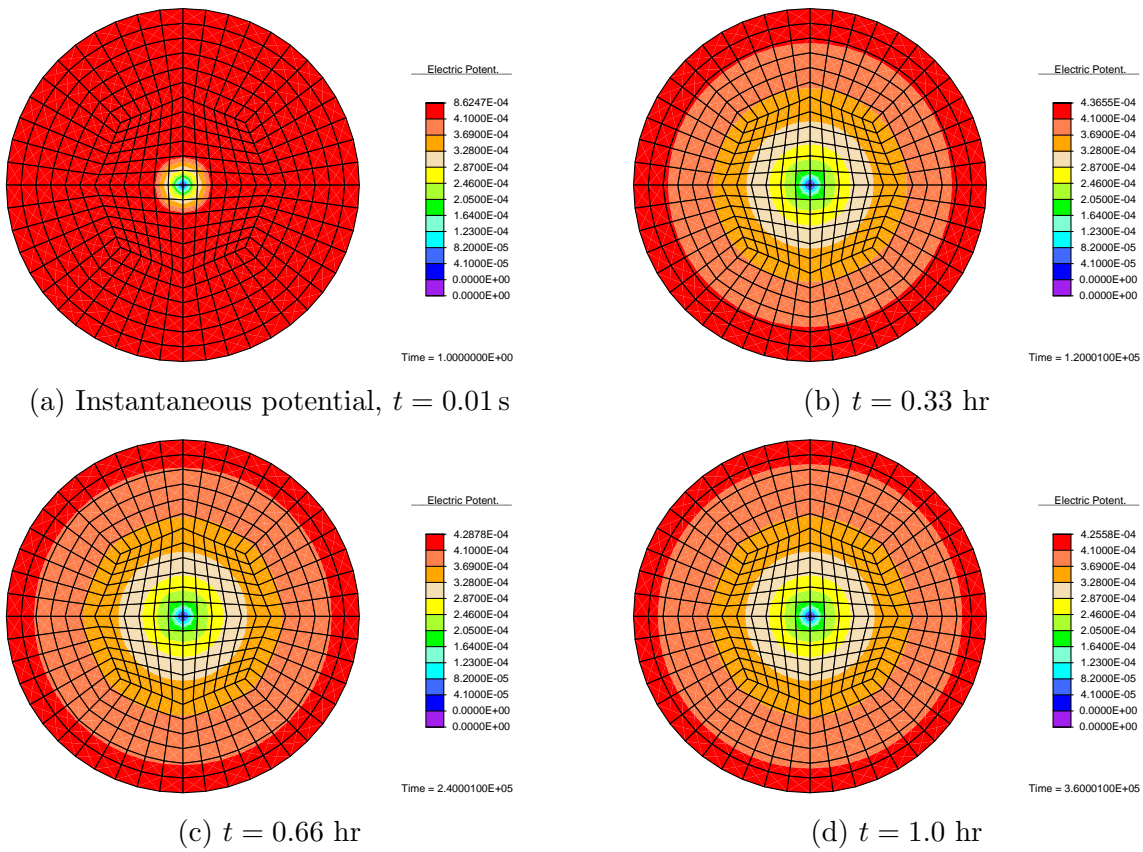
Figure 3.11: Non-dimensional potential ϕ/ϕ_{ref}. At $t = 0.01\,\mathrm{s}$, the potential reaches its greatest magnitude. As the simulation ran, the potential magnitude decreased to counteract the increasing concentration gradient and temperature.

(a) Instantaneous potential

(b) 0.33 hr

(c) 0.66 hr

(d) 1.0 hr
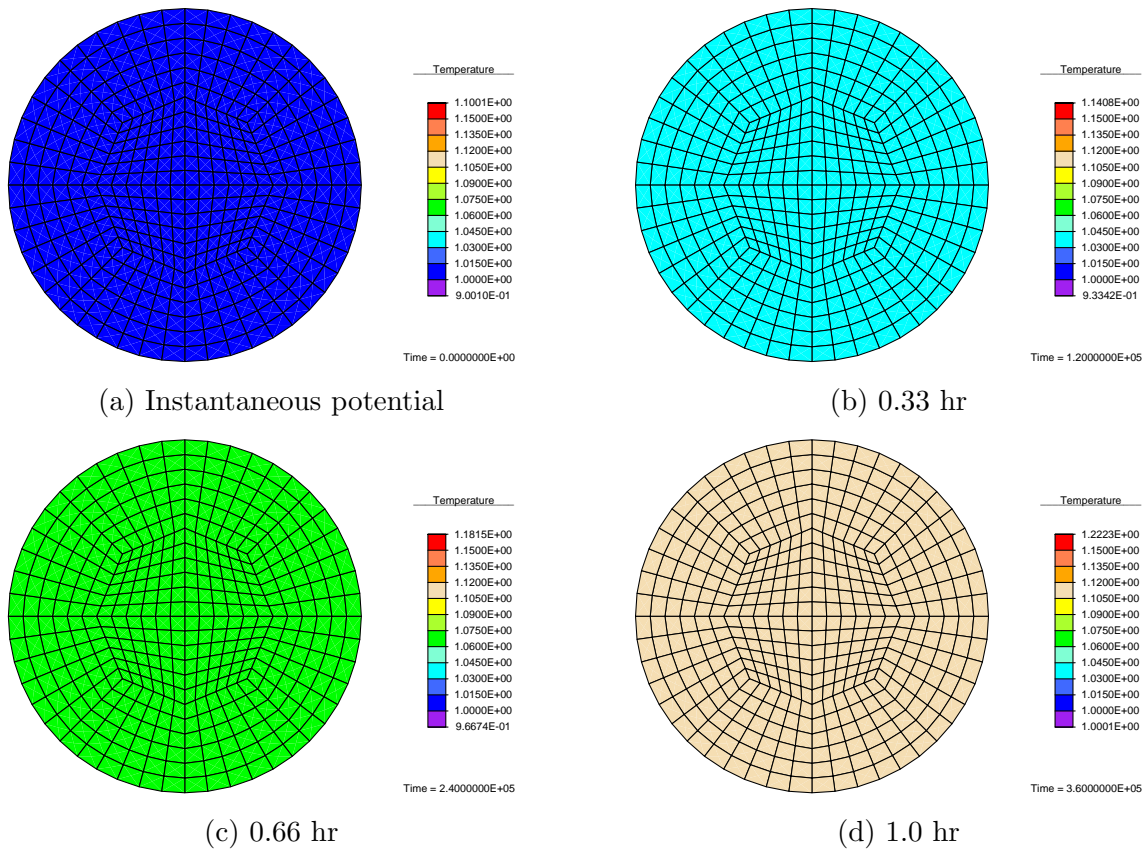
Figure 3.12: Non-dimensional temperature T/T_{ref} is homogeneous throughout the mesh.

3.5   Test Case Simulation: Porous Electrode

In this section we wish to study and simulate the discharge process of a typical lithium ion battery cell. Due to the high computational expense of our detailed micro scale model, we are only considering a thin two dimensional slice of a full cell and will output capacity densities per unit area of the cell. The simulation will again utilize plane strain elasticity. The cell will consist of a graphite anode, a lithium nickel manganese cobalt oxide (NMC) cathode, and lithium hexafluorophophase (LiPF$_6$) dissolved in an ethylene carbonate (EC) to ethyl methyl carbonate (EMC) electrolyte. We assume this specific compound for the electrolyte as it is very commonly reported in the literature. The diffusion and conductivity of lithium ions in the electrolyte are the most important properties compared to other electrolyte material parameters. In general, all the parameters used in the model below are functions of lithium concentration and temperature, but we assume constant values in our model. It is quite cumbersome to experimentally determine electrochemical properties. These properties vary by orders of magnitude in the literature, so one can only gauge a qualitative answer from

computer simulations and provide appropriate data fits thereafter. Even though our model is very detailed and includes all the necessary physics, we can only approximate its outputs due to variance in its inputs. This will be discussed in a later chapter on sensitivity analysis. All material properties used for the finite element analysis are given in Tables 3.6 and 3.7.

For this test case, we assume circular active particles in the electrode with surrounding electrolyte and a thin separator dividing the anode and cathode. Circular particles, commonly modeled as spheres in three dimensions, mimic the assumptions in porous electrode theory and many other finite element simulations in the literature. In Figure 3.13, the anode active particles are depicted in red, the cathode in light blue, the separator in dark blue, the electrolyte in the anode in green, and the electrolyte in the cathode in yellow. The full length L of the assumed cell is 145 micrometers with the anode L_A and cathode L_C individual lengths being 65 micrometers. As we are only considering a small subset of a full two dimensional cell layout, we choose the width $W = 26\,\mu$m and particle diameter $D_p = 20\,\mu$m.

At the left end of the anode $x = 0$, the potential is grounded and set to zero, $\phi_S = 0$. At the right end of the cathode $x = L$, we apply the discharge current of $1.49\,\text{A/m}^2$ for 19 hours, which is approximately a C/19 rate.[1] We fix the x and y displacements at the edges $x = 0$ and $x = L$. This resembles a battery cell casing providing enough mechanical stiffness to prevent swelling. Often this is not the case but this boundary condition will suffice for the chosen active particle materials. Additionally, we apply convective boundary conditions for the thermal flux at $x = 0$ and $x = L$,

$$\mathbf{q} \cdot \mathbf{n} = h_{conv}\left(T(t) - T_{amb}\right)\ ,$$

with h_{conv} being the heat transfer coefficient chosen to be $25.0\,\text{W/m}^2\text{K}$ and T_{amb} is the ambient temperature equal to 298 K. Since we are only considering a section of a full battery, at the $y = 0$ and $y = W$ axes there are no imposed Dirichlet or Neumann boundary conditions. We note that the proper treatment of the temperature degree of freedom should be to impose periodic convective boundary conditions along these axes but that requires knowledge of the solution a priori. Unless otherwise specified, all the results are given in their corresponding non-dimensional units with reference factors shown in Table 3.5.

---

[1]A C rate is a charge/discharge current applied relative to the battery's full capacity. A 1C discharge will completely discharge the battery in 1 hour. While a C/10 rate will discharge the cell in 10 hours, etc.
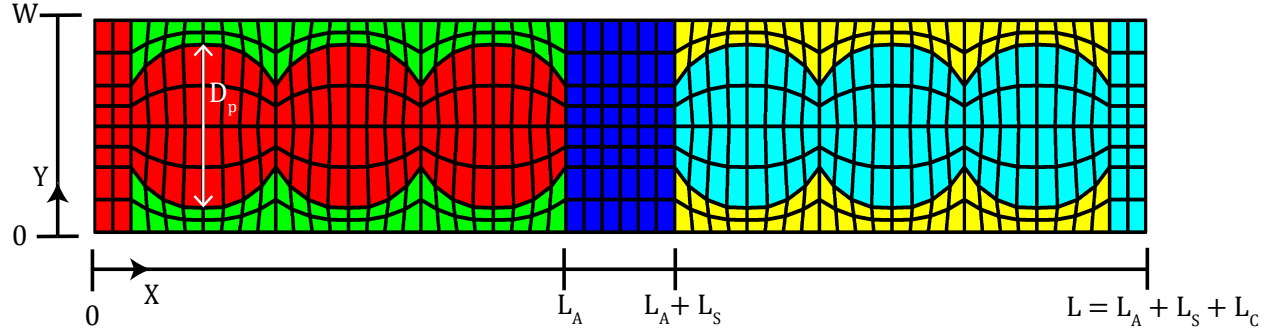
Figure 3.13: The finite element mesh consists of active particles for the anode and cathode shown in red and light blue, respectively. The dark blue elements represent the electrolyte separator. The green and yellow elements depict the liquid electrolyte surrounding the particles. For simplicity, we assume the same material parameters for all electrolyte elements (green, dark blue, yellow).

$x = 0$	$x = L$	$y = 0$	$y = W$
$\mathbf{u} = 0$	$\mathbf{u} = 0$	$\boldsymbol{\sigma} \cdot \mathbf{n} = 0$	$\boldsymbol{\sigma} \cdot \mathbf{n} = 0$
$\mathbf{j} \cdot \mathbf{n} = 0$	$\mathbf{j} \cdot \mathbf{n} = 0$	$\mathbf{j} \cdot \mathbf{n} = 0$	$\mathbf{j} \cdot \mathbf{n} = 0$
$\phi = 0$	$\mathbf{i} \cdot \mathbf{n} = \hat{i}_{discharge}$	$\mathbf{i} \cdot \mathbf{n} = 0$	$\mathbf{i} \cdot \mathbf{n} = 0$
$\mathbf{q} \cdot \mathbf{n} = h_{conv}\left(T(t) - T_{amb}\right)$	$\mathbf{q} \cdot \mathbf{n} = h_{conv}\left(T(t) - T_{amb}\right)$	$\mathbf{q} \cdot \mathbf{n} = 0$	$\mathbf{q} \cdot \mathbf{n} = 0$

Table 3.4: Boundary conditions.

Parameter	Unit	Value	Description
L	m	10^{-6}	Reference length
τ	s	0.01	Reference time
c_{ref}	mol/m^3	25,000	Reference concentration
M	kg	0.01	Reference mass
T_{ref}	K	298.0	Reference temperature
ϕ_{ref}	V	1.0	Reference potential

Table 3.5: Reference dimensions.

We ran the simulation until the cell potential approximately reached 2.8 V. From the FEM model we are able to see a detailed analysis of the deformation, concentration, and potential

profiles that occur within a battery cell. During the discharge process, lithium ions in the active particles flow from the anode to cathode resulting in either expansion or contraction of the appropriate electrode. The electrolyte is assumed to be semi-incompressible and surrounds the particles, following their motion. Since the relative swelling coefficents of the anode and cathode differ, the anode undergoes larger contraction than the cathode's expansion. Figure 3.14 shows the cell's full displacement profile along with the deformed shape of the battery with a 10x magnification multiplier. Figure 3.15 shows a detailed illustration of the stress states $\sigma_{xx}, \sigma_{yy}, \sigma_{zz}$, and σ_{xy}. Since the deformation is primarily due to lithium swelling, the deformation and stress distribution of the particles is very symmetrical. Due to the mechanical constraints, the highest stress occurs at the boundaries $x = 0$ and $x = L$. The corners exhibit the highest stress concentrations as expected. The magnitude of these values indicates that the electrode might be subjected to yielding. We will not make any predictions, as we are more concerned with the relative stress distribution within the cell and qualitative information. We know that this particular FEM mesh is not an extremely accurate representation of the microstructure, so we are not justified in making accurate quantitative predictions.
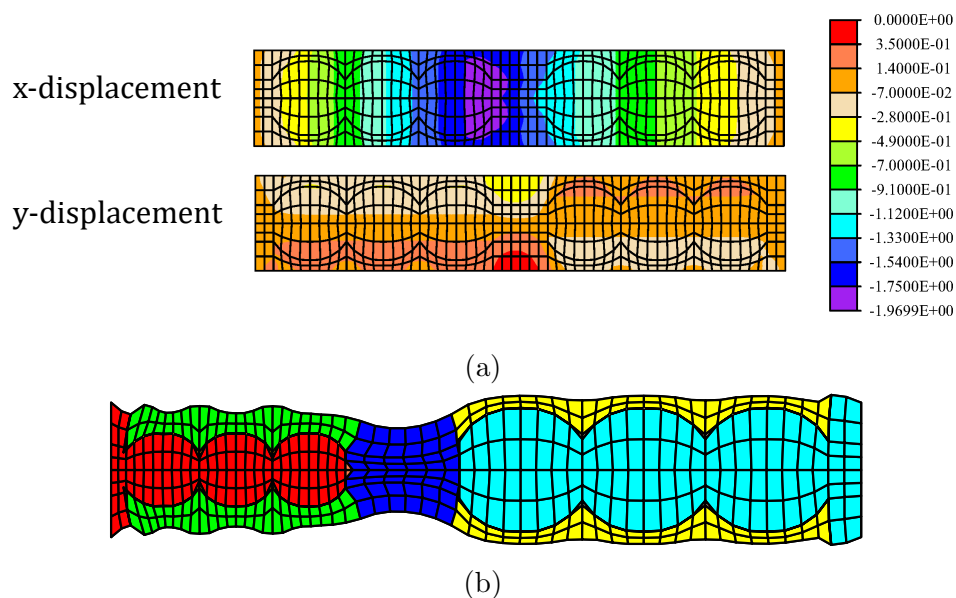
Figure 3.14: The final discharge x and y displacements are portrayed in (a). The units for the colorbar are also non-dimensional. Multiplying by the reference length $L = 10^{-6}$ would yield units of meters. It is clear that the anode particles exhibit higher deformations compared to the cathode particles due to the greater swelling coefficient. The deformed configuration (10x multiplier) in (b) gives a qualitative description of the full cell's deformation.
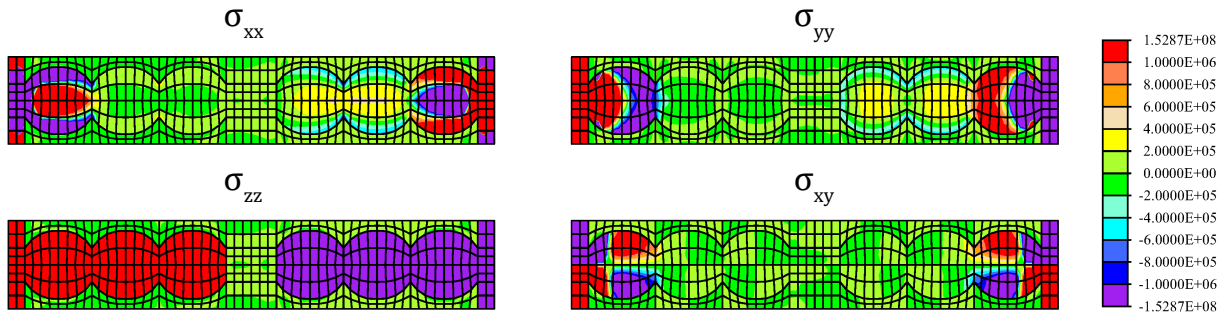
Figure 3.15: Stress distribution measured in Pascals at the end of discharge.

Without the electrolyte filling the pores of both electrodes, it would take lithium ions much longer to travel from anode to cathode, or vice versa. This would result in poorer discharge performance. The diffusivity D of lithium in electrolyte materials is much higher than that of the active particle materials and allows the concentration to remain essentially uniform throughout the entire discharge process. Beginning with an initial concentration of 23750 mol/m^3 $(0.95\,c_{ref})$ in the anode, 2250 mol/m^3 $(0.09\,c_{ref})$ in the cathode, and 1000 mol/m^3 $(0.04\,c_{ref})$ in the separator and electrolyte materials, we can see the concentration changes at various times in Figure 3.16. The magnitude of the ionic flux $|\mathbf{j}|$ is highest in the electrolyte as expected due to the lower electrical conductivity resulting in a greater potential gradient; see Figure 3.19. The electrolyte's larger ionic flux allows lithium to quickly move around the active particles and helps maintain a uniform spatial distribution of its initial concentration.

Figure 3.17 shows the concentration distribution in the anode and cathode at the end of discharge. It illustrates a slightly more uniform lihtium concentration in the anode than compared to the cathode. We attribute this outcome to either the higher anode diffusivity or due to the differences in the equilibrium open circuit potentials $U_0(\bar{c}, T)$ of the two materials. The transfer of lithium ions between different material elements is achieved through surface interface elements incorporating the Butler-Volmer reaction expressions. One can also see from Figure 3.19 that the magnitude of the ionic flux is highest at the surrounding electrolyte elements near the separator. This seems sensible due to the electrolyte's lower conductivity κ and a higher diffusion constant. Since the length of each electrode is relatively small and the discharge rate is relatively low, one does not see an accumulation of concentration at the surface of the electrode particles. This scenario would be ideal for realistic applications.
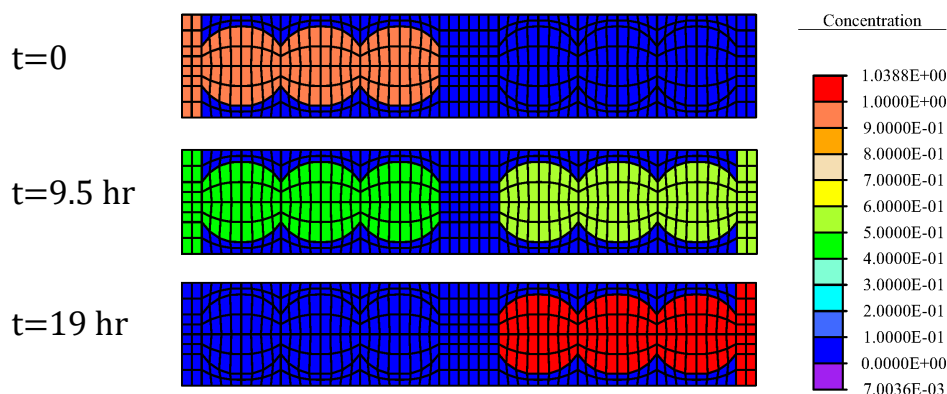
Figure 3.16: Full cell normalized concentration c/c_{ref} as time progresses.

(a) Anode   (b) Cathode
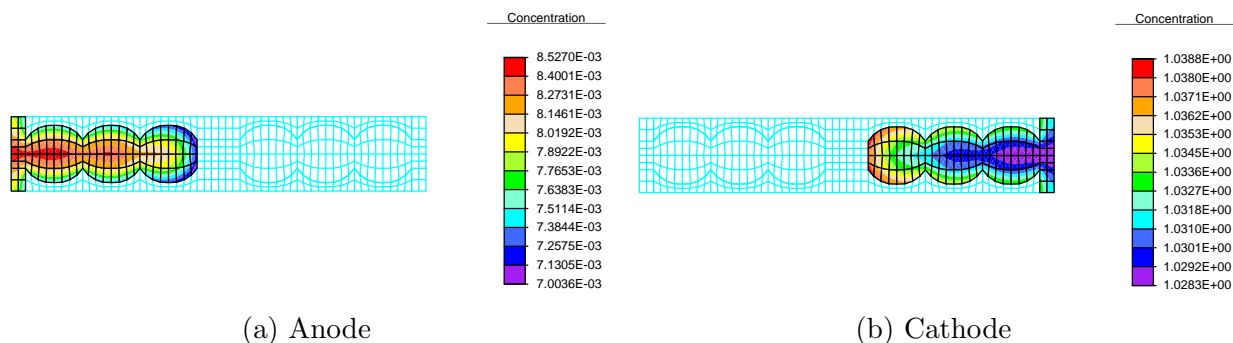
Figure 3.17: Anode and cathode normalized concentration c/c_{ref} after 19 hours of discharge.

Figure 3.18 shows the potential distribution within the cell at the end of the simulation run. The anode is grounded and reaches its maximum negative potential at the junction nearest the separator. Charge conservation yields that ϕ is almost uniform throughout the active particles due to the larger conductivity κ. The electrolyte potential distribution results in the largest potential gradient. It is continuous throughout the regions surrounding the active particles and is discontinuous at the interfaces with the particles.

(a) Anode

(b) Cathode

(c) Surrounding electrolyte and separator
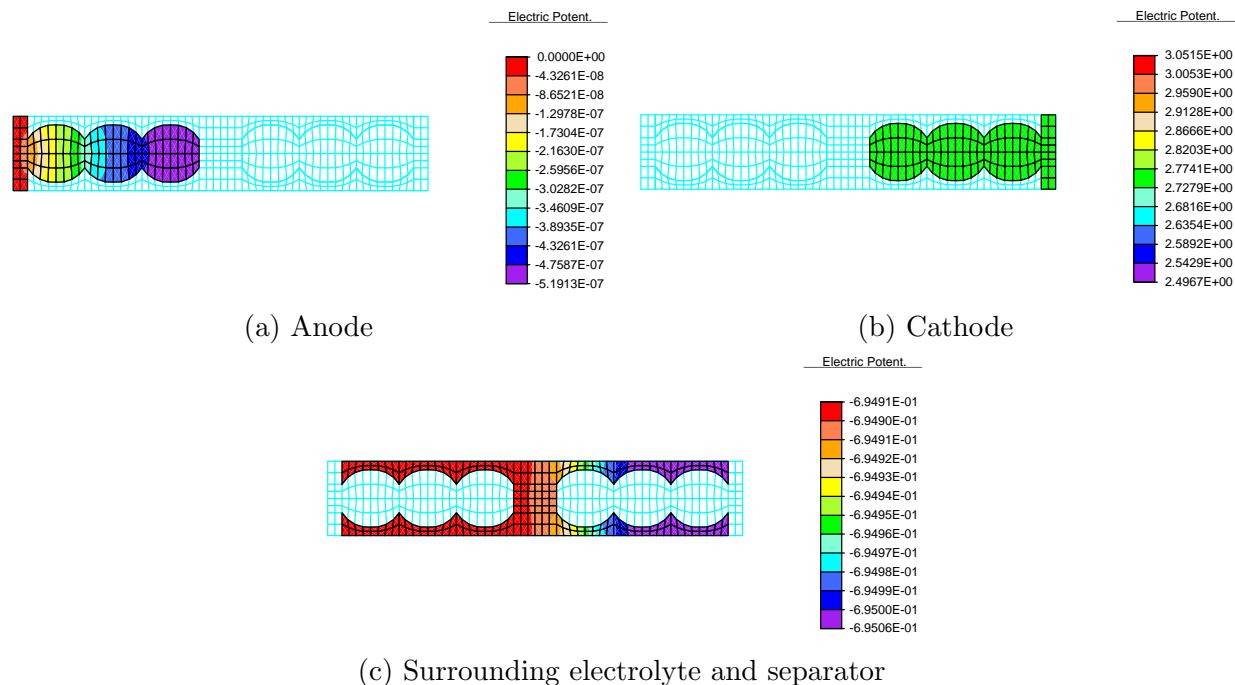
Figure 3.18: (a), (b), and (c) show the potential profiles ϕ/ϕ_{ref} with normalized units at the end of discharge, $t = 19\,\mathrm{hr}$.

Due to the low discharging rate, the temperature changes insignificantly. T evolves from 298 K to 298.3 K at the end of discharge. Towards the end of discharge, there is a variance of the thermal flux distribution throughout the cell but its magnitude is very negligible and produces no significant heating or cooling effect. We can attribute this to the small current rate applied, which allows heat to equilibriate to T_{amb} at the $x = 0$ and $x = L$ edges. However, increasing the discharge rate does result in a significant temperature drop. This is not shown here, but tells us that slower discharging protocols are best for maintaining a desired temperature. This is reassuring as the C/19 discharging rate we apply is very similar to standard charging/discharging rates traditionally used for experimentally testing of equilibrium electrochemical properties. Researchers use such a small magnitude to avoid high temporal temperature fluctuations and maintain chemical stability.

(a) Ionic flux $|\mathbf{j}|$ with units $[\mathrm{mol/m^2s}]$

(b) Electric current $|\mathbf{i}|$ with units $[\mathrm{A/m^2}]$

(c) Thermal Flux $|\mathbf{q}|$ with units $[\mathrm{W/m^2}]$
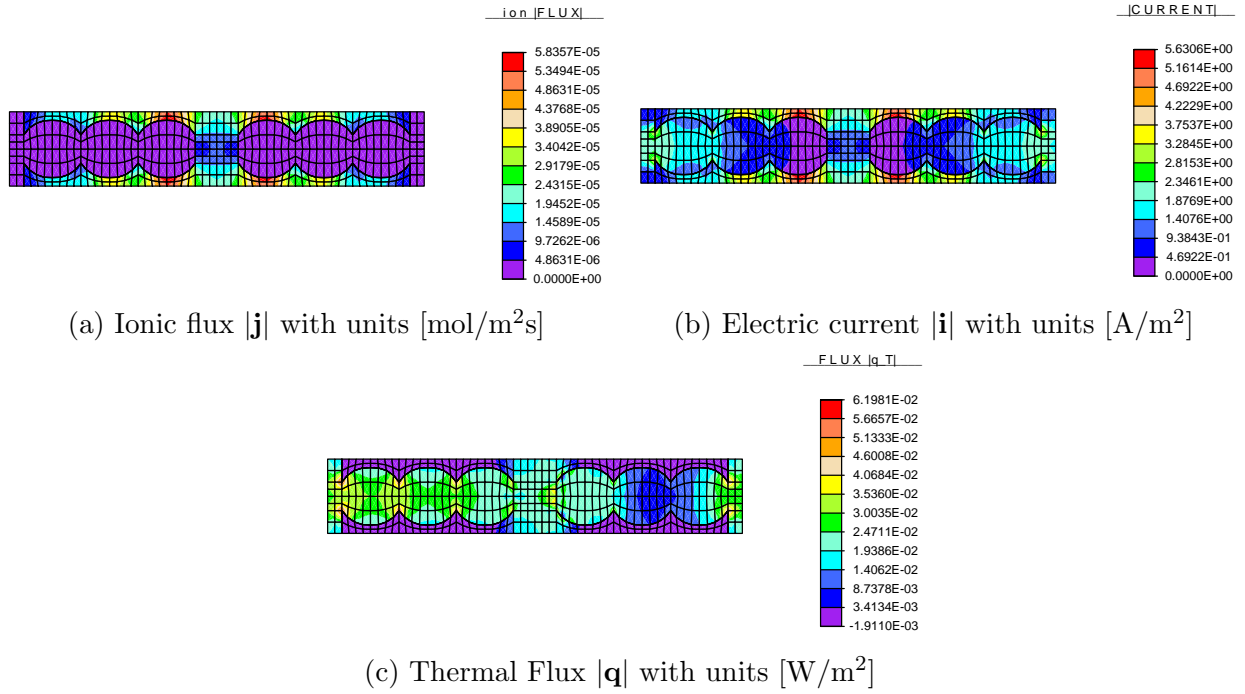
Figure 3.19: This figure illustrates the ionic, electric current, and thermal flux magnitudes at the end of discharge, $t = 19\,\mathrm{hr}$.

Once the cell reaches 2.8 V, the final capacity density of 2.31 mAh/cm^2 is reached. Battery capacity is the amount of electric work that can be extracted from a battery. Mathematically, it is expressed at the time integration of the electric current,

$$Q = \int_0^T I(t)\,dt\,, \tag{3.29}$$

where $I(t)$ [A] is the current extracted at the side of cathode current collector. Our simulation extracts the capacity density, as we are sampling values of the current density $|\mathbf{i}|$ with units [A/m^2] in the integrand in lieu of the total current I. A capacity density of the magnitude achieved above is typical for a NMC cell at a discharge of 1.5 A/m^2 (Jiao et al., 2018). If we choose to vary the discharge rate as in Figure 3.20, we can see the variance in potential and capacity for different loading rates. The final capacities are very similar except the initial potential is varied greatly. Further work will be to determine what model parameters have the greatest contribution in affecting the cell capacity density.

(a)

(b)
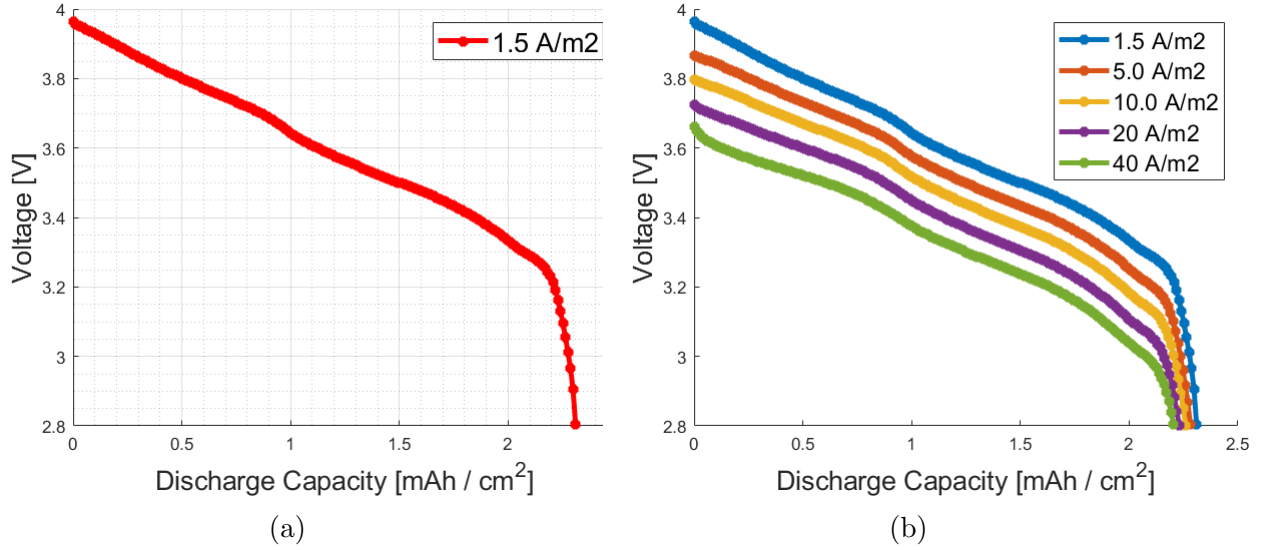
Figure 3.20: (a) shows the voltage vs. capacity profile for the current simulation's discharge rate. (b) shows the varying profiles for multiple discharge rates, whose further detailed analysis was not included in this test case section. Once the cell's voltage reached 2.8V, the simulation stopped.

Parameter	Unit	Anode	Electrolyte	Cathode	Description
E	N/m^2	5.93×10^9	3.0×10^5	8.88×10^9	Young's Modulus
ν	-	0.30	0.49	0.3	Poisson ratio
ρ	kg/m^3	2.5×10^3	1.1×10^3	2.5×10^3	Density
Ω	m^3/mol	2.88×10^{-6}	0	1.86×10^{-6}	Lithium swelling
α	1/K	6.0×10^{-6}	12.46×10^{-6}	9.615×10^{-6}	Thermal expansion
T_0	K	298.0	298.0	298.0	Initial Temperature
C$_P$	J/kg·K	7.0×10^2	1.0×10^3	7.0×10^2	Specific heat
λ	W/m·K	1.04	0.01	5.0	Thermal conductivity
D	m^2/s	5.0×10^{-13}	3.23×10^{-10}	1.0×10^{-13}	Diffusion coefficient
κ	S/m	1.5×10^2	1.0	0.1×10^2	Electrical conductivity
t_0	-	-	0.363	-	Transference number
$\partial \ln \gamma_{\pm} / \partial \ln c$	-	-	0.43	-	Thermodynamic factor

Table 3.6: Material parameters anode, cathode, and electrolyte elements. Note that even though the separator would have different material properties than the surrounding electrolyte, we have assumed the same parameters for both materials.

Parameter	Unit	Anode	Cathode	Description
k_R	$\mathrm{m}^{5/2}/\sqrt{\mathrm{mol}} \cdot \mathrm{s}$	$1.0 \cdot 10^{-11}$	$1.0 \cdot 10^{-11}$	Intercalation reaction rate
c_{max}	$\mathrm{mol/m}^3$	25000	30000	Maximum concentration

Table 3.7: Material parameters for Butler Volmer element for interface elements between active particle and electrolyte materials. Capacity fading mechanisms including SEI growth and lithium plating were not considered for this case.

The open circuit voltages used in the Butler-Volmer element are given by previous researchers (Wang et al., 2018). The anode's (negative electrode) OCV as a function of normalized concentration $\bar{c} = c/c_{max}$ at the surface is

$$
\begin{aligned}
U_0^N(\bar{c}) = {} & 0.266 + 0.555 \exp\left(-178.97\bar{c}\right) - 0.012 \tanh\left(\frac{\bar{c} - 0.557}{0.028}\right) \\
& - 0.0117 \tanh\left(\frac{\bar{c} - 0.239}{0.049}\right) - 0.0129 \tanh\left(\frac{\bar{c} - 0.175}{0.035}\right) \\
& - 0.05 \tanh\left(\frac{\bar{c} - 0.99}{0.0245}\right) - 0.035\bar{c} - 0.012 \tanh\left(\frac{\bar{c} - 0.13}{0.02}\right) \\
& - 0.152 \tanh\left(\frac{\bar{c} - 0.03}{0.023}\right) ,
\end{aligned}
\tag{3.30}
$$

and the cathode's (positive electrode) OCV is

$$
\begin{aligned}
U_0^P(\bar{c}) = {} & \bigg(-0.0923 - 7.82\bar{c} + 50.07\bar{c}^2 - 122.28\bar{c}^3 + 82.98\bar{c}^4 + 140.29\bar{c}^5 \\
& - 374.73\bar{c}^6 + 403.25\bar{c}^7 - 221.19\bar{c}^8 + 49.33\bar{c}^9 \bigg) \bigg/ \bigg(-0.02 - 1.9\bar{c} \\
& + 11.73\bar{c}^2 - 28.78\bar{c}^3 + 27.54\bar{c}^4 - 8.63\bar{c}^5 \bigg) .
\end{aligned}
\tag{3.31}
$$

Both potentials are measured in Volts [V] and are illustrated in Figure 3.21. The change in U_0 with respect to temperature T is given below (Wang, Siegel, and Garikipati, 2017). This

expression for $\partial U_0 / \partial T$ was used in both the anode and cathode interface elements.

$$
\frac{\partial U_0}{\partial T} =
\begin{cases}
0.01442 * \bar{c}^2 - 0.00291 * \bar{c} - 0.000138 & \bar{c} \leq 0.2 \\
0.00634 * \bar{c}^3 - 0.006625 * \bar{c}^2 + 0.002635 * \bar{c} - 0.0004554 & 0.2 < \bar{c} \leq 0.4 \\
0.001059 * \bar{c} - 0.0004793 & 0.4 < \bar{c} \leq 0.5 \\
0.00025 * \bar{c} - 7.5 \times 10^{-5} & 0.5 < \bar{c} \leq 0.7 \\
-0.001 * \bar{c} + 0.0008 & 0.7 < \bar{c} \leq 0.8 \\
0.0333 * \bar{c}^2 - 0.057 * barc + 0.02427 & 0.8 < \bar{c} \leq 0.82 \\
0.002 * \bar{c}^2 - 0.0038 * \bar{c} + 0.00177 & 0.82 < \bar{c} \leq 0.95 \\
-0.0014 * \bar{c} + 0.0012 & 0.95 < \bar{c} \leq 1
\end{cases}
\tag{3.32}
$$
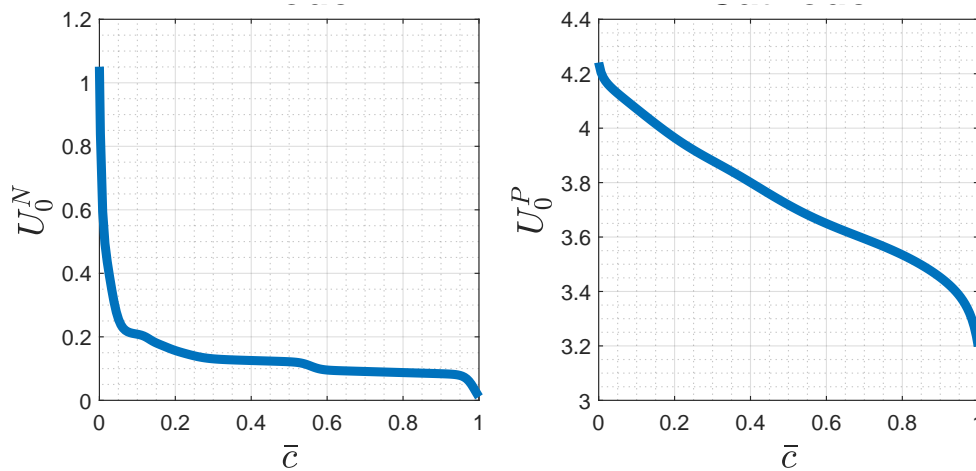
Figure 3.21: Open circuit voltages as a function of normalized concentration $\bar{c} = c_S/c_{max}$ where c_S is the active particle concentration evaluated at the surface of the electrolyte/electrode interface.
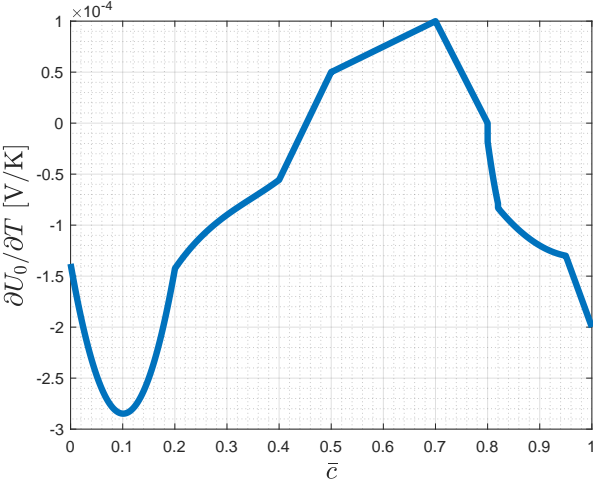
Figure 3.22: Change in open circuit voltage as a function of temperature.

Chapter 4

Electrochemical Methods for Determining Transport Properties in Electrodes

In this chapter, we will discuss some of the limitations of common experimental techniques in determining the diffusion coefficient of lithium in electrodes. The two methods we will investigate will be the Galvanostatic and Potentiostatic Intermittent Titration Techniques. They are commonly employed in commercial and research applications for calculating transport properties in electrodes. We find that even in an idealized simulation, there is uncertainty in the results we obtain due to reaction rates and the electrical conductivity of the electrolyte.

4.1 Experimental Overview

One of the most important properties in battery chemistry is the diffusion coefficient of lithium ions in the host matrix of the electrode. Experimental measurements of diffusion coefficients for simple materials can be carried out by radiotracer techniques. This experiment tracks an element isotope implanted into the host material. The isotope's nucleus is unstable and radioactive, which can then be detected by radiation detectors. This allows one to trace the mechanism of a chemical reaction or view the distribution of an element within a substance. For example, this method has previously been applied with lithium and flourine as the isotope tracers (Jeong et al., 2003).

Accurate measurement of the diffusivity and other primary electrochemical properties is imperative for accurate numerical simulations of any battery cell. A researcher cannot appropriately analyze the results with inconsistent simulation inputs. Most material properties are commonly derived by experimental testing, while a few are derived from first principles calculations. In particular, a few common methods to experimentally determine the diffusivity include the Galvanostatic Intermittent Titration Technique (GITT) and the Potentiostatic Intermittent Titration Technique (PITT) experiments. These methods in-

volve the application of an incremental potential or current, respectively, resulting in an incremental change of the lithium concentration due to chemical reactions occurring at the electrode-electrolyte interface. Analytical expressions are available to determine the diffusion coefficient of a chemical species in a host electrode. These expressions are calculated through transient changes in lithium concentration, electric potential, and electric current. The analytic expressions are solutions to a partial differential equation resulting from the mass conservation governing equation. Additionally, one is able to measure other pertinent electrochemical properties through these techniques.

The seminal GITT experiment of Weppner and Huggins (1977) introduced a novel technique to calculate many important battery cell properties. These properties included the chemical and component diffusion coefficients, electrical conductivity, ion mobility, the thermodynamic enhancement factor, and even the reaction rate constant. The species diffusivity in the host electrode matrix is determined by applying small current pulses to change the equilibrium state of the electrode's voltage and hence the name Galvanostatic Intermittent Titration Technique. The current pulses result in small incremental changes in the cell potential that are then measured and used to determine desired electrochemical properties.

The GITT experiment surpassed the PITT experiment in Wen, Boukamp, and Huggins (1979) as it proved to be more accurate. The PITT method is slightly older wherein incremental potential changes are applied instead of current pulses. The transient current response is then measured to determine the same electrode properties. In both cases, a battery half cell setup is only needed, in which lithium metal is typically the reference electrode at the negative terminal. Fick's law is used to describe the ionic flux in both cases and the mass conservation PDE is solved for the species concentration given appropriate flux boundary conditions at the electrode-electrolyte interface.

4.2 Galvanostatic Intermittent Titration Technique

The GITT procedure is concisely described by the Metrohm Autolab manuscript in Autolab (2014a). Short current pulses are applied to the half cell which slowly increases (or decreases during negative pulses) the cell potential. This results in a flux of lithium ions entering the electrode at any contact points with the electrolyte solution and a subsequent change in chemical stoichiometry. The pulse is followed by a zero current relaxation time allowing for lithium ions near the surface of the interface to diffuse through the solid media ensuring homogeneous lithium concentration after a certain period of time. The solution to the mass conservation equation yields the diffusion coefficient D through the following formula,

$$\frac{dc}{d\sqrt{t}} = \frac{2I}{Sz_A F\sqrt{D\pi}}, \tag{4.1}$$

where I is the applied current pulse [A], z_A is the valency, S is the contact area between electrolyte-electrode [m^2], and the concentration c [mol/m^3] of lithium in the host electrode

is sampled at this interface. This equation is valid for time $t << L^2/D$, where L is the characteristic length of the electrode. One can manipulate this equation to obtain the diffusion coefficient in terms of the time dependent potential E [V]. Equation (4.1) then becomes

$$D = \frac{4}{\pi} \left(\frac{IV_m}{z_A FS} \right)^2 \left(\frac{dE}{d\delta} \bigg/ \frac{dE}{d\sqrt{t}} \right)^2 , \tag{4.2}$$

where V_m is the molar volume of the electrode [m^3/mol] and δ [-] is the stoichiometric ratio of lithium in the host material. One should note that the relation between δ and the concentration c is given by the relation $d\delta = V_m \, dc$. The numerator $dE/d\delta$ in the equation above is the slope of the coulometric titration curve, which is essentially the change in the open circuit potential of the electrode against the change in normalized lithium concentration. If sufficiently small currents and short pulse durations are used, we can approximate the derivatives by linear relations yielding

$$D = \frac{4}{\pi \tau} \left(\frac{n_m V_m}{S} \right)^2 \left(\frac{\Delta E_s}{\Delta E_t} \right)^2 , \tag{4.3}$$

where τ is the pulse duration [s], n_m is the number of moles [mol] of the reacted species, ΔE_s is the change in steady state potentials between titration steps, and ΔE_t is the change in potential during applied pulse neglecting any IR drops. The IR drop occurs due to the instantaneous voltage increase/drop during a current pulse. Figure 4.1 illustrates the meaning of the change in the potentials and where they occur in relation to the pulse duration. The GITT method is deemed slightly more accurate than the PITT method since one is able to visualize and account for the IR potential drops. Therefore, any electrical impedances in the cell do not contribute to the error in calculating the diffusion coefficient, which is a recognizable problem in the PITT experiment.
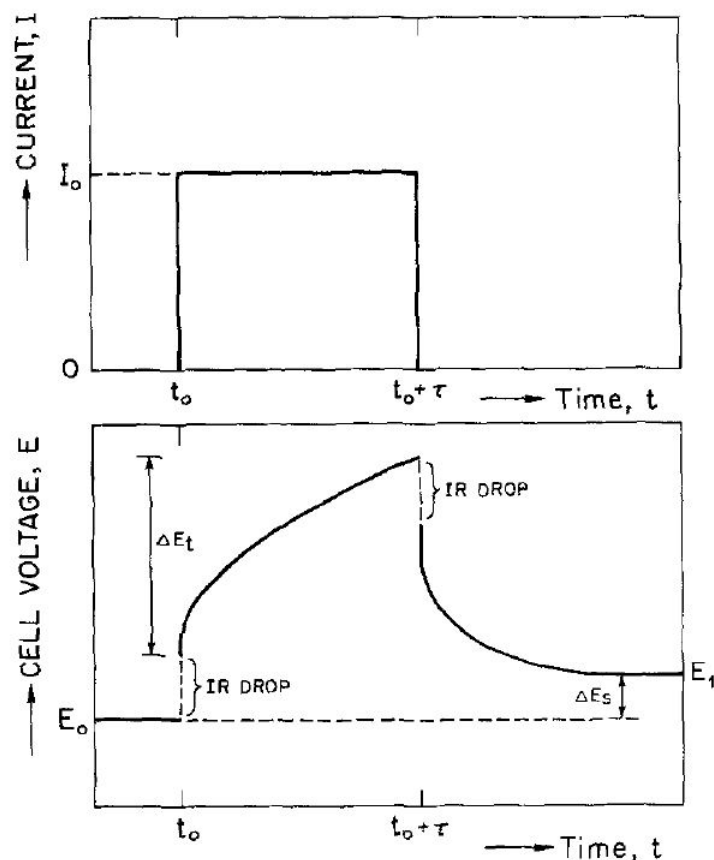
Figure 4.1: This figure is taken from Weppner and Huggins (1977) and depicts a typical potential vs. time curve during a GITT experiment. ΔE_s represents the change in potential from the new steady state voltage compared to the initial voltage. ΔE_t represents the potential increase during the applied current and can be approximated by a linear relation when plotted against $\sqrt{t}$.

Various authors, such as Weppner and Huggins (1977), Wen et al. (1981), and Verma et al. (2017) among others, have experimentally used this technique to determine properties for Li_3Sb, $LiAl$, and $LiNi_{0.5}Co_{0.2}Mn_{0.3}O_2$, respectively. The experimental data provided in Verma et al. (2017) correlates well to previous data in the literature. The authors also used a single particle model to simulate the GITT experiment and it compared extremely well to their experiments. Deiss (2005) also used the GITT method to show the dependence of reaction kinetics in the theoretical solutions. The original method assumes infinitely fast kinetics such that surface lithium ions are quickly adsorbed into the electrode and diffusion can then take place. However, Deiss (2005) and Deiss et al. (2001) numerically solved the mass conservation PDE equation and back-solved for the electric potential as a function of

time given the flux boundary condition in terms of a Butler-Volmer expression for the reaction kinetics. Their additional simulations showed that no choice for the reaction rate constant would yield the constant numerical input for the diffusivity. Increasing the reaction rate to a sufficiently high value yielded the most accurate result as the diffusion was calculated to be constant but slightly lower than the initial input value. However, for a reasonable reaction rate, the results showed oscillatory behavior and performed worse as the rate decreased.

Furthermore, Falconi (2017) simulated this method using a porous electrode model and also discovered non intuitive behavior. They solved for the separate diffusivities of the liquid and solid components in the porous electrode and unexpectedly found a similar voltage behavior between the liquid and solid materials given a certain range of current amplitudes and pulse duration times. Changing these parameters yielded more reasonable plots, but the theory shows an ambiguity and/or discrepancy in using the experiment for porous electrodes. These studies show the scrutiny involved in carrying out these experimental techniques and interpreting the results. The analytical expressions are derived for important electrode material properties, and careful examination of the assumptions used could be needed. This questions the validity of these experiments for complicated electrode behaviors.

4.2.1 GITT Simulation Results

With our simulation model, we attempt to recreate the GITT experiment and qualitatively show the sensitivity of the theory to changes in reaction kinetics. We mimic the one dimensional geometry of the original experiment, which is very suitable for our finite element model. We will now assume axisymmetric conditions for the simulation solution. The FEM mesh is composed of a cylindrical block of an anode electrode, electrolyte separator, and a cathode electrode. We attempt to recalculate the diffusion constant of the cathode material, as in the original experiment. The radius W of the cell is 1 μm, the width of the anode/cathode $L_A = L_C$ is 40 μm, and the width of the separator L_S is 10 μm. The geometry is shown in Figure 4.2. The anode material properties do not matter as long as the reaction rate at the electrolyte interface is sufficiently fast compared to the cathode to allow for uniform lithium concentration within the separator. The cathode is chosen to be Lithium Nickel Manganese Cobalt Oxide (NMC) with a constant input value of $D = 1 \times 10^{-13}\,\mathrm{m^2/s}$ for the diffusion coefficient. In this section, the mechanical and thermal changes are not included and the relevant properties of the cathode, anode, and electrolyte separator are presented in Table 4.1. We perform the analysis by beginning with an appropriate initial concentration in the cathode, apply appropriate FEM boundary conditions to mimic the GITT experiment, post process the results at the present concentration, and then repeat these steps at a new initial concentration.

At the right edge of the cathode $z = L$, we apply a current of magnitude $i = 0.01\,\mathrm{A/m^2}$. The pulse period lasts for a duration of 150 seconds and the relaxation time is 3600 seconds. The long relaxation time is chosen so that the lithium concentration in the cathode will be completely homogeneous at the end of each applied voltage pulse. The potential and concentration values are sampled at the cathode/electrolyte interface (green/red intersection

in Figure 4.2). Lastly, the potential is fixed at at the left edge of the anode, $\phi(z = 0) = 0$. These are the only boundary conditions used in simulation, which exactly mimics the assumptions used for the boundary conditions in the original GITT experiment.

We simplify the GITT equations by using the relations $d\delta = V_m dc$ and $n_m V_m = V$, where V is the total volume of the electrode accounting for the 2π rotation about the azimuth axis in the axisymmetric formulation. Here V would symbolize the volume of just the cathode portion in the mesh. The equations can then be manipulated in multiple forms:

$$D = \frac{4}{\pi} \left(\frac{i}{z_A F} \right)^2 \left(1 / \frac{dc}{d\sqrt{t}} \right)^2 , \tag{4.4a}$$

$$D = \frac{4}{\pi} \left(\frac{i}{z_A F} \right)^2 \left(\frac{dE}{dc} \Big/ \frac{dE}{d\sqrt{t}} \right)^2 , \tag{4.4b}$$

$$D = \frac{4}{\pi\tau} \left(\frac{1}{L_{eff}} \right)^2 \left(\frac{\Delta E_s}{\Delta E_t} \right)^2 , \tag{4.4c}$$

with L_{eff} [m] being the effective length of the electrode; i.e. $L_{eff} = V/S$. S is the total contact area between the electrode and electrolyte. In this section, it is equal to the cathode length L_C. In the experiment and simulation solution, one controls the application of the current density i and needs to measure the transient responses of lithium concentration c and electric potential E in the electrode at its junction with the electrolyte.
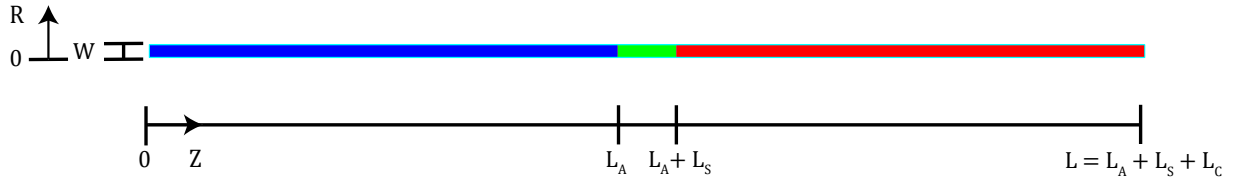
Figure 4.2: Cylindrical geometry for the FEM mesh with $W = 1, L_A = 40, L_S = 10$, and $L_C = 40$ all measured in micrometers. The lithium anode is shown in blue, the electrolyte separator in green, and the NMC cathode shown in red. The current pulse is applied at the right edge $z = L$ with the potential being grounded to zero at $z = 0$. Note the image is not to scale to show the outline of the mesh clearly.

The reaction kinetics at the electrode-electrolyte interface is modeled via the symmetric Butler-Volmer equation,

$$R_{BV} = 2k_R \sqrt{c_E} \sqrt{c_S} \sqrt{c_S^{max} - c_S} \cdot \sinh \left(-\frac{F}{2RT} \eta \right) \tag{4.5}$$

where we assume $\alpha = 1/2$ from Equation (2.75) and $\eta = \phi_S - \phi_E - U_0(\bar{c})$. We do not account for any film growth or potential drops due to film growth. The current pulse will

increase the potential in the cathode ϕ_S and result in lithium deinteracaltion. Ions migrate
from the cathode to the anode via the electrolyte pathway. Butler-Volmer elements exist at
the interfaces between the anode or cathode material elements and the electrolyte material
elements. $U_0(\bar{c})$ is chosen to be zero for the anode to represent a block of pure lithium metal.
From Wang, Siegel, and Garikipati (2017), the open circuit potential used for the NMC
cathode is

$$
\begin{aligned}
U_0(\bar{c}) \;=\; & \left(-0.0923 - 7.82\bar{c} + 50.07\bar{c}^2 - 122.28\bar{c}^3 + 82.98\bar{c}^4 + 140.29\bar{c}^5 - 374.73\bar{c}^6 \right. \\
& \left. + \; 403.25\bar{c}^7 - 221.19\bar{c}^8 + 49.33\bar{c}^9 \right) \Big/ \left(-0.02 - 1.9\bar{c} + 11.73\bar{c}^2 - 28.78\bar{c}^3 \right. \\
& \left. + \; 27.54\bar{c}^4 - 8.63\bar{c}^5 \right),
\end{aligned}
$$

where $\bar{c} = c_S/c_{max}$ is the normalized surface concentration with respect to the maximum
lithium concentration attainable. Figure 4.3 illustrates the change in U_0 as a function of $\bar{c}$.
We choose $c_{max} = 30,000 \, \text{mol/m}^3$ and the reaction rate $k_R = 1 \times 10^{-8} \, \text{m}^{5/2}/s\sqrt{\text{mol}}$ for both
the anode and cathode reactions.
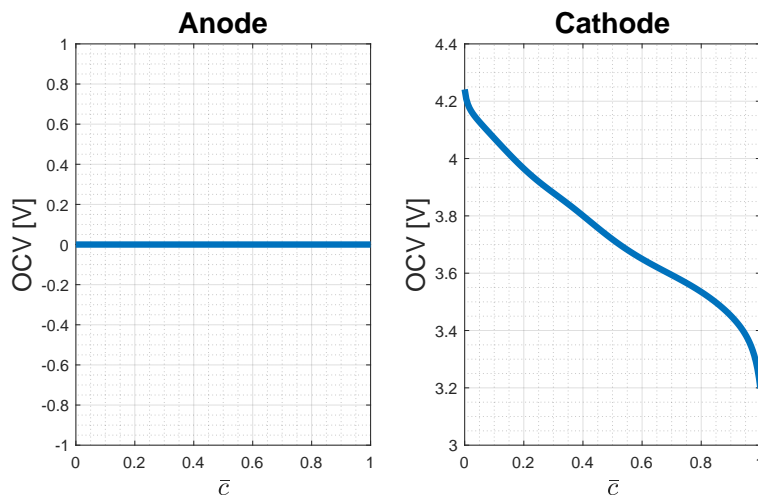
Figure 4.3: Open circuit voltages as a function of normalized concentration $\bar{c} = c_S/c_{max}$
where c_S is the active particle concentration evaluated at the surface of the elec-
trolyte/electrode interface.

NMC Cathode Properties			
Parameter	Unit	Value	Description
D	m^2/s	$1.0 \cdot 10^{-13}$	Diffusion coefficient
κ	S/m	$1.0 \cdot 10^{2}$	Electrical conductivity
Electrolyte Properties			
Parameter	Unit	Value	Description
D	m^2/s	$1.0 \cdot 10^{-10}$	Diffusion coefficient
κ_{eff}	S/m	1.0	Electrical conductivity
t_+	-	0.4	Transference Number
$\frac{\partial \ln \gamma_\pm}{\partial \ln c}$	-	0.3	Thermodynamic factor
c_0	mol/m^3	1000	Initial concentration
Lithium Anode Properties			
Parameter	Unit	Value	Description
D	m^2/s	$1.0 \cdot 10^{-11}$	Diffusion coefficient
κ	S/m	$1.0 \cdot 10^{3}$	Electrical conductivity
c_0	mol/m^3	15,000	Initial concentration

Table 4.1: Material parameters needed in the simulation input.

We perform the analysis beginning with an initial concentration in the cathode, mimic the GITT experiment, post process the data, and then redo this cycle for a new initial concentration. The diffusion values calculated from Equations (4.4a)-(4.4c) perform extremely well and are shown in Figure 4.5(a). Equation (4.4a) is noted as EQ_1 in the figure and only has a 0.1% error. The input values to these equations are taken from the potential jumps and derivatives shown in Figure 4.4. For the first $\tau = 150\,\text{s}$, we fit a linear polynomial to obtain the slope of the c_S vs. $\sqrt{t}$ and ϕ_S vs. $\sqrt{t}$ curves yielding $dc/d\sqrt{t}$ and $dE/d\sqrt{t}$, respectively. The analysis runs for various c_0 values, and we can see that the linear approximation, Equation (4.4c), performs the worst as expected. Overall, the approximate results we obtain with our FEM model work remarkably well. The difference between our simulation runs and the analytical expressions in Weppner and Huggins (1977) is the consideration of realistic reaction kinetics and potential gradient effects. These phenomena should be considered when interpreting the diffusivities obtained from GITT experiments but are impossible to correct for. However, from a simulation perspective, we can handle these shortcomings easily. Figure 4.5(b) demonstrates the values of D obtained from the GITT expressions above for changing the reaction constants of the anode and cathode from $k_R = 1.0 \times 10^{-8}$ to $k_R = 1.0 \times 10^{0}$. We can see that we obtain much better accuracy from Equation (4.4b), EQ_2 in the figure, but Equation (4.4c) performs worse, EQ_3 in the figure. The oscillations previously present are less chaotic as well. It is just a simple change in the simulation, but it seems that the GITT experiment is sensitive to reaction kinetics, which it neglects. Albeit the Butler-Volmer equation is an empirical approximation, but it corresponds to physical

phenomena occurring at the interface between the bulk electrodes and the electrolyte. An analytical correction to the GITT experiment accounting for these shortcomings is extremely complicated and would have to be solved numerically. This would detract from the simplicity of the original experiment. However, it is satisfying to know that we can computationally see these sensitivities by a priori knowing the value of D we should obtain.

Changing anode, cathode, and electrolyte electrical conductivities values shown in Table 4.1 to $\kappa = \kappa_{eff} = 1 \times 10^4$ S/m provides the best approximation and almost completely reduces the oscillations. This is illustrated in Figure 4.6. Additionally, the approximation with expression EQ_2 is almost identical to the true value. with only approximately a 0.5% error now. Unfortunately, the values used for the conductivities are unrealistic for conventional anodes and electrolytes. One interesting outcome is that EQ_1 (Equation (4.4a)) consistently is accurate with less than 0.5% error for any reaction rate or conductivity value used. If one is capable, measuring the concentration changes in the electrode as function of time instead of potential changes could be one useful adjustment experimentally. This could bypass a lot of error associated with true physical phenomena that occur during any GITT experiment. This unfortunately seems unrealistic and arduous as the concentration measure would have to be sampled at the location where it meets the electrolyte.
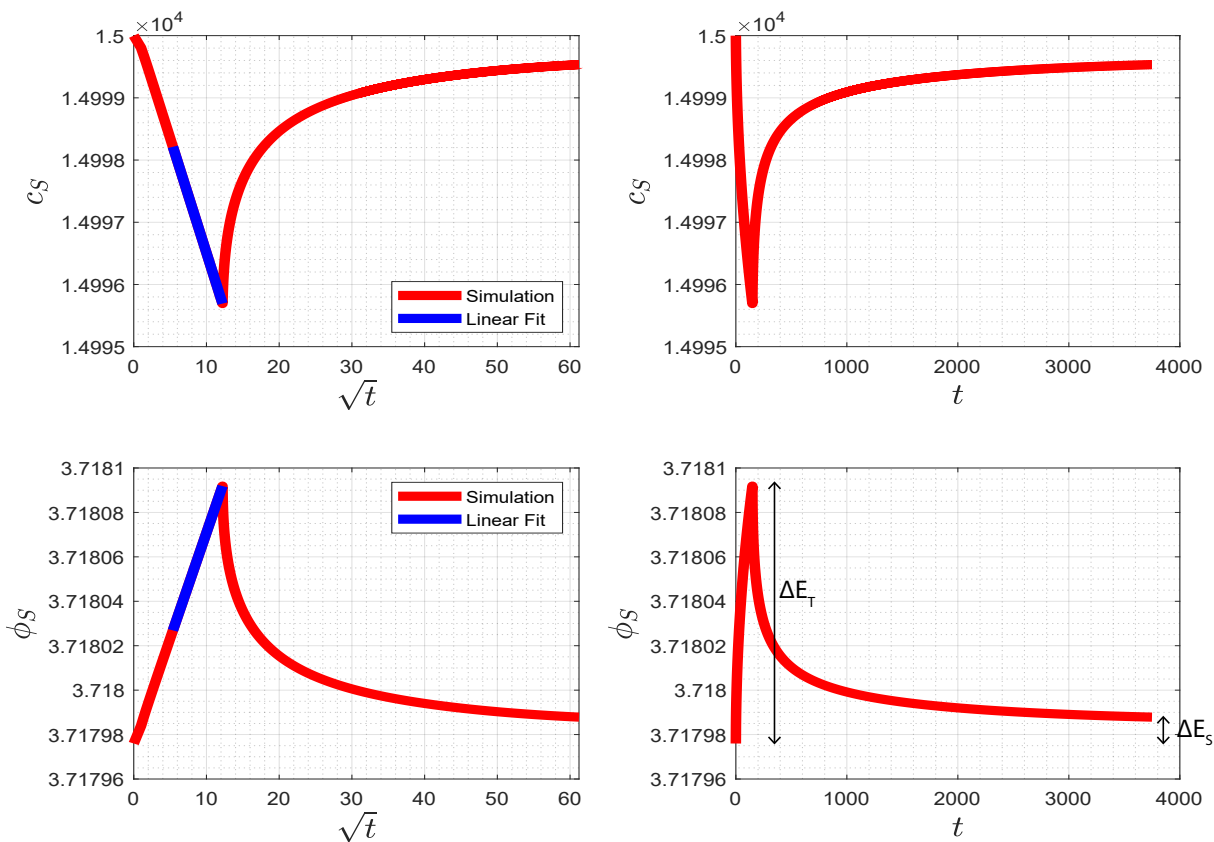
Figure 4.4: Typical concentration and potential profiles during one step of the GITT simulation. Here the NMC initial concentration is $c_0 = 15,000 \, \text{mol/m}^3$. The linear fit of the concentration and potential vs. $\sqrt{t}$ is shown in blue in the left sub figures. $dc/d\sqrt{t}$ and $dE/d\sqrt{t}$ are taken as the slope of the linear fits, respectively. ΔE_t and ΔE_s are shown in the bottom right figure. Our simulation model does not predict any IR drop.

(a) $k_R = 1 \times 10^{-8}$

(b) $k_R = 1 \times 10^{0}$
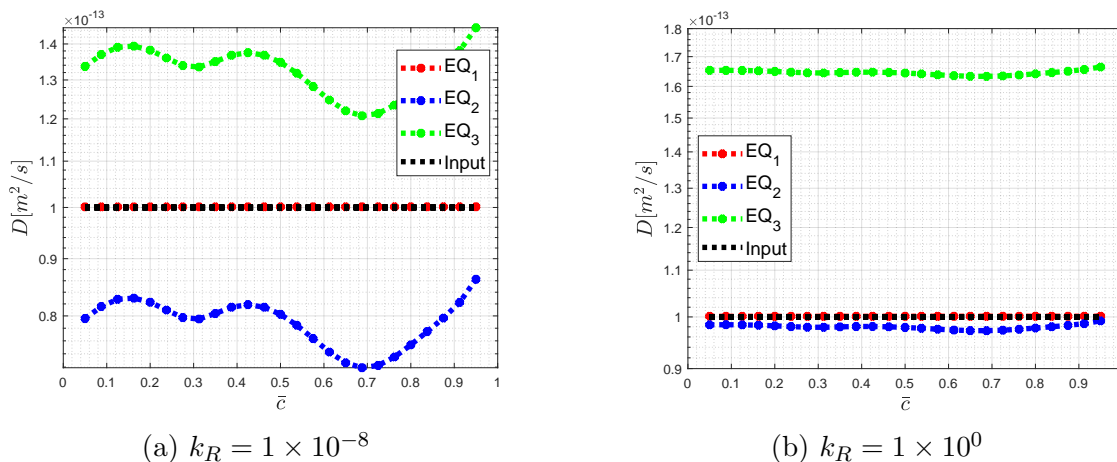
Figure 4.5: D is calculated through the 3 separate formulas presented in Weppner and Huggins (1977). EQ_1 is Equation (4.4a), EQ_2 is Equation (4.4b), and EQ_3 is Equation (4.4c). As expected the linear approximation made in EQ_3 performs the worst and small oscillations only occur with EQ_2 and EQ_3. In both (a) and (b), EQ_1 lies directly beneath the input value for D and performs remarkably well.
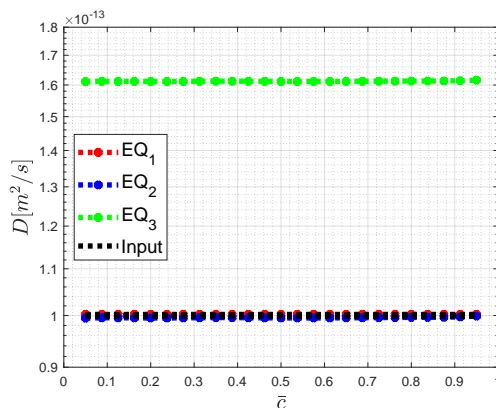
Figure 4.6: For $k_R = 1 \times 10^{0}$ and all electrical conductivity values $\kappa = \kappa_{eff} = 1 \times 10^{4}$, we recalculate D. It is apparent that higher reaction rates and conductivities mitigate the oscillations present in Figure 4.5 as both EQ_1 and EQ_2 lie beneath the input value of D in this figure. Again, EQ_1 is Equation (4.4a), EQ_2 is Equation (4.4b), and EQ_3 is Equation (4.4c).

We are even able to recalculate the true value of the input diffusion even if it is a nonlinear function of concentration, $D = D(\bar{c})$. We fitted a smooth spline curve to experimental

diffusion values from the GITT experiment in Ecker et al. (2015). The values vary with concentration and is shown in Figure 4.7. We use the same geometry and material properties in Table 4.1 with the exception of varying k_R [m$^{5/2}$/s$\sqrt{\text{mol}}$]. EQ_1 and EQ_2 again perform extremely well for both reaction rates tested. The linear approximation formula EQ_3 has significant error as expected. These simulations are reassuring that we can achieve what we want to see from the GITT experiment. However, the numerical oscillations seen in both runs and loss of accuracy using Equation (4.4c) question the efficacy of the GITT experiment for realistic porous electrodes. Our simulations show the sensitivity these expressions have for an extremely idealized case, so caution should be used when interpreting oscillations and data outliers in experimental data.

(a) $k_R = 1 \times 10^{-8}$ (b) $k_R = 1 \times 10^0$
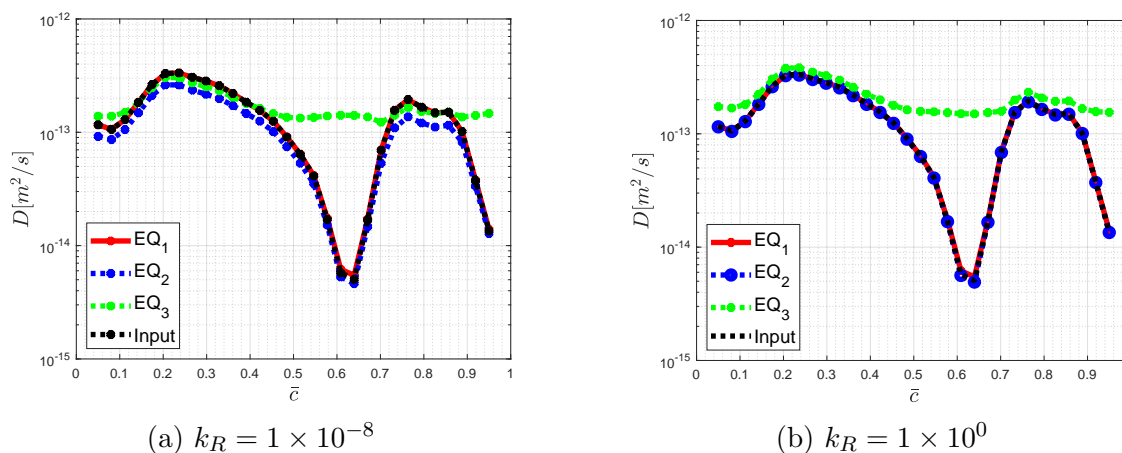
Figure 4.7: $D(\bar{c})$ data is taken from Ecker et al. (2015) with material properties in Table 4.1. In the figure, EQ_1 coincides directly with the input value for both (a) and (b). EQ_2 only coincides directly with the input value for (b). EQ_1 is Equation (4.4a), EQ_2 is Equation (4.4b), and EQ_3 is Equation (4.4c).

4.3 Potentiostatic Intermittent Titration Technique

Originating back to Yao, Heredy, and Saunders (1971), the PITT experiment is the predecessor of the GITT method. It still is a widely used technique to determine the diffusion coefficient. Metrohm Autolab (Autolab, 2014b) describes the procedure in more detail, but the experiment begins by first determining the initial open circuit potential U_0 of the battery half cell. Then, a potential pulse at U_0 is switched on for a pulse duration τ followed by an appropriate relaxation time allowing for the cell's electric current to equilibrate. Next, a 0.02 V increment is applied to U_0 for the same time τ along with the same amount of relaxation time as in the previous step. During this process, the transient current response is measured. This process is repeated in 0.02 V increments until the terminal voltage of the cell is reached. Figure 4.8 illustrates a qualitative plot of one increment. The diffusion

coefficient is implicitly given in the equation for the transient current,

$$I(t) = \frac{2z_A FS(c_S - c_0)D}{L} \exp\left(-\frac{\pi^2 Dt}{4L^2}\right) , \tag{4.6}$$

where S is the surface area of the electrode/electrolyte interfaces [m^2], c_S [mol/m^3] is the surface concentration at time t, c_0 [mol/m^3] is the initial surface concentration at the beginning of the pulse, and L is the characteristic length of the electrode. One can then determine D from the slope of the natural log of Equation (4.6) yielding

$$D = \frac{d\ln(I)}{dt} \cdot \frac{4L^2}{\pi^2} . \tag{4.7}$$

Equations (4.6) and (4.7) are only valid for $t >> L^2/D$. Note that D can also be calculated through the y-intercept of a $\ln(I)$ vs. t plot. The validity of these equations varies from the GITT relations, which are valid for $t << L^2/D$. If this is the case then an alternate formula may be used,

$$I(t) = z_A FS(c_S - c_0)\sqrt{\frac{D}{\pi t}} , \tag{4.8}$$

and D can be determined by the slope of $I(t)$ vs. $t^{-1/2}$,

$$D = \pi \left(\frac{dI}{d(1/\sqrt{t})} \cdot \frac{1}{z_A FS(c_S - c_0)}\right)^2 . \tag{4.9}$$

Note that $I(t)$ has units of amps [A] in both relations. The current density i [A/m^2] can be obtained by dividing I by the area of where the current is applied. Because the electrode potential is controlled, one can effectively measure chemical properties without any phase transformations occurring. The potential can be incremented within a certain stability window to negate any known phase transformations or undesired chemical reactions. However, a disadvantage of the PITT method is the inevitable ohmic potential drop due to the electrolyte electrical resistance and cannot be entirely eliminated. One way to mitigate this is to place the reference electrode geographically very close to the sample electrode so that the current travels less distance in the battery circuitry (Wen et al., 1981).
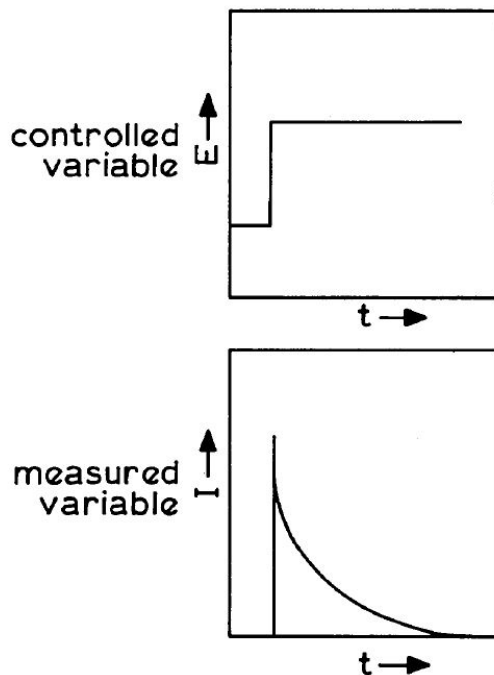
Figure 4.8: In a typical PITT experiment, the potential is pulsed and the current as a function of time is measured. The diffusivity can then be determined by a linear plot of $\ln I$ vs. t in Equation (4.6). This figure is obtained from Wen et al. (1981).

Among others, Li et al. (2011) used the PITT theory along with incorporation of interfacial reaction kinetics to study the effect of finite interfacial reaction rates. This is similar to the work done by Deiss (2005) for the GITT experiment. They find that when the surface reaction is the rate limiting factor, the concentration within the bulk material increases slower than expected and the diffusion coefficient can be underestimated. This is also a similar case for the galvanostatic step technique. Montella (2002) also studied the limitations of neglecting finite reaction rates and the inevitable ohmic potential drop due to cell impedance. The authors studied these limitations by considering equivalent circuit models and deriving a modified theory to calculate the diffusivity. They determined that using the PITT experiment can only accurately determine D if the measurement involves very fast reaction kinetics, negligible ohmic drops, negligible film resistance at electrode interfaces, and no phase transformations.

4.3.1 PITT Simulation Results

In our simulation, we will vary the reaction kinetics and execute the PITT experiment. We use the same mesh and geometry from the previous GITT simulation, which is shown below

in Figure 4.9 for clarity. The initial material parameters are also the same as those in Table
4.1 with the reaction rate $k_R = 1.0 \times 10^{-8} \, \text{m}^{5/2}/s\sqrt{\text{mol}}$ for both the anode and cathode.
Again, the anode mimics pure lithium metal and the cathode is NMC. Our model will begin
at a cathode initial concentration c_0 and electric potential equal to its corresponding open
circuit voltage $U_0(\bar{c}_0 = c_0/c_{max})$. We let the system equilibrate naturally by holding the
potentials fixed at $z = 0$ and $z = L$ to their initial values for 60 seconds,

$$z = 0 \quad \rightarrow \quad \phi = 0 \, ,$$
$$z = L \quad \rightarrow \quad \phi = U_0(\bar{c}_0) \, .$$

Then, at $z = L$ we will apply a potential jump of 0.02 V for 900 seconds and extrapolate
data from the $I(t)$ vs. t curve, i.e. at $z = L \rightarrow \phi = U_0(\bar{c}_0) + 0.02$. The input diffusion value
we seek to recalculate is $D = 1 \times 10^{-13} \, \text{m}^2/\text{s}$ with a cathode length $L_C = 40 \, \mu\text{m}$. For this
case, we use Equation (4.9) to determine D as $t << L_C^2/D$. We fit a linear polynomial to
$I(t)$ vs. $1/\sqrt{t}$ to determine D from the slope of this linear fit. We work with the current
density $i(t) = I(t)/S$, in which the S corresponds to the area of the applied current. This
area is also equal to the area of the interface between cathode/electrolyte. In the simulation,
$S = \pi \, \mu\text{m}^2$ and the rest of the geometry is shown in Figure 4.9.

Similar to the GITT simulation, we begin with various initial concentrations, execute
potential jumps at $z = L$, and then calculate D from Equation (4.7). We can see from
Figure 4.10 that test simulation runs well but with about a 45% overestimation error. There
are no oscillations present as previously seen in the GITT simulation, but our approximation
is much less accurate. The accuracy loss is also seen in experimental data, and could be an
inherent flaw in the analytical derivation. Varying the reaction rate k_R from 1×10^{-8} to
$1 \times 10^0 \, \text{m}^{5/2}/s\sqrt{\text{mol}}$ shows no change in accuracy. This is pleasing to see, as it can possibly
validate the interpretation of the GITT experiment. If GITT data is unclear, then one
can use the PITT experiment as a tool to determine a better estimate and rule out some
sensitivity due to reaction kinetics.
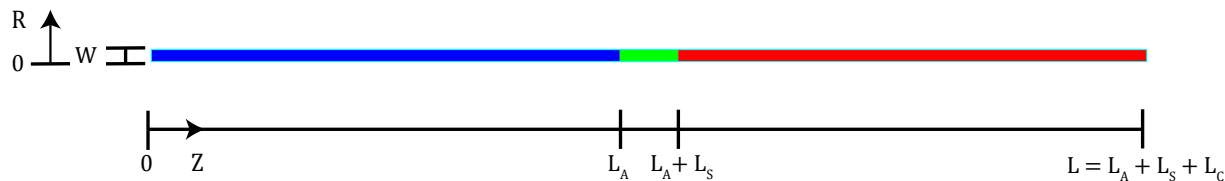
Figure 4.9: Planar geometry for the FEM mesh with $W = 1, L_A = 40, L_S = 10, L_C = 40$ all
measured in micrometers. The lithium anode is shown in blue, the electrolyte separator in
green, and the NMC cathode shown in red. The potential jumps are applied at the right
edge $z = L$ with the potential being grounded to zero at $z = 0$.

(a) $k_R = 1 \times 10^{-8}$

(b) $k_R = 1 \times 10^0$
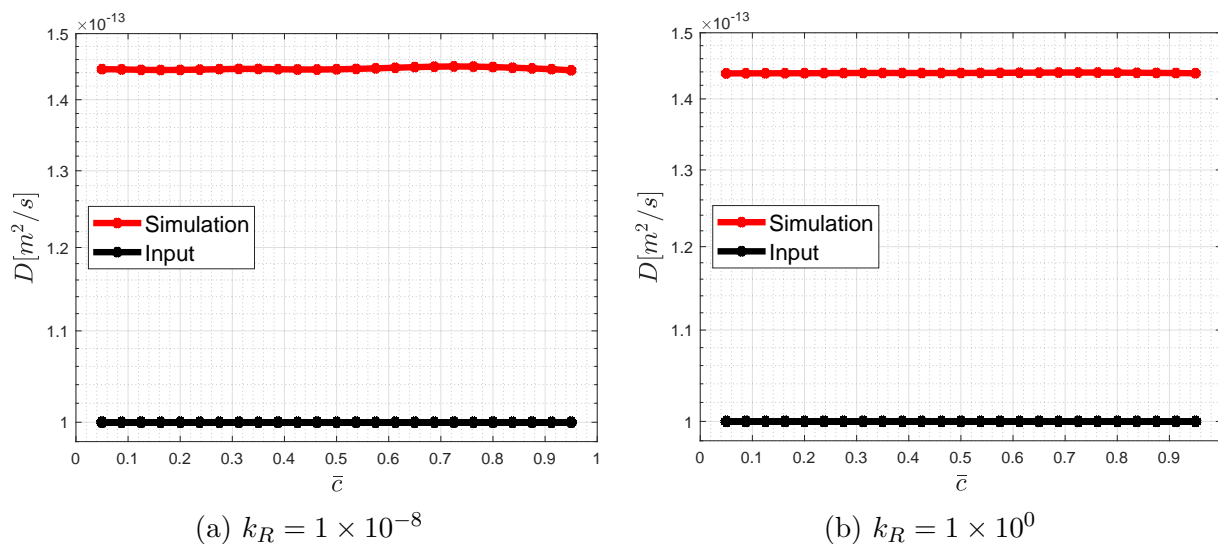
Figure 4.10: PITT simulation using the short time approximation Equation (4.9). Increasing the reaction constant in the PITT simulation shows that there is no significant influence in the relation we obtain for D.

The linear plot of i vs. $1/\sqrt{t}$ is shown for $\bar{c}_0 = 0.95$ ($c_0 = 28,500 \, \text{mol/m}^3$) in Figure 4.11. We are able to obtain a great fit to the data and the physics qualitatively match our intuition. At the beginning time step, the potential is held fixed to its equilibrium value and there is no current within the electrode. Once the potential is increased to a new value, equilibrium is not satisfied and there is a corresponding increase in current. A reaction occurs at the electrode's interface with the electrolyte, resulting in lithium ions leaving the electrode. The flux of ions corresponds to an electric current, which decreases with time as a new equilibrium value is achieved. Holding the potential at this new value will eventually result in zero current signifying a new equilibrium state.
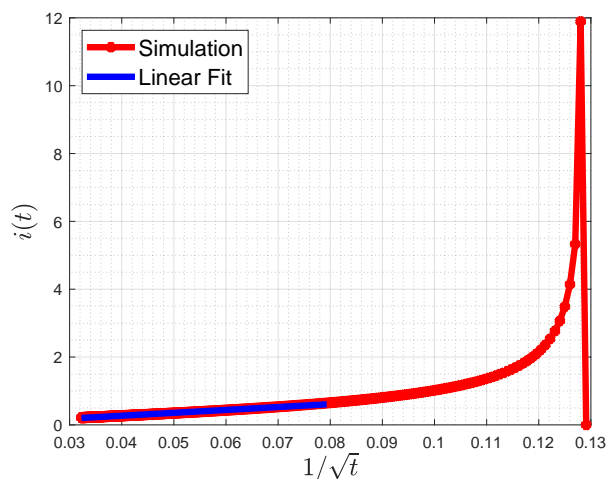
Figure 4.11: $i(t)$ vs. $1/\sqrt{t}$ curve, where i is measured in A/m^2. We fit a linear polynomial towards the end of the curve, as there is some nonlinearity in the initial stages of the potential jump. The current is initial zero at $t = 60$ s, and then the large increase in i for immediately after shows when we applied the potential increase $U_0 + 0.02$ V.

In Figure 4.12, we change the geometry very slightly by increasing the anode, cathode, and electrolyte lengths while keeping the width the same. In this case, $L_A = L_C = 100\,\mu$m and $L_S = 20\,\mu$m. Visually, the larger cathode length performs worse, but could be a result of numerical precision or sensitivity in determining the slope of the linear plot i vs. $1/\sqrt{t}$. There is about an approximate 10-20% error when using different data points in time for determining the slope of i vs. $1/\sqrt{t}$. The most accurate slope measurements are achieved for points in time closer towards the end of the applied potential pulse. Both estimates using the original lengths and the newly defined lengths are of the same order of magnitude and vary only by a couple percent. This run verifies that our PITT simulation is not sensitive to geometry or reaction rates.
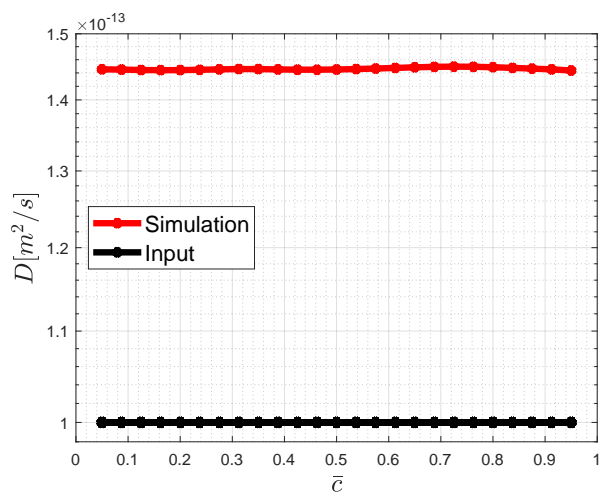
(a) $L_C = 40\,\mu\text{m}$
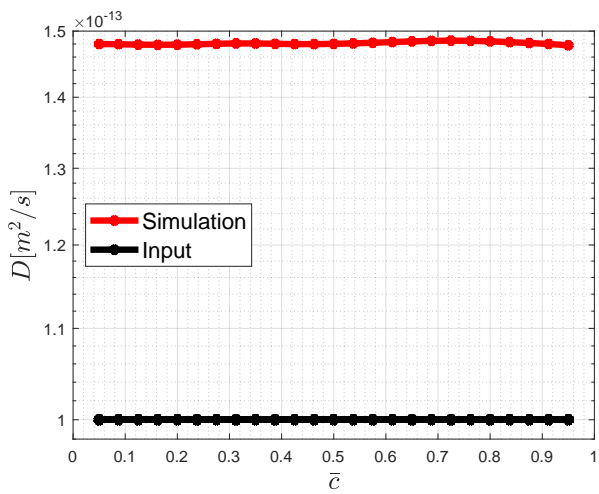
(b) $L_C = 100\,\mu\text{m}$

Figure 4.12: This figure shows the results in varying the cathode length using the short time approximation, Equation (4.9).

Chapter 5

Geometrical Effects on Aging Mechanisms

This chapter focuses on geometrical effects on SEI formation, lithium plating, and stress concentrations. Porous electrode theory idealizes the electrode's microstructure and assumes smooth spherical particles. However, it is well known in structural mechanics that for small deviations in smooth geometries a large impact on stress concentrations can be seen and are the basis of many early engineering failures. It will be shown in this section that the same phenomena occurs in reaction rates as well as mechanical stresses within the active particle.

5.1 Geometrical Variance Simulation

We consider three similar geometrical configurations that are realistic representative particles within an electrode. The geometric meshes are labeled $\{1, 2, 3\}$ in Figure 5.1 with $R_1 = 10\,\mu$m, $R_2 = 2\,\mu$m, and $R_D = 8\,\mu$m in MESH 3. We use our axisymmetric elements such that MESH 1 represents the hemisphere a spherical particle given a 2π rotation into the page. MESH 2 characterizes the smooth curve given in MESH 1 by sharp edges, and MESH 3 assumes a smooth outer surface but a nonuniform particle radius. MESH 3 yields the most interesting results as it has the highest stress concentrations and fastest reaction rates resulting in a desired increase in lithium intercalation but also undesired increases in the SEI and plated lithium film thickness. Similar results are shown for MESH 2 but not as pronounced.
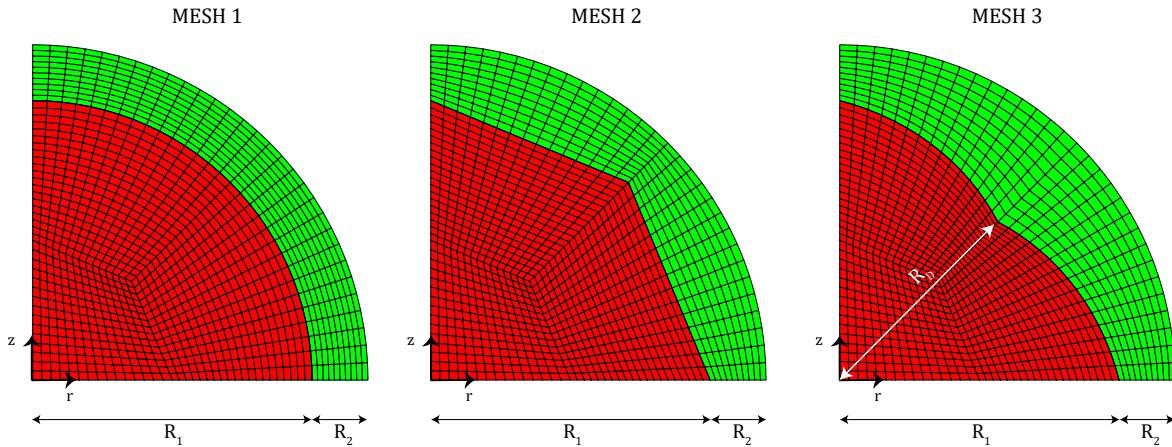
Figure 5.1: This section considers three variances in spherical geometry, where active particle material is shown in red and the surrounding electrolyte shown in green. Interface elements lie at the junctions of all particle and electrolyte elements. MESH 1 is the control test case, while MESH 2 and MESH 3 are sample geometries that can easily be good representations of a realistic microstructure. The active particle elements are shown in red and the electrolyte elements are shown in green. $R_1 = 10\,\mu\mathrm{m}$, $R_2 = 2\,\mu\mathrm{m}$, and $R_D = 8\,\mu\mathrm{m}$.

The boundary conditions, number of elements, and material properties for all three meshes are the same. The only variance is the geometrical representation of the electrode and consequently the electrolyte interface. We begin with initial concentrations of $1580\,\mathrm{mol/m^3}\,(0.05 c_{max})$ and $1000\,\mathrm{mol/m^3}$ in the particle and electrolyte elements, respectively. A theoretical estimate of $c_{max} = 31,600\,\mathrm{mol/m^3}$ is based on the molar mass and density of lithium graphite, as also shown in Ecker et al. (2015). The Dirichlet boundary conditions are: $\phi(r = 0, z = 0) = 0$, $u_r(r = 0, z) = 0$, and $u_z(r, z = 0) = 0$. At the outer surface of the electrolyte, $\sqrt{z^2 + r^2} = (R_1 + R_2)$, there is an applied current of $1.25\,\mathrm{A/m^2}$ with a corresponding applied flux of $1.2955 \times 10^{-5}\,\mathrm{mol/m^2 s}$. We carry out the simulation solution for 3600 s with these boundary conditions remaining constant. At the electrode-electrolyte interface, there are Butler-Volmer interface elements allowing the transfer of ions, current, and heat between the two materials. The remaining material properties are given in Table 5.1 and Table 5.2. The open circuit voltage $U_0(\bar{c})$ is given in Equation (3.30) as it is assumed the active particle is lithium graphite. The differences in temperature distributions for the three separate configurations are not significant in the analysis and is omitted in the results.

Figure 5.3 illustrates the growth of the SEI thickness, plating thickness, and the von Mises stress across the radial coordinate r. These values are taken from the Butler-Volmer interface elements, which lie between the outer surface of the active particle and electrolyte. From the figure below, one can see that there is about a 16% and 56% increase in the total film thickness in going from MESH 1 to MESH 2 and from MESH 1 to MESH 3, respectively. The variance in geometry affects lithium plating more than SEI growth. A

Parameter	Units	Particle	Electrolyte	Description
E	N/m^2	5.89×10^9	3.0×10^5	Young's Modulus
ν	-	0.30	0.49	Poisson ratio
ρ	kg/m^3	2.5×10^3	1.1×10^3	Density
Ω	m^3/mol	2.88×10^{-6}	0	Lithium swelling
α	1/K	6.0×10^{-6}	12.46×10^{-6}	Thermal expansion
T_0	K	298.0	298.0	Initial Temperature
C$_P$	J/kg·K	7.0×10^2	1.8×10^3	Specific heat
λ	W/m·K	1.04	0.01	Thermal conductivity
D	m^2/s	2.58×10^{-14}	3.23×10^{-10}	Diffusion coefficient
κ	S/m	1.0×10^2	1.0	Electrical conductivity
t_0	-	-	0.435	Transference number
$\partial \ln \gamma_{\pm}/\partial \ln c$	-	-	0.43	Thermodynamic factor

Table 5.1: Material parameters used for every mesh in this section. Some properties are taken from Ecker et al. (2015) while others are assumed.

56% increase in unwanted film growth is a significant result, but there is about a 35% increase in lithium intercalation into the active particle as well. Figure 5.2 illustrates the larger lithium concentration in the latter meshes compared to the control case. Slight kinks in a perfectly spherical particle produce an increase in reaction rates due to slight changes in the potential profiles of the active particle. The difference in potential between the particle ϕ_S and electrolyte ϕ_E along r becomes increasingly more negative from MESH $1 \rightarrow 2 \rightarrow 3$; see Figure 5.4. This directly increases the overpotential η and results in an exponential increase for intercalation, SEI, and lithium plating reactions.
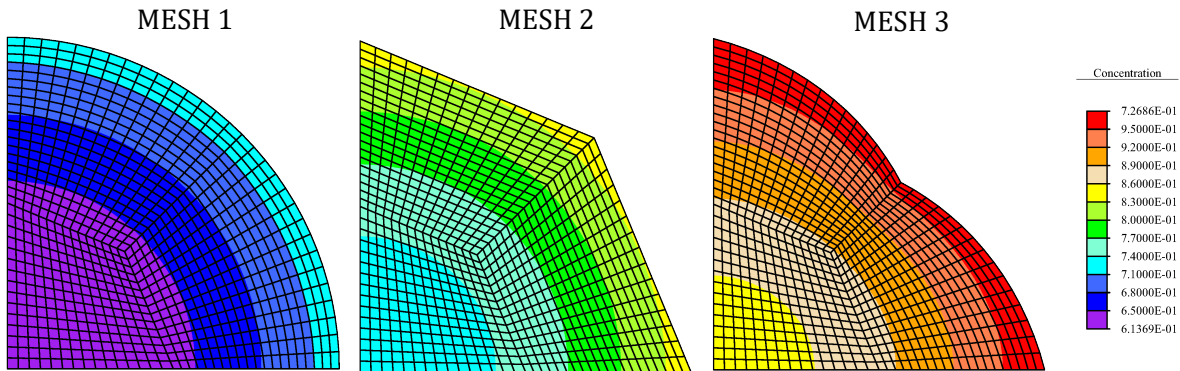
Figure 5.2: Normalized concentration c/c_{ref} profiles for three separate meshes.

Parameter	Units	Value	Description
k_R	$\mathrm{m}^{5/2}/\mathrm{s}\sqrt{\mathrm{mol}}$	1.76×10^{-11}	Intercalation reaction rate
$k_{0,SEI}$	m/s	7.0×10^{-11}	SEI reaction rate
$k_{0,plate}$	$\mathrm{mol/m^2 s}$	5.1822×10^{-8}	Plating reaction rate
$\alpha_{C,SEI}$	-	0.5	SEI symmetry reaction coefficient
$\alpha_{C,plate}$	-	0.5	Plating symmetry reaction coefficient
λ_{SEI}	1/m	3.0×10^6	SEI decay factor
λ_{plate}	1/m	3.0×10^6	Plating decay factor
β	-	0.0	Plating to SEI coefficient
M_{SEI}	kg/mol	0.162	SEI molar mass
ρ_{SEI}	$\mathrm{kg/m^3}$	1690	SEI density
C_{EC}^S	$\mathrm{mol/m^3}$	4541	Solvent surface concentration
U_{SEI}	V	0.4	SEI equilibrium potential
κ_{SEI}	S/m	5.0×10^{-6}	SEI electrical conductivity
z	-	1.0	SEI valency
c_{max}	$\mathrm{mol/m^3}$	31,600	Maximum concentration

Table 5.2: Reaction kinetic properties used in the Butler-Volmer interface elements. SEI and plating parameters are adopted (some adjusted) from Yang et al. (2017) and Safari et al. (2009). We assume zero initial film thickness for both reactions. Moreover, we also assume that there is an initial 1nm thick layer for δ_{SEI} while zero initial thickness for the δ_{plate} film layer.
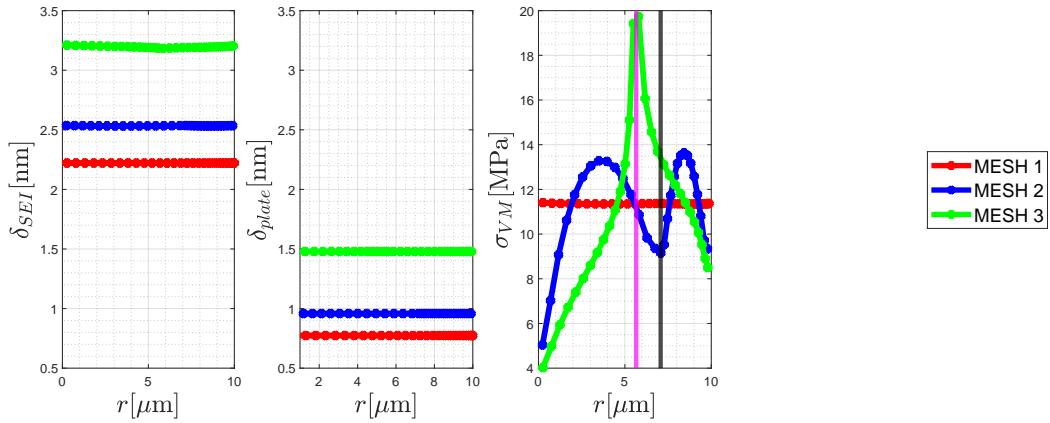
Figure 5.3: The film thickness and magnitude of the stress varies greatly from the ideal case, MESH 1, compared to MESH 2 and MESH 3. The horizontal axis depicts the radial coordination of the active particle. The SEI thickness is shown in the left, plating thickness in the middle, and von Mises stress in the right. The geometric imperfections in MESH 2 and MESH 3 are located at $7.071\,\mu$m (vertical black line) and at $5.657\,\mu$m (vertical purple line), respectively.

Figure 5.3 also shows the large variance in the von Mises stress at the particle's surface. The von Mises stress in polar coordinates is defined as

$$\sigma_{VM} = \frac{1}{\sqrt{2}} \sqrt{(\sigma_{rr} - \sigma_{\theta\theta})^2 + (\sigma_{\theta\theta} - \sigma_{zz})^2 + (\sigma_{zz} - \sigma_{rr})^2 + 6\left(\sigma_{\theta z}^2 + \sigma_{rz}^2 + \sigma_{r\theta}^2\right)}, \qquad (5.1)$$

where $\sigma_{\theta z} = \sigma_{r\theta} = 0$ for axisymmetric elements. The defect positioned at 45° between the r and z axes creates about a 65% increase in the maximum stress obtained at the surface. The peak of the stress occurs at this specific angle. The surface stresses fluctuate greatly and are not uniform. From Figure 5.5, we can visualize the individual stress profiles for $\{\sigma_{rr}, \sigma_{zz}, \sigma_{rz}\}$ and see their changes as MESH 1 becomes more concave. σ_{rz} shows the greatest change at the indent. σ_{rr} and σ_{zz} do not show such a large discrepancy.
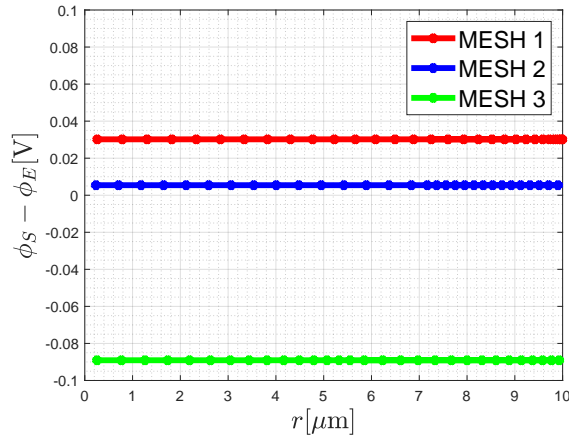
Figure 5.4: Overpotential distribution along the radial coordinate of the particle at the end of 3600 s charge for given meshes. A more negative potential difference $\phi_S - \phi_E$ enhances the overpotential η in each reaction. This results in an exponential increase in the active particle reaching full capacity but also influences the unwanted side reactions.
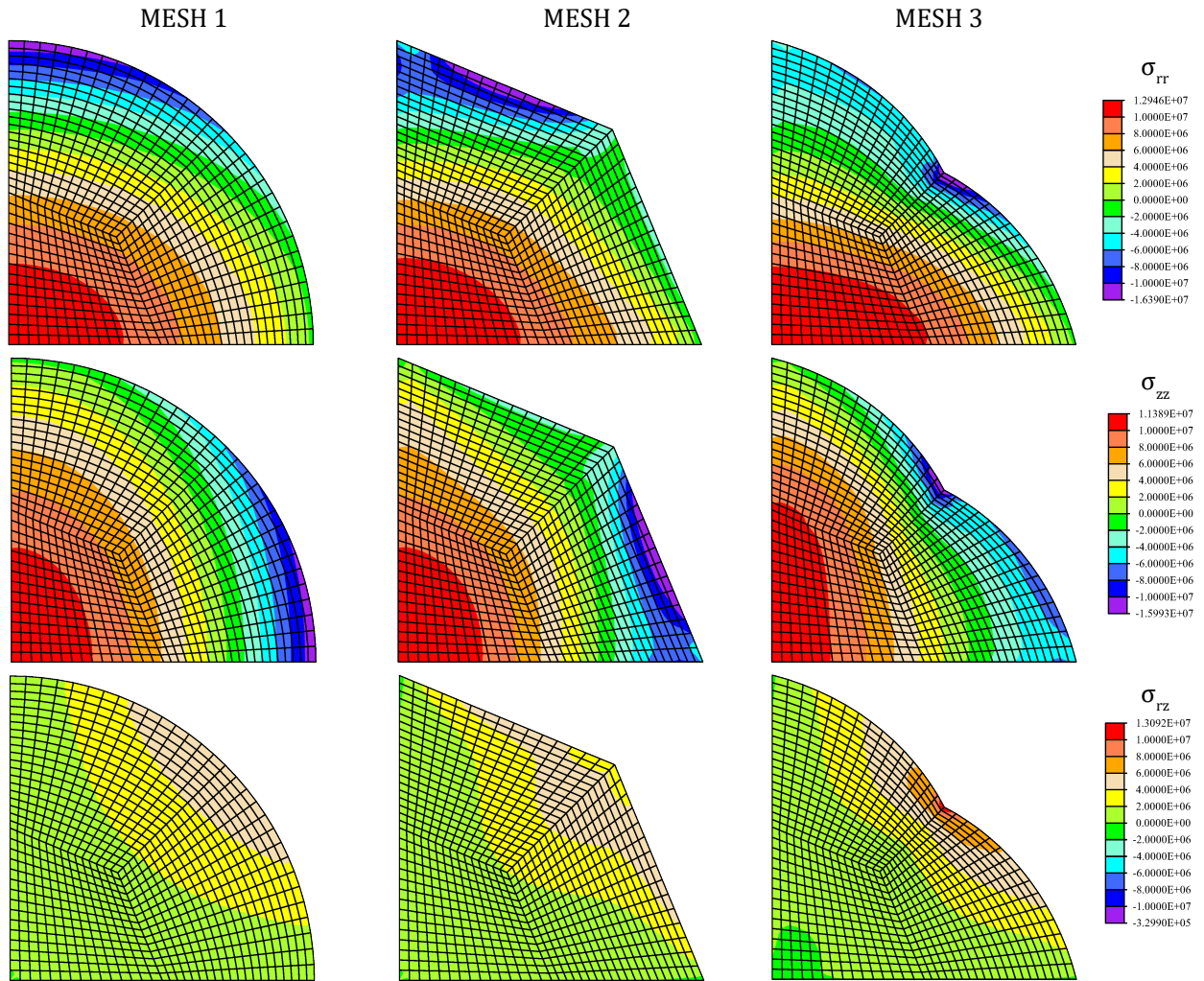
Figure 5.5: Stress distributions for $\{\sigma_{rr}, \sigma_{zz}, \sigma_{rz}\}$ all in units of Pascals [Pa].

Additionally, we can easily change the particle size to $R_1 = 15$ and $R_2 = 3$ μm. The particle size is 50% larger corresponding to a tremendous 337.5% increase in theoretical lithium storage capacity. Figure 5.6 illustrates the same fluctuation in σ_{VM} as well as a slight increase in film thickness for MESH 2 and 3. The only difference is the magnitude of total film thickness and stress is proportionally greater in this case as compared to the results above. As expected, σ_{VM} has increased by 50% from the case above. It is interesting to see that variance in lithium plating is much less significant. We attribute this to the ability of the active particle to store more lithium ions. Thus, the particle does not reach near its maximum concentration c_{max} resulting in similar potential difference distributions $\phi_S - \phi_E$ between the three meshes; see Figure 5.7.
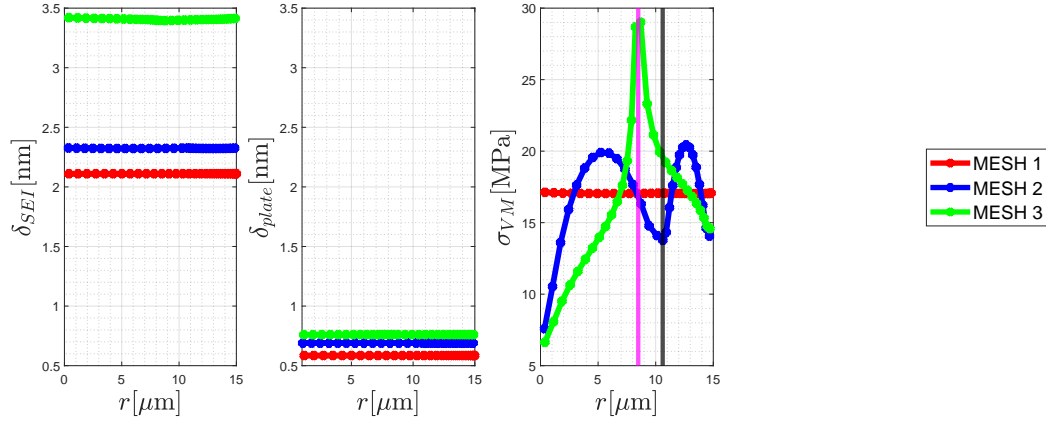
Figure 5.6: This figure demonstrates the change in particle size from $R_1 = 10\,\mu$m and $R_2 = 2$ μm to $R_1 = 15\,\mu$m and $R_2 = 3$ μm. Now the geometric imperfection in MESH 2 is located at $10.607\,\mu$m shown as the vertical black line, and the imperfection for MESH 3 is located at $8.485\,\mu$m shown as the vertical purple line.
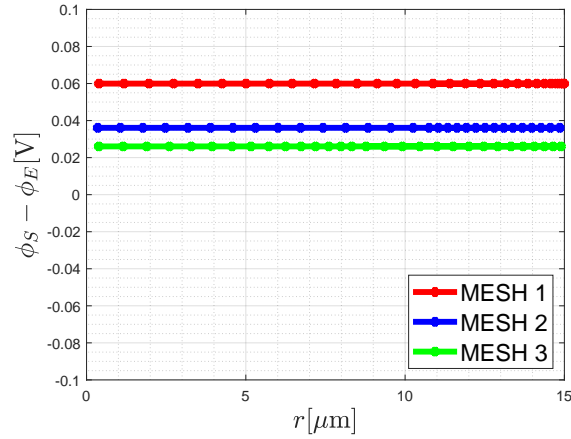
Figure 5.7: The potential difference $\phi_S - \phi_E$ for $R_1 = 15\,\mu$m and $R_2 = 3$ μm.

5.2 Cyclic Aging

We return back to the original mesh dimensions of $R_1 = 10\,\mu$m and $R_2 = 2$ μm. The simulation boundary conditions in this section will attempt to reproduce charging and discharging scenarios specifically applied to a single particle. At the outer surface of the electrolyte, $\sqrt{z^2 + r^2} = R_1 + R_2$, we will either positively or negatively apply a current density of magnitude $0.5\,\text{A/m}^2$ and a corresponding ionic flux of magnitude of $5.1821 \times 10^{-6}\,\text{mol/m}^2$s. One

can visualize this in Figure 5.8, where one "cycle" is either a positively applied current period or a negatively applied current period. Each simulation period lasts for 7200 s. Running the
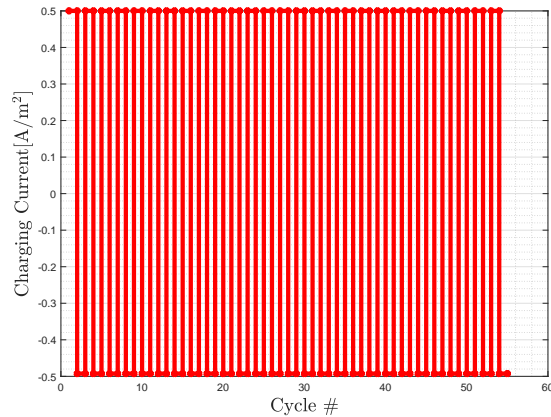
Figure 5.8: Applied charging and discharging current densities.

finite element model for 55 "cycles", we see an expected square root behavior for SEI growth and a parabolic transient profile for lithium plating in MESH 1 and MESH 2. This is similar to the linear to nonlinear capacity fading profile in Yang et al. (2017). Their experimental and computational analysis show SEI growth to be more dominant in the initial age of a battery cell, and then lithium plating becomes the dominant aging mechanism due to its exponential growth. Interestingly, we do not see this behavior for MESH 3, as the geometrical defect causes very linear film growth for the SEI and Li(s). Note that these thickness values δ_{SEI}, δ_{plate}, and potential difference values $\phi_S - \phi_E$ presented for each cycle number in Figure 5.9 are the average surface values over the radial position r of the particle. For each average surface value, δ_{SEI}, δ_{plate}, and $\phi_S - \phi_E$ was summed over all radial positions r and then divided by the number of data points sampled. The total film growth is greatest in MESH 3, as the SEI film grows exceptionally high. This would present impedance problems in a full model, where a cathode material is appropriately considered. We can see from the pseudo overpotential $\phi_S - \phi_E$ that lithium deposition occurs least in MESH 3 due to exhibiting the most stable potential profile as cycles increase. Rather than exhibiting an increase in potential fluctuations, as shown for MESH 1 and MESH 2, the overpotential actually decreases with time and seems to reach an asymptotic limit. Given the smaller charging and discharging rate on the particle, $\phi_S - \phi_E$ is always greater than 0.0 V (i.e. Li(s) equilibrium potential). This contrasts the scenario presented in the section above for a much higher applied current of $1.25 \, \text{A/m}^2$. The ability for available surface lithium ions to more rapidly intercalate into the particle results in a more stable surface potential. The minor geometrical defect helps the particle achieve its maximum concentration quicker, as shown in Figure 5.2. Residual SEI growth is inevitable, but is mitigated by having $\phi_S - \phi_E < U_{SEI}$, which is the case for all three meshes and for all cycle numbers.
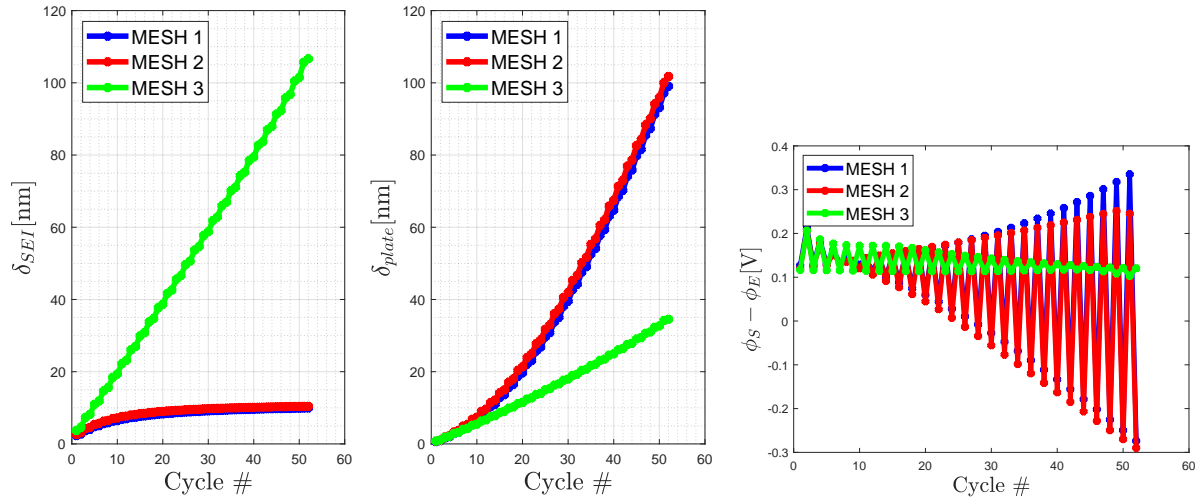
Figure 5.9: Film growth and overpotential difference given $\beta = 0.0$.

One mechanism for further SEI growth is the possibility of deposited lithium reacting with free electrons and the electrolyte solvent on the particle's surface. Consequently, these species can react to form the SEI compound. This is mathematically illustrated in Equations (2.81) and (2.82), where β is the fraction of plating that converts to the SEI. We can artificially set β to an arbitrary value in the simulation model. Figure 5.10 shows the stark contrast in δ_{SEI} and δ_{plate} given $\beta = 0.25$. The pseudo overpotential is very similar and almost identical for the case $\beta = 0.0$, however not only is δ_{plate} growing exponentially (or parabolically) with time, but also δ_{SEI} grows in the same fashion for MESH 1 and MESH 2. Since the surface overpotential inevitably becomes less than 0.0 V for these two meshes, plating will continue to occur regardless the value of β, and the conversion to SEI formation results in exponential growth for the SEI film layer. MESH 3 still exhibits very similar linear behavior given $\beta = 0.0$, which shows the efficacy of maintaining proper potential profiles within a battery cell to prevent aging.
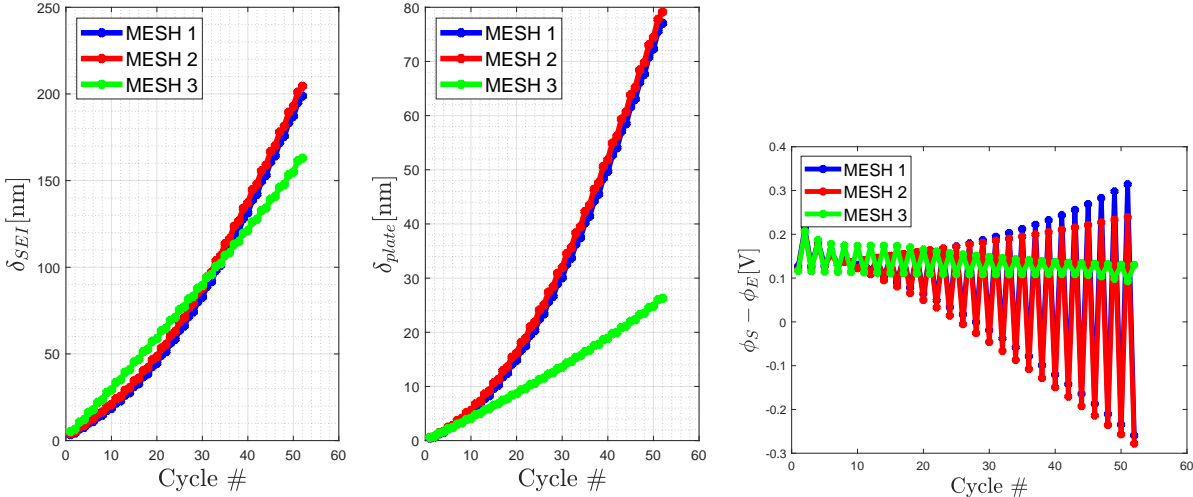
Figure 5.10: Film growth and overpotential difference given $\beta = 0.25$.

Chapter 6

Global Sensitivity Analysis

This chapter will conclude the results portion of the dissertation. We will perform a global sensitivity analysis on our finite element model through the use of Sobol indices in Sobol' (2001). Sobol indices is a variance based technique and are novel in that the nonlinear interactions of input model parameters can be measured in the sensitivity indices. We will study the effect of perturbations in the mechanical and electrochemical inputs in our set of user elements on: (1) discharging capacity density, (2) charging terminal voltage, (3) maximum temperature, and (4) average particle von Mises stress.

6.1 Sobol Indices

As with any simulation software, the output greatly depends on the model assumptions and input properties. Sensitivity measures give key insight into which factors play the most crucial roles. They also verify the model's validity. Local sensitivity analysis involves the use of functional gradients or partial differentiation of an objective function (see Ch.4 in Cacuci (2003)). Local methods not only allow the user to scale the importance of parameters but also visualize the direction they have on the output. As the name suggests, local methods analyze the perturbation of the solution about incremental changes in specific reference values. On the other hand, global sensitivity analysis also allows the user to identify important or non-influential parameters, while not necessarily needing the use of analytical or numerical differentiation as shown in Saltelli et al. (2004) Ch. 2. This yields ease of implementation but does not give a definite answer of whether the model perturbation is a positive or negative consequence. Typically, these techniques approximate variances in the objective function.

Various research is currently available for studying battery performance and optimization. Reddy et al. (2019) used the P2D model with least squares regression techniques to determine model input parameters from voltage data. Similarly, Park et al. (2018) combined a nonlinear least squares algorithm in the context of sensitivity analysis to determine an accurate set of input parameters and their individual contributions to the output data. Both studies determined that the size of the electrode particle radius and the active particle diffusivities are

the most critical parameters. They noted that the electrolyte transference number and active particle electrical conductivities are the least important. Golmon, Maute, and Dunn (2012) extended Newman's porous electrode model with mechanical deformations in a multiscale setting. The finite element method is used at both scales in conjunction with porous electrode theory to determine continuous concentration, potential, and displacement fields. Adjoint sensitivity analysis was then used to determine the optimal battery layout for maximum discharge capacity while limiting peak stress levels. Lin et al. (2018) also utilized a multiscale approach and determined that the electrode size and pore structure is the most sensitive input parameter for discharge capacity and thermal behavior. Sensitivity analysis methods with Newman's porous electrode theory have also been used in Jin et al. (2017), Constantine and Doostan (2017), Zhang et al. (2013), Pozzi et al. (2019), and Hadigol, Maute, and Doostan (2015) among others. Edouard et al. (2016) extended Newman's porous model to include battery aging due to SEI growth. They also found that the pore geometry and size within the electrode are some of the most significant parameters. Laresgoiti et al. (2015) studied the mechanical stress generated during cycling in the active particle and the solid-electrolyte interphase (SEI) layer. Their results are interesting as the highest sensitivity measures for the active particle are not necessarily the same for that of the SEI layer.

Most current papers on lithium ion batteries only consider the electrochemical behavior of lithium ion cells. However, Safari et al. (2009) demonstrates the loss of structural integrity of the electrodes contributes the most to destructive battery aging mechanisms. High mechanical stresses deteriorate the bonding of active particles and can even lead to fracture. This causes an excessive amount of unwanted side reactions occurring at newly exposed interfaces between the solid particles and the surrounding electrolyte. The expansion and contraction of electrodes is cyclic and the main shortcoming of higher capacity electrodes. Additionally, high temperatures yield poorer performance through similar aging mechanisms. This diminishes the usability of the battery's capacity. The design of battery cells is therefore very complicated as the electrochemistry is coupled with mechanical and thermal effects. Unfortunately, experimental techniques are not advanced enough to simultaneously measure all these phenomena during charging/discharging. Computer models can provide extremely accurate predictions but need proper assumptions and realistic input variables. Sensitivity measures provide a valuable tool in determining which variables are most important from a computational accuracy perspective.

We seek to reproduce some of the published optimization analyses and provide a more detailed illustration with our finite element battery model. This chapter will focus on utilizing "Sobol Indices" (Sobol', 2001), which is a variance based technique of determining the linear and nonlinear interaction between the model properties. The method of Sobol' (2001) assumes that the output model (e.g. discharge capacity, temperature, etc.) can be described by an integrable function $y = f(\mathbf{x})$, where the input variables are $\mathbf{x} = (x_1, ..., x_n)$. Given the desired solution $y^* = f(\mathbf{x}^*)$, local sensitivity measures are traditionally measured by the partial derivative of the solution with respect to an input, i.e. $(\partial y / \partial x_k)_{\mathbf{x}=\mathbf{x}^*}$.

Global sensitivity measures are unique in that the solution $\mathbf{x}^*$ is not needed and only considers the model $f(\mathbf{x})$. This is done by the decomposition of the function $f(\mathbf{x})$ into a

series of summands with increasing dimensionality

$$f(\mathbf{x}) = f_0 + \sum_i f_i(x_i) + \sum_{i<j} f_{ij}(x_i, x_j) + \cdots + f_{12\cdots n}(x_1, x_2, \ldots, x_n). \tag{6.1}$$

For Equation (6.1) to hold, f_0 must be a constant, and the integral of every summand over any of its own variables must be zero,

$$\int_0^1 f_{i_1 \cdots i_s}(x_{i_1}, \ldots, x_{i_s})\, dx_k = 0 \qquad \text{for} \qquad k = i_1, \ldots, i_s. \tag{6.2}$$

The functions $f_{ij\cdots k}(x_i, x_j, ..., x_k)$ are derived from conditional expectations. The mean and first order functions are obtained as

$$f_0 = E(y), \tag{6.3}$$
$$f_i = E_{\mathbf{x}_{-i}}(y|x_i) - E(y), \tag{6.4}$$

where $\mathbf{x}_{-i}$ denotes the space of all variables not including x_i. The total variance and the first order partial variances of a function are defined as

$$V(y) = \int_{\mathbf{x}} f(\mathbf{x})^2 d\mathbf{x} - f_0^2, \tag{6.5}$$
$$V_i = V(f_i(x_i)) = V_{x_i}\left[E_{\mathbf{x}_{-i}}(y|x_i) \right]. \tag{6.6}$$

We are neglecting definitions of higher order terms as we will not be incorporating them. Saltelli et al. (2010) provide a more extensive formulation of higher order variance definitions. The first order Sobol index is then defined as

$$S_i = \frac{V_{x_i}\left[E_{\mathbf{x}_{-i}}(y|x_i) \right]}{V(y)}, \tag{6.7}$$

with the total effect index being

$$S_{Ti} = \frac{E_{x_{-i}}\left[V_{\mathbf{x}_i}(y|\mathbf{x}_{-i})) \right]}{V(y)} = 1 - \frac{V_{x_{-i}}\left[E_{\mathbf{x}_i}(y|\mathbf{x}_{-i}) \right]}{V(y)}. \tag{6.8}$$

S_i measures the first order effect of x_i on the model's output, while S_{Ti} measures the total effect the parameter has on the model. S_{Ti} includes the nonlinear interactions that variables can have with one another. If $S_i = S_{Ti} = 0$, then $f(\mathbf{x})$ does not depend on x_i, and if $S_i = S_{Ti} = 1$ then $f(\mathbf{x})$ depends only on x_i. By construction, $S_{Ti} \geq S_i$ and $\sum S_i \leq 1$, while $\sum S_{Ti} \geq 1$. This is intuitive as the total effect of a variable should always be at least equal to its first order effect. The greater in magnitude these indices are, the more sensitive the function is to the parameter. It provides a useful identification which parameters should be studied further and which parameters are insignificant.

Saltelli et al. (2010) provides an efficient way to estimate these integrals via the Monte Carlo method. To compute S_i and S_{Ti}, latin hypercube sampling (LHS) (Ye, 1998) generates two sets of sample matrices $\mathbf{A}$ and $\mathbf{B}$, each of dimension $N \times p$ with p being the size of the input variables. This yields N rows of a p dimensional input vector $(x_1, x_2, ..., x_p)$ for the function $f(\mathbf{x})$. From these matrices, we can create a third matrix $\mathbf{A}_{\mathbf{B}}^i$, such that the i-th column of $\mathbf{A}_{\mathbf{B}}^i$ is the same as the i-th column of $\mathbf{B}$. The other columns of $\mathbf{A}_{\mathbf{B}}^i$ are the same as those of $\mathbf{A}$. Defining N as the number of sampling points in the Monte Carlo method, the integrals are approximated as

$$f_0 \quad = \quad \frac{1}{N} \sum_{k=1}^{N} f(\mathbf{A}_k) \,, \tag{6.9}$$

$$V(y) \quad = \quad \frac{1}{N} \sum_{k=1}^{N} (f(\mathbf{A}_k))^2 - \left(\frac{1}{N} \sum_{k=1}^{N} f(\mathbf{A}_k) \right)^2 \,, \tag{6.10}$$

$$S_i \quad = \quad \frac{1}{N} \sum_{k=1}^{N} f(\mathbf{B})_k \left(f(\mathbf{A}_{\mathbf{B}}^i)_k - f(\mathbf{A})_k \right) \,, \tag{6.11}$$

$$S_{Ti} \quad = \quad \frac{1}{2N} \sum_{k=1}^{N} \left(f(\mathbf{A})_k - f(\mathbf{A}_{\mathbf{B}}^i)_k \right)^2 \,. \tag{6.12}$$

In the above expressions, the functions $f(\mathbf{A}_k)$, $f(\mathbf{B})_k$, and $f(\mathbf{A}_{\mathbf{B}}^i)_k$ denote a corresponding output of the FEM simulation, which are evaluated with the corresponding k^{th} row of matrices $\mathbf{A}$, $\mathbf{B}$, or $\mathbf{A}_{\mathbf{B}}^i$, respectively. A consensus has not been made in the literature as to which first order approximations are best. Jansen (1999) and Owen (2013) provide other estimations for first order indices and show that smaller indices are harder to accurately represent. Generally, as N increases the better the estimation is. In the following sections, we choose to work with the total effect index S_{Ti} as it encapsulates the implicit nonlinearity in some of the parameters and provides a more consistent estimate.

The remaining sections in this chapter focus on using our FEM model in conjunction with Sobol indices to study the importance of key material parameters. Our output function will consist of four different measurements: (1) discharge battery capacity, (2) charging terminal voltage, (3) maximum temperature in an adiabatic cell, and (4) average von Mises stress in the active particles. Battery capacity, terminal voltage, and temperature are commonly studied in the literature, as they are easily able to be experimentally verified. However, microscale mechanical stresses are very difficult to measure. Safari et al. (2009) experimentally measured that about 73% of total capacity loss after 800 cycles is due to structural degradation of active material. This is an outstanding result as most capacity fading estimates neglect any mechanics and attribute the capacity loss solely due to side reactions, such as SEI formation or lithium plating. This was also shown in the section above on geometrical effects on reaction rates and stress concentrations. Our model does not include any fracture/fatigue mechanics, stress induced effects on lithium diffusion, or stress dependent reaction rates, but

it is able to give us a detailed illustration of what material properties yield the highest effect on stress concentrations. We believe our finite element model can be a great predictor for which properties should be studied further and optimized within the cell. The simulation model we use is very idealized and similar to that used in Wang and Garikipati (2018). They studied finite deformation effects on electrode porosity. We simplify the geometry as we are not trying to predict the location and/or magnitude of the highest stress concentrations.

6.2   FEM Simulation Description

The mesh is shown in Figure 6.1 with the anode active particles in red, the electrolyte separator in blue, and the cathode active particles in light blue. The green and yellow elements signify the liquid electrolyte surrounding the active particles in each electrode. The dimensions for the cell height, anode length, separator length, and cathode lengths are $W = 14\,\mu m, L_A = 88.85\,\mu m, L_S = 16\,\mu m, L_C = 88.85\,\mu m$, respectively. The active particle radius is $12\,\mu m$, as the cell height includes a fraction of the electrolyte elements. We use axisymmetric elements, which accounts for a 2π rotation about the azimuth axis. The mesh intends to symbolize a small sliver of a true battery cell at this length scale. Realistically the height W would be orders of magnitude greater and these thin cells would be spirally wound for higher capacity. The boundary conditions for each simulation are shown below with I_{app} being equal to the applied discharge or charge current.
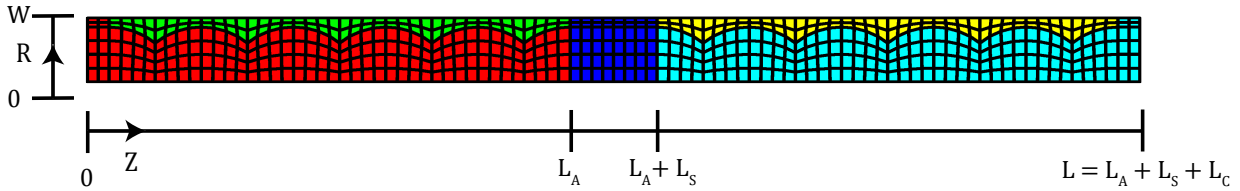
Figure 6.1: Finite element mesh depicting the anode and cathode active particles in red and light blue, respectively. The separator is shown in blue with the remaining green and yellow elements symbolizing the electrolyte surrounding the electrode elements. The mesh is idealized to depict a sliver of a full cell with a given porosity.

$R = 0$	$R = W$	$Z = 0$	$Z = L_A + L_S + L_C$
$u_R = 0$	$\boldsymbol{\sigma} \cdot \mathbf{n} = 0$	$u_Z = 0$	$u_Z = 0$
$\mathbf{j} \cdot \mathbf{n} = 0$	$\mathbf{j} \cdot \mathbf{n} = 0$	$\mathbf{j} \cdot \mathbf{n} = 0$	$\mathbf{j} \cdot \mathbf{n} = 0$
$\mathbf{i} \cdot \mathbf{n} = 0$	$\mathbf{i} \cdot \mathbf{n} = 0$	$\phi = 0$	$\mathbf{i} \cdot \mathbf{n} = I_{app}$
$\mathbf{q} \cdot \mathbf{n} = 0$	$\mathbf{q} \cdot \mathbf{n} = 0$	$\mathbf{q} \cdot \mathbf{n} = 0$	$\mathbf{q} \cdot \mathbf{n} = 0$

One utility of porous electrode theory is that the particle radius, electrode porosity, and tortuosity can be easily changed in a simulation setting. This is not the case for finite ele-

ment discretizations. This would require re-meshing and instilling new boundary conditions at every Monte Carlo iteration, which is too cumbersome for our work. It has already been verified that particle radius and porosity are always some of the most sensitive parameters. Smaller radii yield better performance in general, and there is an optimal porosity value to efficiently allow lithium ions to flow between electrodes during use. We fix the mesh geometry and study the other material properties that are used in the constitutive equations. Additionally, we assume that the anode is lithium graphite (LiC_6) and the cathode is lithium nickel manganese cobalt oxide (NMC). Their respective open circuit voltages used in the Butler-Volmer interface elements are shown again below in terms of the normalized concentration $\bar{c} = c/c_{max}$ and temperature T:

$$U_0^N(\bar{c}) = 0.266 + 0.555 \exp\left(-178.97\bar{c}\right) - 0.012 \tanh\left(\frac{\bar{c} - 0.557}{0.028}\right)$$

$$- 0.0117 \tanh\left(\frac{\bar{c} - 0.239}{0.049}\right) - 0.0129 \tanh\left(\frac{\bar{c} - 0.175}{0.035}\right)$$

$$- 0.05 \tanh\left(\frac{\bar{c} - 0.99}{0.0245}\right) - 0.035\bar{c} - 0.012 \tanh\left(\frac{\bar{c} - 0.13}{0.02}\right) \tag{6.13}$$

$$- 0.152 \tanh\left(\frac{\bar{c} - 0.03}{0.023}\right),$$

$$U_0^P(\bar{c}) = \left(-0.0923 - 7.82\bar{c} + 50.07\bar{c}^2 - 122.28\bar{c}^3 + 82.98\bar{c}^4 + 140.29\bar{c}^5\right.$$

$$\left. - 374.73\bar{c}^6 + 403.25\bar{c}^7 - 221.19\bar{c}^8 + 49.33\bar{c}^9\right) \bigg/ \left(-0.02 - 1.9\bar{c}\right. \tag{6.14}$$

$$\left. + 11.73\bar{c}^2 - 28.78\bar{c}^3 + 27.54\bar{c}^4 - 8.63\bar{c}^5\right).$$

Equation (6.13) uses $c_{max} = 25,000 \, \text{mol/m}^3$ and Equation (6.14) uses $c_{max} = 30,000 \, \text{mol/m}^3$. The superscripts N and P signify negative and positive electrodes, respectively. Figure 3.21 illustrates these functions, which are taken from Wang et al. (2018) along with $\partial U_0/\partial T$ being given in Equation (3.32) for both the anode and cathode materials. In the remaining sections below, we will assume densities for anode, cathode, and electrolyte to be 2500, 2500, and 1100 kg/m³, respectively. The densities and maximum concentrations are not varied in our work.

6.3   Discharge Capacity and Terminal Voltage Results

This section will illustrate the results of the sensitivity measures calculated on the discharge capacity density and charging terminal voltage in response to the model inputs. Both are measures of battery capacity, as the discharge capacity is determined by the time integration

of the amount of current extracted from the cell,

$$Q = \int_0^T I(t)\, dt\,.$$

The terminal voltage is easily measured from the voltage difference between the cathode and anode potentials at the end of the charging period,

$$V = \phi(z = L) - \phi(z = 0)\,.$$

The simulation battery current is measured from the average current magnitude $|\mathbf{i}|$ from the 12 active material elements at $z = L$. We use the midpoint method to integrate this function in time. Since our model constitutive equations do not have mechanical deformations influencing the flux or current relations, we will not vary any mechanical parameters for this section. It will purely focus on the electrochemical behavior. The parameters varied and their ranges are shown in Table 6.1. The discharge/charge current applied was $41\,\mathrm{A/m^2}$, and the simulation ran for 2640 seconds. The magnitude of this current density is approximately a 1C rate current density. The initial lithium concentrations in the anode and cathode during discharge were $23750\,\mathrm{mol/m^3}$ and $1500\,\mathrm{mol/m^3}$, respectively. The initial concentrations during the charging period were $1250\,\mathrm{mol/m^3}$ and $28500\,\mathrm{mol/m^3}$, respectively. These conditions symbolize a fully charged cell before the discharge period and a fully depleted cell before charging. These initial conditions will be used in future sections as well. We chose to only show the total order Sobol index for brevity, as the first order Sobol index was almost identical in every analysis. This ascertains that the parameter coupling is primarily first order in our model.

First, we varied the active particle and electrolyte electrochemical and thermal properties to see which are of the highest importance. Then, we will sample the subsection of properties with the highest Sobol index values with the reaction rate constants chosen as $k_R = 5 \times 10^{-12}$ and $k_R = 1 \times 10^{-11}$ for the anode and cathode particles, respectively, with units of $[\mathrm{m^{5/2}/s\sqrt{mol}}]$. We originally neglect studying the variance of the reaction rate constants in the Butler-Volmer expression, since these are already well noted to be a significant factor in capacity and terminal voltage.

Material Parameter	Units	Range	$S_{Ti,discharge}$	$S_{Ti,charge}$
(A) Diffusivity	m^2/s	$4 \times 10^{-13} - 6 \times 10^{-13}$	0.0	0.0016
(A) Electrical Conductivity	S/m	$145 - 155$	0.0	0.0
(A) Heat Conductivity	W/m $\cdot$ K	$0.8 - 1.2$	0.0	0.0
(A) Specific Heat	J/kg $\cdot$ K	$675 - 725$	0.0005	0.0089
(E) Diffusivity	m^2/s	$2 \times 10^{-10} - 5 \times 10^{-10}$	0.0626	0.0906
(E) Electrical Conductivity	S/m	$0.5 - 1.5$	0.001	0.0024
(E) Transference #	-	$0.3 - 0.4$	0.0	0.0
(E) Thermodynamic Factor	-	$0.35 - 0.45$	0.0	0.0
(E) Heat Conductivity	W/m $\cdot$ K	$0.05 - 0.15$	0.0	0.0
(E) Specific Heat	J/kg $\cdot$ K	$1700 - 1900$	0.0006	0.0094
(C) Diffusivity	m^2/s	$4 \times 10^{-13} - 6 \times 10^{-13}$	0.7818	0.0052
(C) Electrical Conductivity	S/m	$45 - 55$	0.0	0.0
(C) Heat Conductivity	W/m $\cdot$ K	$0.8 - 1.2$	0.0	0.0
(C) Specific Heat	J/kg $\cdot$ K	$675 - 725$	0.0005	0.0082
Initial Temperature	K	$283.1 - 312.9$	0.1634	0.9022

Table 6.1: Input ranges for the material parameters studied for discharge capacity and charging terminal voltage. (A), (E), and (C) symbolize the anode, electrolyte, and cathode, respectively. In every Monte Carlo iteration, we fix the reaction constants [m$^{5/2}$/s$\sqrt{\text{mol}}$] for the anode and cathode to be $k_R = 5 \times 10^{-12}$ and $k_R = 1 \times 10^{-11}$, respectively.

Figure 6.2 shows the Sobol indices for discharging capacity and charging terminal voltage. One can see that most of the parameters used in the model have very little effect in the uncertainty outcome for discharge capacity. In discharging, the mean f_0 and total variance $V(y)$ calculated from Equations (6.9) and (6.10) are 3.0791 mAh/cm^2 and 1.17×10^{-7} (mAh/cm^2)^2, respectively. In charging, the mean is 4.1866 V with a standard deviation $\sqrt{V(y)}$ of 0.011 V. It is surprising that S_{Ti} for the diffusion coefficient of lithium in the anode is zero for discharging and a very minor uncertainty prediction in charging. It is also surprising that the only electrochemical properties causing any significant variance are the diffusion coefficients of the cathode and electrolyte. Intuitively, it seems that the electrical conductivity could play a major role. Recall, the ionic flux is given by

$$\mathbf{j} = -D\nabla c - \frac{DzF}{RT} c \nabla \phi \,.$$

The conductivity drives the magnitude of the potential gradient $\nabla \phi$, which is then the primary driving force for the migration of ions. The multiplication of D in the relation for $\mathbf{j}$ seems to solely mitigate the impact of their migration.

It is also well seen in the literature that non-optimal temperature conditions hinder battery performance. Low temperatures impede reaction rates and the migration of lithium

ions. Slightly higher temperatures actually help performance by doing the opposite. However, an excessively large temperature also results in negative consequences. The adhesive glue of the electrode can deteriorate or the rate of unwanted side reactions can increase. This was not considered in our work though. As a result of the temperature being so significant in battery charging, the specific heats also play a minor role. The specific heat controls the amount of heat the material absorbs and consequently how much T varies in time. The thermal conductivity λ has zero indices for all three materials. This is a result of a homogeneous temperature distribution within the cell. At the length scale we simulate, T disperses much quicker than the concentration c and remains homogeneous at each time step. Due to the large current magnitude applied, our results can indicate that thermal changes are very imperative for battery simulation modeling, especially during charging scenarios.
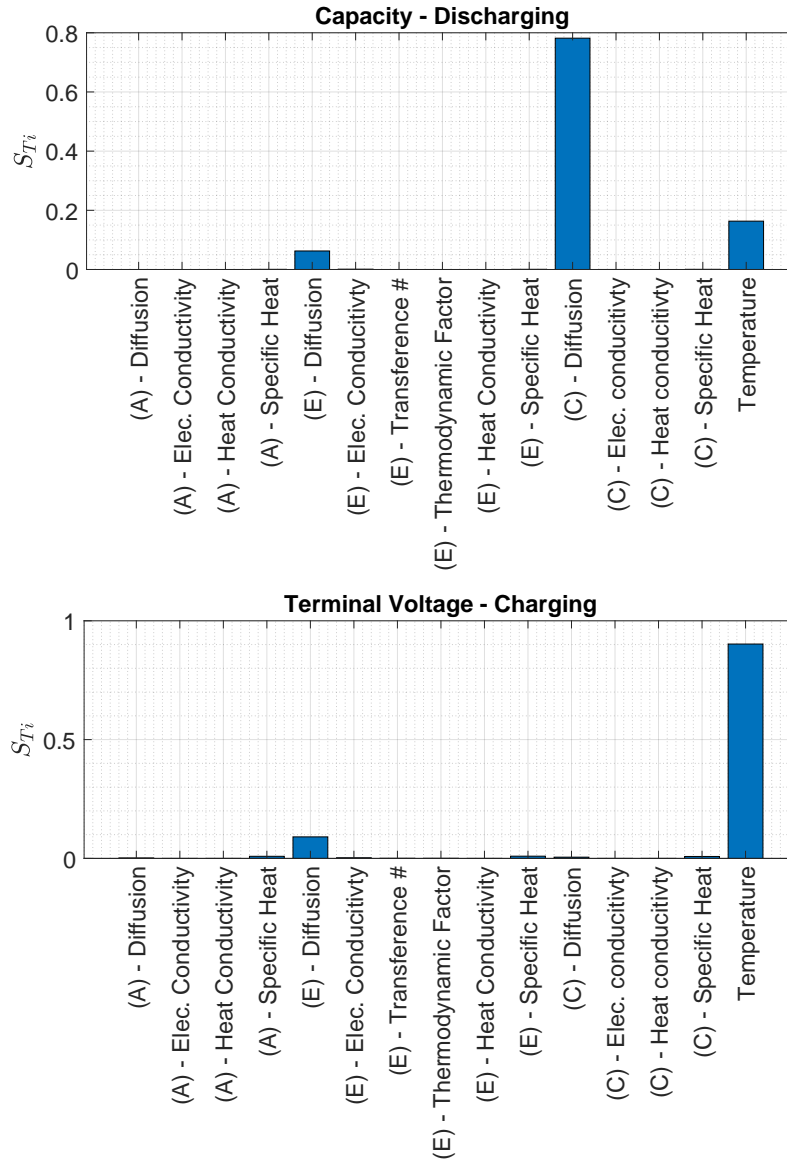
Figure 6.2: For both cases the FEM model used a current density of $41\mathrm{A/m^2}$ for 2640 seconds (≈ 0.75 hours). The current magnitude is negative during discharging and positive during charging. (A), (E), and (C) symbolize the anode, electrolyte, and cathode, respectively.

Next, we will consider the reaction rates of the anode and cathode, while neglecting some of the properties that exhibit no effect in the previous analysis. The properties varied are shown in Table 6.2 with the Sobol indices illustrated in Figure 6.3. The initial conditions for discharging/charging are the same as in the previous case, but we lowered the applied current to $20\,\mathrm{A/m^2}$ (≈ 0.5 C rate) and ran the FEM model for 5280 seconds (≈ 1.5 hours). Equation (6.9) yields a discharge capacity average of $f_0 = 3.1395\,\mathrm{mAh/cm^2}$ and $\sqrt{V(y)} =$

$0.0018 \, \text{mAh/cm}^2$. The new average terminal voltage is 3.9674 V with standard deviation of 0.0687 V. As expected, the smaller current magnitude, as compared to the previous analysis, produces a higher discharge capacity density while producing a smaller terminal voltage on average.

Material Parameter	Units	Range	$S_{Ti,discharge}$	$S_{Ti,charge}$
(A) Diffusivity	m^2/s	$1 \times 10^{-13} - 7 \times 10^{-13}$	0.0	0.0006
(A) Specific Heat	$\text{J/kg} \cdot \text{K}$	$600 - 900$	0.0	0.0002
(E) Diffusivity	m^2/s	$7 \times 10^{-11} - 5 \times 10^{-10}$	0.0007	0.0030
(E) Conductivity	S/m	$0.5 - 1.5$	0.0005	0.0
(E) Specific Heat	$\text{J/kg} \cdot \text{K}$	$1500 - 2000$	0.0	0.0011
(C) Diffusivity	m^2/s	$1 \times 10^{-13} - 7 \times 10^{-13}$	0.6357	0.0019
(C) Specific Heat	$\text{J/kg} \cdot \text{K}$	$500 - 1000$	0.0001	0.0012
(A) Reaction Rate	$\text{m}^{5/2}/\sqrt{\text{mol}} \cdot s$	$1 \times 10^{-12} - 6 \times 10^{-11}$	0.0018	0.5290
(C) Reaction Rate	$\text{m}^{5/2}/\sqrt{\text{mol}} \cdot s$	$1 \times 10^{-12} - 6 \times 10^{-11}$	0.3511	0.4564
Initial Temperature	K	$283.1 - 312.9$	0.0029	0.0041

Table 6.2: Input ranges for the material parameters studied in the second analysis of discharge capacity and charging terminal voltage. (A), (E), and (C) symbolize the anode, electrolyte, and cathode, respectively. The remaining electrochemical parameters were chosen as the median in the sampling ranges from Table 6.1.

Since we are using the Monte Carlo method to evaluate the Sobol indices, the magnitude of the indices are not perfectly accurate. In the discharging perdiod, we do obtain good qualitative information, as we can still see D plays a crucial role for ion transport and output current in the cathode. We determine again that the cathode's diffusivity is extremely important in discharge capacity. The cathode reaction rate has shifted the sensitivity measures of the temperature and electrolyte diffusivity. The reaction rate k_R influences the magnitude of the amount of lithium ions entering and leaving the cathode active particles, which then dictates the amount of capacity one can extract from the battery cell.

Figure 6.4 illustrates the concentration field from the finite element model at the end of a discharge run. In both the anode and cathode, we see similar spatial distributions as lithium ions are moving from the anode to cathode. At the junctions of the separator (shown as dark blue in Figure 6.1) with the anode and cathode, we see that lithium is most depleted in the anode and is most saturated in the cathode. An estimate on the concentration gradient $\partial c/\partial z$ yields about a 3.2% higher gradient in the cathode than the anode. This could be the reason for the primary dependency of the cathode's diffusion in the sensitivity analysis.

In the charging period, the reaction rates for both electrodes exhibit the highest sensitivity. They almost completely outweigh the initial temperature's significance. Evidenced in the concentration figure below, the reaction rates have a direct dependence on the speed

of lithium ions entering and leaving both electrodes. Ions quickly migrate through the electrolyte, as its concentration is almost spatially uniform. The spatial distribution of the electrolyte concentration is highly dependent on D, which is why we see a small sensitivity measure S_{Ti} for this parameter.

Note that our model does not include any Arrhenius relations with temperature or concentration. Realistically, the reaction rates would fluctuate given fluctuations in temperature. The temperature affects the reaction rate through the open circuit potential

$$U_0(T) = U_0(T = 298\,\text{K}) + (T(t) - T_0)\frac{\partial U_0}{\partial T}\,,$$

which then is directly multiplied by the reaction rate k_R in the Butler-Volmer equation. This shows a clear indication for the almost unanimous dependence of the anode and cathode reaction rates on the simulation's variance during charging.
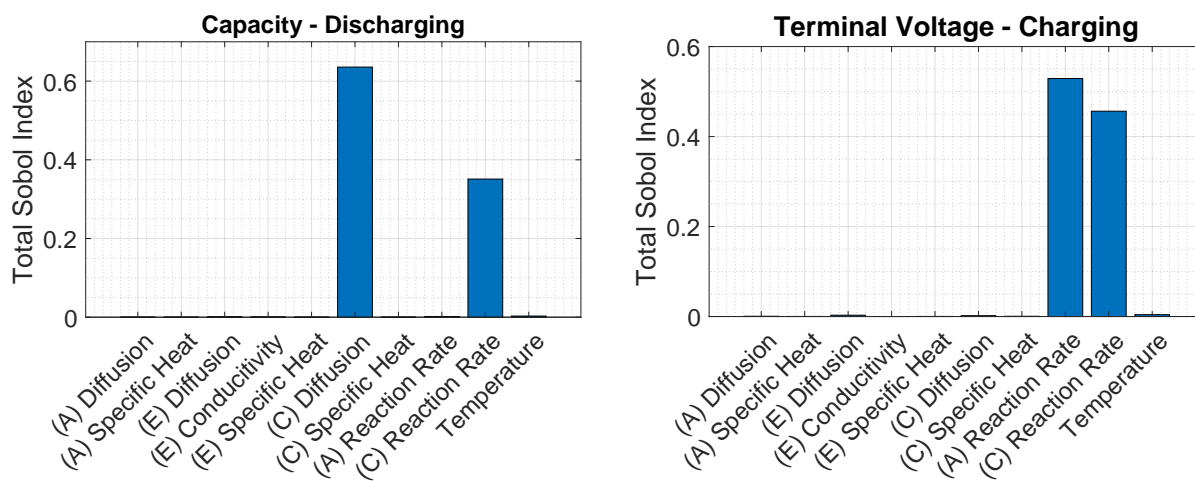
Figure 6.3: Total effect Sobol indices for discharge capacity and terminal voltage with new boundary conditions of 20A/m^2 being extracted/applied for 5280 seconds ($\approx$ 1.5 hours).
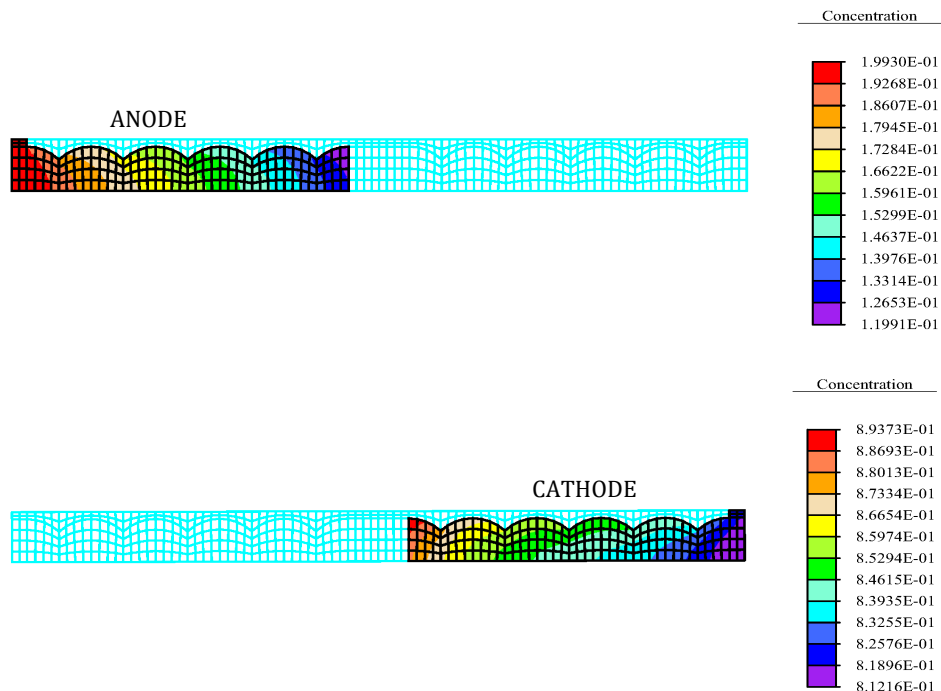
Figure 6.4: Normalized concentration distribution c/c_{ref} of lithium for the anode and cathode at the end of discharge.

6.4 Maximum Temperature Results

We now test the sensitivity of the electrochemical properties and the initial temperature on the maximum temperature obtained within any element in the cell. We add to Table 6.1 and include the reaction rates of the anode and cathode for this section's sensitivity analysis run. The parameters varied, the ranges, and the discharge/charge total Sobol indices are shown in Table 6.3. We ran the FEM simulation for the same boundary conditions in the previous case, except now we extract the maximum temperature in any element at the end of the discharge and charge states. For this specific adiabatic case, there is no difference between the charge and discharge analyzes. This makes complete sense as we apply the same magnitude of the electric current for the same duration for both cases. Energy conservation then requires that the total heat generated will be the same and we should reach the same final temperature given the same material properties. We choose to implement adiabatic boundary conditions along all edges of the mesh, because we are only simulating a small section of a full battery cell. Our mesh would realistically be surrounded by other cells and it seems reasonable that the heat generation is trapped within this specific microstructure. We note that some heat is escaped through convection at the edges $z = 0$ and $z = L$, but the sensitivity measures should still be very similar. For brevity, we only visualize the charging case in Figure 6.5.

Material Parameter	Units	Range	$S_{Ti,discharge}$	$S_{Ti,charge}$
(A) Diffusivity	m^2/s	$4 \times 10^{-13} - 6 \times 10^{-13}$	0.0	0.0
(A) Elec. Conductivity	S/m	$145 - 155$	0.0	0.0
(A) Heat Conductivity	W/m · K	$0.8 - 1.2$	0.0	0.0
(A) Specific Heat	J/kg · K	$675 - 725$	0.0016	0.0017
(E) Diffusivity	m^2/s	$2 \times 10^{-10} - 5 \times 10^{-10}$	0.0046	0.0047
(E) Elec. Conductivity	S/m	$0.5 - 1.5$	0.0015	0.0015
(E) Transference #	-	$0.3 - 0.4$	0.0	0.0
(E) Thermo. Factor	-	$0.35 - 0.45$	0.0	0.0
(E) Heat Conductivity	W/m · K	$0.05 - 0.15$	0.0	0.0
(E) Specific Heat	J/kg · K	$1700 - 1900$	0.0106	0.0111
(C) Diffusivity	m^2/s	$4 \times 10^{-13} - 6 \times 10^{-13}$	0.7818	0.0
(C) Elec. Conductivity	S/m	$45 - 55$	0.0	0.0
(C) Heat Conductivity	W/m · K	$0.8 - 1.2$	0.0	0.0
(C) Specific Heat	J/kg · K	$675 - 725$	0.0016	0.0017
(A) Reaction Rate	m$^{5/2}$/s$\sqrt{\text{mol}}$	$0.8 \times 10^{-11} - 2 \times 10^{-11}$	0.3749	0.3746
(C) Reaction Rate	m$^{5/2}$/s$\sqrt{\text{mol}}$	$0.8 \times 10^{-11} - 2 \times 10^{-11}$	0.3285	0.3386
Initial Temperature	K	$292.04 - 303.96$	0.2723	0.2718

Table 6.3: Input ranges for the material parameters studied on maximum temperature at the end of discharge and charging. (A), (E), and (C) symbolize the anode, electrolyte, and cathode, respectively. The range variance for each variable was chosen to provide a significant enough variance but not computationally require an excessive amount of Monte Carlo sample points N, where $N = 12,000$ in this analysis.

The mean final temperature for $N = 12,000$ Monte Carlo samples is $f_0 = 349.2\,\text{K}$ with standard deviation $\sqrt{V(y)} = 7.76\,\text{K}$. Interestingly, both reaction rates have the highest significance with the anode's rate slightly outweighing the cathode's rate. This occurs in the previous charging case for determining the terminal voltage. This correlation indicates that surface reactions are not only significant in the uncertainty outcome of charging capacity but also the final operating temperature of the battery cell.

The initial temperature T_0 displays the third largest sensitivity measure, which is a very reasonable result. It is intriguing to see that the specific heats C_p or thermal conductivities λ yield little to no sensitivity in the finite element model. We again postulate that due to the uniformity of the spatial temperature distribution in the mesh, λ plays no role in the corresponding ranges we used. This is evident in Figure 6.6 with every element displaying the same temperature at the corresponding times $t = 0$ and $t = 5280\,\text{s}$.
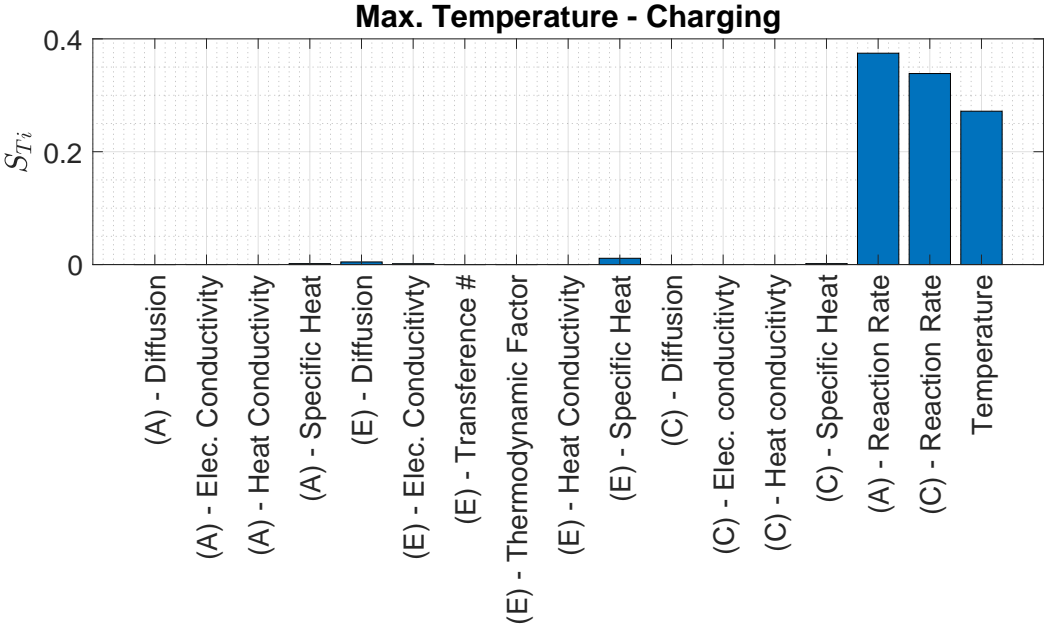
Figure 6.5: Given an adiabatic battery system, we determine the electrochemical sensitivity measures on the maximum temperature. The same boundary conditions again are a current density of $20\,\mathrm{A/m^2}$ applied for 5280 seconds.
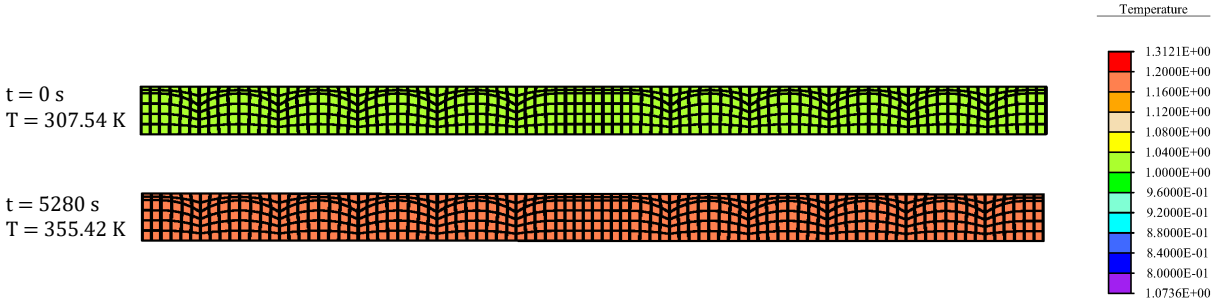
Figure 6.6: The parameters used in the model were sampled from the range given in Table 6.3. At both $t = 0$ s and $t = 5280$ s there is a homogeneous distribution. These temperature distributions indicate that the thermal conductivities λ have no impact on the the variance in the cell's maximum temperature.

6.5   Average Particle Stress Results

This final section calculates the Sobol indices for the average von Mises stress obtained in all of the anode and cathode active particles. The expression for the von Mises stress in cylindrical coordinates is shown in Equation (5.1). We determine sensitivity measures for the average particle stress in lieu of any maximum stress obtained, as the boundary conditions specifically for the mechanical degrees of freedom are approximate to realistic conditions. In addition, the true porosity distributions, particle sizes, and particle shapes are idealized and assumed to be symmetric for both the anode and cathode active materials. These idealizations would not give an accurate depiction of the true stress distribution or stress concentration locations in a realistic battery cell. However, the Sobol indices calculated in this section will give a clear indication of which material parameters contribute the most to fluctuations in any active particle stress distributions.

For the electrolyte and separator elements, we will assume a constant Poisson ratio of $\nu = 0.45$ to symbolize a nearly incompressible material. Due to such a high value for ν, we use the B-bar method briefly discussed in Section 3.2.2 to mitigate potential volumetric mesh locking. The elastic modulus of the electrolyte will be the parameter that is perturbed in the analysis runs. Variation on the elastic modulus given $\nu = 0.45$ yields a corresponding variation on the bulk modulus $K = E/\left(3(1 - 2\nu)\right)$.

We consider two separate groups of parameters. The first set describes the electrochemical properties shown in Table 6.4 and the second set involves only mechanical properties and is listed in Table 6.5. Their calculated total Sobol indices are illustrated in Figures 6.7 and 6.9, respectively. From the results, we can see that the most pertinent electrochemical parameters are the anode and cathode diffusion coefficients, which is unsurprising as the diffusivity D directly controls the rate of lithium ion distribution. Higher values of D result in a more uniform lithium ion concentration field and mitigates stress fluctuations within the active particles.

An example of the von Mises stress distribution for a random Monte Carlo run is presented in Figure 6.8. We can see that the cathode active particles exhibit higher stress values. The anode active particles appear to have the highest fluctuation between the highest and lowest values for σ_{VM}. It is also difficult to see, but slight stress concentrations occur at the sharp edges, in which our finite element mesh is under-resolved to accurately depict these stress concentrations. For this reason, we choose to only look at the total average active particle stress.

The last analysis we conduct is a global sensitivity analysis of the mechanical properties of the anode, electrolyte, and cathode. From Table 6.5, the lithium ion swelling coefficients Ω have the highest contributions to the variance in the average particle stress. The elastic modulus of the electrolyte, anode, and cathode exhibit additional contributions on the variance of the stress as well. The elastic modulus of the electrolyte relates well to its bulk modulus, as explained above and directly affects the pressure acting on the active particles during expansion and contraction due to lithium ion intercalation. These results make valid sense, as the temperature field remains homogeneous, while the concentration field is a lot

more spatially heterogeneous in comparison.
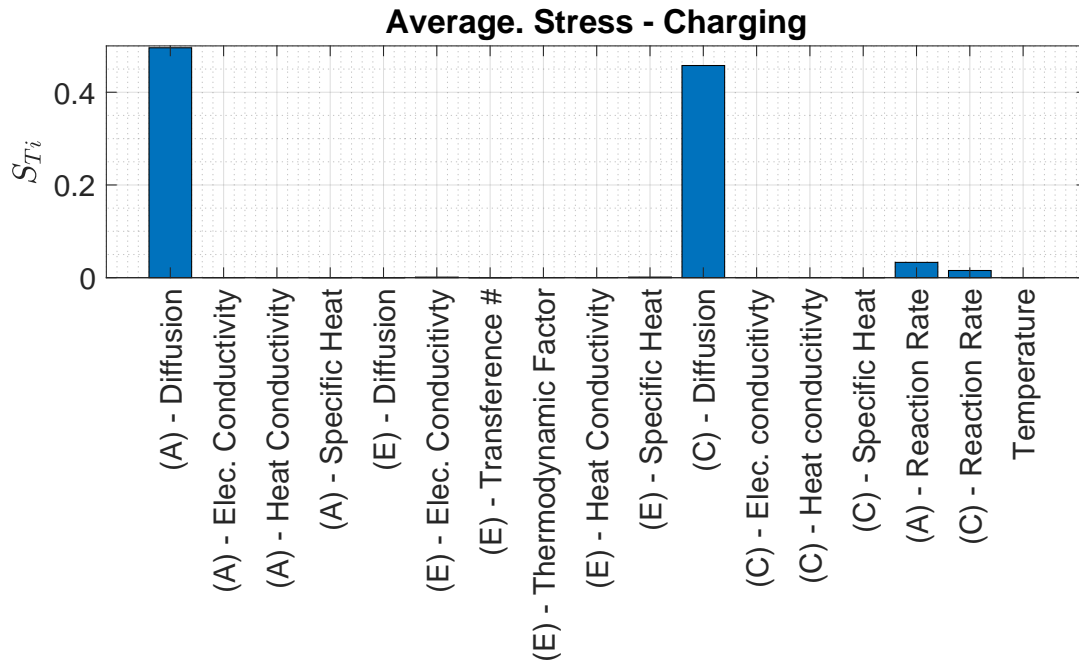
Figure 6.7: We again use $N = 12,000$ Monte Carlo iterations, the same boundary conditions, and the same material parameter ranges in Table 6.3.
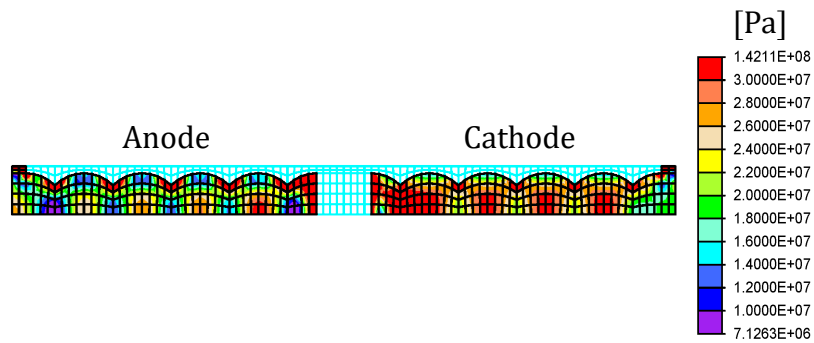
Figure 6.8: Von Mises stress distribution at the end of the charging period for a random Monte Carlo run.
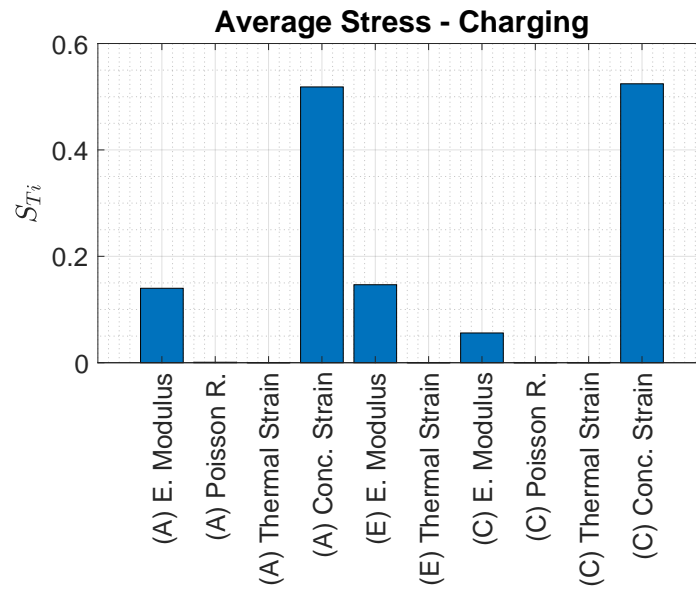
Figure 6.9: Sobol indices in variance of mechanical material properties of the electrode and electrolyte elements.

Material Parameter	Units	Range	S_{Ti}
(A) Diffusivity	m^2/s	$4 \times 10^{-13} - 6 \times 10^{-13}$	0.4959
(A) Elec. Conductivity	S/m	$145 - 155$	0.0
(A) Heat Conductivity	W/m · K	$0.8 - 1.2$	0.0
(A) Specific Heat	J/kg · K	$675 - 725$	0.0002
(E) Diffusivity	m^2/s	$2 \times 10^{-10} - 5 \times 10^{-10}$	0.0001
(E) Elec. Conductivity	S/m	$0.5 - 1.5$	0.0012
(E) Transference #	-	$0.3 - 0.4$	0.0
(E) Thermo. Factor	-	$0.35 - 0.45$	0.0
(E) Heat Conductivity	W/m · K	$0.05 - 0.15$	0.0
(E) Specific Heat	J/kg · K	$1700 - 1900$	0.0013
(C) Diffusivity	m^2/s	$4 \times 10^{-13} - 6 \times 10^{-13}$	0.4577
(C) Elec. Conductivity	S/m	$45 - 55$	0.0
(C) Heat Conductivity	W/m · K	$0.8 - 1.2$	0.0
(C) Specific Heat	J/kg · K	$675 - 725$	0.0002
(A) Reaction Rate	m$^{5/2}$/s$\sqrt{\text{mol}}$	$0.8 \times 10^{-11} - 2 \times 10^{-11}$	0.0330
(C) Reaction Rate	m$^{5/2}$/s$\sqrt{\text{mol}}$	$0.8 \times 10^{-11} - 2 \times 10^{-11}$	0.0155
Initial Temperature	K	$292.04 - 303.96$	0.0004

Table 6.4: Input ranges for the electrochemical material parameters studied on active particle von Mises stress. (A), (E), and (C) symbolize the anode, electrolyte, and cathode, respectively, and $N = 12,000$ in this analysis. The mean and standard deviation from the Monte Carlo runs are $f_0 = 24.7\,\text{MPa}$ and $\sqrt{V(y)} = 0.029\,\text{MPa}$.

Material Parameter	Units	Range	S_{Ti}
(A) Elastic Modulus	GPa	$2 - 5$	0.1399
(A) Poisson Ratio	-	$0.25 - 0.35$	0.0009
(A) Thermal Strain	1/K	$3 \times 10^{-6} - 8 \times 10^{-6}$	0.0
(A) Conc. Strain	m^3/mol	$2 \times 10^{-6} - 5 \times 10^{-6}$	0.5184
(E) Elastic Modulus	GPa	$0.9 - 2$	0.1466
(E) Thermal Strain	1/K	$0.8 \times 10^{-6} - 4 \times 10^{-6}$	0.0
(C) Elastic Modulus	GPa	$2 - 5$	0.0559
(C) Poisson Ratio	-	$0.25 - 0.35$	0.0
(C) Thermal Strain	1/K	$3 \times 10^{-6} - 8 \times 10^{-6}$	0.0
(C) Conc. Strain	m^3/mol	$1 \times 10^{-6} - 5 \times 10^{-6}$	0.5243

Table 6.5: Material property ranges for the mechanical properties studied in determining maximum and average stress response in the electrode particles. We use $N = 12,000$ in this section's analysis. We assume that the Poisson ratio $\nu = 0.45$ and intercalation strain $\beta = 0$ for the electrolyte. The mean and standard deviation from the Monte Carlo runs are $f_0 = 17.69 \, \mathrm{MPa}$ and $\sqrt{V(y)} = 5.42 \, \mathrm{MPa}$.

Chapter 7

Concluding Remarks

7.1 Summary

We have formulated the computational foundation for a complete multiphysics model for lithium ion batteries with the additional incorporation of SEI growth and lithium plating as common aging mechanisms. To our current knowledge, our model is one of the most complete simulation models currently available. We have coupled linear thermomechanical governing equations with the electrochemical governing equations used in traditional battery models. This coupling is nothing novel, but the combination of modeling unwanted side reactions in addition to lithium intercalation is not common. In addition, we have chosen to model the electrolyte and active particle materials separately to provide an in depth analysis for arbitrary geometrical layouts of a porous electrode.

In this dissertation, we have used our model to study the effect that geometrical imperfections have on stress concentrations, overpotential fluctuations, and electrode surface film growth. We have shown that small perturbations in idealized electrode particle shapes result in exasperated film growth and higher stresses. Consequently, these effects reduce the lifespan of the cell. Albeit we have only demonstrated these effects for a single particle, they correlate qualitatively well to experimental data; see Yang et al., 2017.

Moreover, we have utilized Sobol Indices as a global sensitivity method to construct an importance hierarchy for the input material properties for approximated FEM battery cell mesh. We analyzed battery discharge capacity density, maximum temperature, and average electrode particle stress. From our analyses, we have determined that the most pertinent parameters include the electrode diffusion coefficients, the active particle lithium swelling coefficients, electrode reaction rates, and initial battery cell temperature.

7.2 Limitations & Future Work

As with any computational model, there can always be improvements. Our work is lacking due to the following reasons.

1. We have implemented our model using constant material properties. Realistically, these properties are dependent on concentration and temperature values. However, the constitutive expressions for these dependencies are highly nonlinear and are applicable to a certain material fit given certain experimental data. This would be quite cumbersome to implement in the finite element method, and would then yield a very specific active particle or electrolyte user element, which we have chosen to not model.

2. The Butler-Volmer expressions for aging side reactions could have been more accurate by considering the transient consumption of the electrolyte solvent. We have implemented a decrease in reaction rate through an exponential decay factor, but we believe that a better analysis can be achieved if the electrolyte solvent surface concentration is not constant and also a function of time. Mathematically from Equation (2.79), $C_{EC}^S = \hat{C}_{EC}^S(t)$ and varies spatially along the surface of particles. This would necessitate the use of an additional history variable or independent variable to account for in the finite element code.

3. We did not consider any pressure gradient effects in the active particle. Some of the results yielded high stress concentrations near sharp edges and could have skewed our results. This phenomena is most imperative in a finite deformation setting. Moreover, mechanical pressure effects on reaction kinetics could be very crucial in a coupled mechanical and electrochemical model; see Christensen, 2005 or Cogswell and Bazant, 2012.

4. Lastly, and probably most importantly, we are computationally limited in not simulating a full battery cell at the millimeter length scale. Detailed two dimensional finite element representations of a battery microstructure were not available to us and are computationally very expensive. We had to idealize an appropriate representation in our finite element code. This is the reason for lack of comparisons to experimental data for stress magnitudes, voltage vs. capacity profiles, and surface film thicknesses. For this reason, we chose to conduct sensitivity analyses with our finite element model.

Future work would include to improve on all the limitations aforementioned. Additionally, if one has the computational power, the model can be extended to three dimensions in which finite element representations of porous electrodes are more readily seen in the literature. Further extension to accurately account for incompressible fluid motion and finite deformation mechanics would yield the most accurate stress responses within the battery cell. This would be especially useful for modeling of lithium silicon batteries. Ultimately, we hope that the model we propose can advance current research on finite element battery models and would be a useful tool for other researchers.

Bibliography

Alfaruqi, M.H. et al. (2019). "First principles calculations study of α-MnO$_2$ as a potential cathode for Al-ion battery application". In: *Journal of Materials Chemistry A* 7, pp. 26966–26974.

Armero, F. (2004). "Assumed Strain Finite Element Methods". In: Barcelona, Spain: International Centre for Numerical Methods in Engineering, pp. 46–61.

Arunachalam, H. (2017). "A New Multiscale Modeling Framework for Lithium-Ion Battery Dynamics: Theory, Experiments, and Comparative Study with the Doyle-Fuller-Newman Model". PhD thesis. Clemson University.

Autolab, Metrohm (2014a). "Galvanostatic Intermittent Titration Technique". Unpublished Note. URL: https://www.metrohm.com/en-us/applications/AN-BAT-003.

— (2014b). "Potentiostatic Intermittent Titration Technique". Unpublished Note. URL: https://www.metrohm.com/en-us/applications/AN-BAT-004.

Ayudinol, M.K. et al. (1997). "Ab initio study of lithium intercalation in metal oxides and metal dichalcogenides". In: *Physical Review B* 56.3, pp. 1354–1365.

Barai, P., K. Higa, and V. Srinivasan (2017). "Lithium dendrite growth mechanisms in polymer electrolytes and prevention strategies". In: *Physical Chemistry Chemical Physics* 19, pp. 20493–2050.

Battery University (2019). *BU-205 Types of Lithium-Ion*. URL: https://batteryuniversity.com/learn/article/types_of_lithium_ion.

Bazant, M.Z. (2012). "Theory of Chemical Kinetics and Charge Transfer based on Nonequilibrium Thermodynamics". In: *Accounts of Chemical Research* 46.5, pp. 1144–1160.

Bhattacharya, S., A. Reza Riahi, and A.T. Alpas (2014). "Thermal cycling induced capacity enhancement of graphtie anodes in lithium-ion cells". In: *Carbon* 67, pp. 592–606.

Bower, A.F. and P.R. Guduru (2012). "A simple finite element model of diffusion, finite deformation, plasticity and fracture in lithium ion insertion electrode materials". In: *Modeling and Simulation in Materials Science and Engineering* 20.4, p. 045004.

Bower, A.F., P.R. Guduru, and V.A. Sethuraman (2011). "A finite strain model of stress, diffusion, plastic flow, and electrochemical reactions in a lithium-ion half-cell". In: *Journal of the Mechanics and Physics of Solids* 59.4, pp. 804–828.

Bower, A.F. et al. (2015). "A continuum model of deformation, transport and irreversible changes in atomic structure in amorphous lithium-silicon electrodes". In: *Acta Materialia* 98, pp. 229–241.

Bucci, G., Chiang Y.M., and W.C. Carter (2016). "Formulation of the coupled electrochemical-mechanical boundary value problem, with applications to transport of multiple charged species". In: *Acta Materialia* 104, pp. 33–51.

Bucci, G. et al. (2017). "Modeling of internal mechanical failure of all-solid-state batteries during electrochemical cycling, and implications for battery design". In: *Journal of Materials Chemistry A* 5, pp. 19422–19430.

Cacuci, D.G. (2003). *Sensitivity and Uncertainty Analysis Volume I*. Chapman & Hall/CRC. ISBN: 9781584881155.

Chadwick, P. (1999). *Continuum Mechanics: Concise Theory and Problems*. Mineola, New York: Dover Publications, Inc. ISBN: 0486401804.

Christensen, J. (2005). "Failure Mechanisms in Lithium-Ion Batteries". PhD thesis. University of California, Berkeley.

Christensen, J. and J. Newman (2004). "A Mathematical Model for the Lithium-Ion Negative Electrode Solid Electrolyte Interphase". In: *Journal of the Electrochemical Society* 151.11, A1977–A1988.

Ciucci, F. and W. Lai (2011). "Derivation of Micro/Macro Lithium Battery Models". In: *Transport in Porous Media* 88, pp. 249–270.

Cogswell, D.A. and M.Z. Bazant (2012). "Coherency Strain and the Kinetics of Phase Separation in LiFePO4 Nanoparticles". In: *ACS Nano* 6.3, pp. 2215–2225.

Coleman, B. D. and W. Noll (1963). "The thermodynamics of elastic materials with heat conduction and viscosity". In: *Archive for Rational Mechanics and Analysis* 13.1, pp. 167–178.

Constantine, P. G. and A. Doostan (2017). "Time-dependent global sensitivity analysis with active subspaces for a lithium ion battery model". In: *Statistical Analysis and Data Mining* 10, pp. 243–262.

Dal, H. and C. Miehe (2015). "Computational electro-chemo-mechanics of lithium-ion battery electrodes at finite strains". In: *Computational Mechanics* 55.2, pp. 303–325.

Daniel, C. and J.O. Besenhard (2011). *Handbook of Battery Materials*. Wiley-VCH Verlag GmbH & Co. KGaA. ISBN: 978-3-527-32695-2.

Deiss, E. (2005). "Spurious chemical diffusion coefficients of Li^+ in electrode materials evaluated with GITT". In: *Electrochimica Acta* 50, pp. 2927–2932.

Deiss, E. et al. (2001). "Modeling of the charge-discharge dynamics of lithium manganese oxide electrodes for lithium-ion batteries". In: *Electrochimica Acta* 46, pp. 4185–4196.

Deng, J., G. J. Wagner, and R. P. Muller (2013). "Phase Field Modeling of Solid Electrolyte Interface Formation in Lithium Ion Batteries". In: *Journal of the Electrochemical Society* 160.3, A487–A496.

Doyle, M., T.F. Fuller, and J. Newman (1993). "Modeling of galvanostatic charge and discharge of the lithium/polymer/insertion cell". In: *Journal of the Electrochemical Society* 160.6, pp. 1526–1533.

Ecker, M. et al. (2015). "Parameterization of a Physico-Chemical Model of a Lithium-Ion Battery". In: *Journal of the Electrochemical Society* 162.9, A1836–A1848.

Edouard, C. et al. (2016). "Parameter sensitivity analysis of a simplified electrochemical and thermal model for Li-ion batteries aging". In: *Journal of Power Sources* 325, pp. 482–494.

Eringen, A. C. and G. A. Maugin (1989). *Electrodynamics of Continua I: Foundations and Solid Media*. Princeton, N.J.: Springer-Verlag. ISBN: 9781461279235.

Falconi, A. (2017). "Electrochemical Li-Ion battery modeling for electric vehicles". PhD thesis. Communaute Universite Grenoble Alpes.

Ganser, M. et al. (2019). "A finite strain electro-chemo-mechanical theory for ion transport with application to binary solid electrolytes". In: *Journal of the Mechanics and Physics of Solids* 125, pp. 681–713.

Ge, H. et al. (2017). "Investigating Lithium Plating in Lithium-Ion Batteries at Low Temperatures Using Electrochemical Model with NMR Assisted Parameterization". In: *Journal of the Electrochemical Society* 164.6, A1050–A1060.

Golmon, S., K. Maute, and M. L. Dunn (2012). "Multiscale design optimization of lithium ion batteries using adjoint sensitivity analysis". In: *International Journal for Numerical Methods in Engineering* 92, pp. 475–494.

Goodenough, J.B. and Y. Kim (2009). "Challenges for Rechargeable Li Batteries". In: *Chemistry of Materials* 22, pp. 587–603.

Grazioli, D., M. Magri, and A. Salvadori (2016). "Computational modeling of Li-ion batteries". In: *Computational Mechanics* 58, pp. 889–909.

Griffiths, D.J. (2013). *Introduction to Electrodynamics: Fourth Edition*. Pearson. ISBN: 978-0-321-85656-2.

Guan, P., L. Liu, and Y. Gao (2018). "Phase-Field Modeling of Solid Electrolyte Interphase (SEI) Cracking in Lithium Batteries". In: *ECS Transactions* 85.13, pp. 1041–1051.

Guan, P., L. Liu, and X. Lin (2015). "Simulation and Experiment on Solid Electrolyte Interphase (SEI) Morphology Evolution and Lithium-Ion Diffusion". In: *Journal of the Electrochemical Society* 162.9, A1798–A1808.

Gurtin, M.E. (1982). *An Introduction to Continuum Mechanics*. Cambridge, Massachusetts: Academic Press. ISBN: 0123097509.

Gwak, G. and H. Ju (2019). "Multi-Scale and Multi-Dimensional Thermal Modeling of Lithium-Ion Batteries". In: *Energies* 12.3, p. 374.

Hadigol, M., K. Maute, and A. Doostan (2015). "On uncertainty quantification of lithium-ion batteries: Application to an $LiC_6/LiCoO_2$ cell". In: *Journal of Power Sources* 300, pp. 507–524.

Hariharan, K. S., P. Tagade, and S. Ramachandran (2018). *Theoretical Framework of the Electrochemical Model*. Springer, Cham. ISBN: 9783319035277.

Hassoun, J. and B. Scrosati (2015). "Review – Advances in Anode and Electrolyte Materials for the Progress of Lithium-Ion and beyond Lithium-Ion Batteries". In: *Journal of the Electrochemical Society* 162.14, A2582–A2588.

Horstmann, B., F. Single, and A. Latz (2019). "Review on Multi-Scale Models of Solid-Electrolyte Interphase Formation". In: *Current Opinion in Electrochemistry* 13, pp. 61–69.

Hu, B. et al. (2017). "A chemo-mechanical model coupled with thermal effects on the hollow core-shell electrodes in lithium-ion batteries". In: *Theoretical and Applied Mechanics Letters* 7, pp. 199–206.

Hughes, T. (1980). "Generalization of selective integration procedures to anisotropic and nonlinear media". In: *Short Communications* 15.9, pp. 1413–1418.

Hughes, T. J. R. (2000). *The Finite Element Method: Linear Static and Dynamic Finite Element Analysis*. Dover Publications. ISBN: 978-0-486-41181-1.

Jansen, M. (1999). "Analysis of variance designs for model output". In: *Computer Physics Communications* 117, pp. 35–43.

Jeong, S.C. et al. (2003). "Simulation of radiotracer method for diffusion studies using short-lived radioactive nuclear beams". In: *Nuclear Instruments and Methods in Physics Research Section B* 212, pp. 483–488.

Jiao, S. et al. (2018). "Behavior of Lithium Metal Anodes under Various Capacity Utilization and High Current Density in Lithium Metal Batteries". In: *Joule* 2, pp. 110–124.

Jin, N. et al. (2017). "Parameter estimation of an electrochemistry-based lithium-ion battery model using a two-step procedure and a parameter sensitivity analysis". In: *International Journal of Energy Research* 42, pp. 2417–2430.

Jokar, A. et al. (2016). "Review of simplified Pseudo-two-Dimensional models of lithium-ion batteries". In: *Journal of Power Sources* 327, pp. 44–55.

Kindermann, F.M. et al. (2017). "A SEI Modeling Approach Distinguishing between Capacity and Power Fade". In: *Journal of the Electrochemical Society* 164.12, E287–E294.

Kovetz, A. (2000). *Electromagnetic Theory*. Great Clarendon Street, Oxford: Oxford University Press. ISBN: 0198506031.

Laresgoiti, I. et al. (2015). "Modeling mechanical degradation in lithium ion batteries during cycling: Solid electrolyte interphase fracture". In: *Journal of Power Sources* 300, pp. 112–122.

Latz, A. and J. Zausch (2011). "Thermodynamic consistent transport theory of Li-ion batteries". In: *Journal of Power Sources* 196, pp. 3296–3302.

— (2015). "Multiscale modeling of lithium ion batteries: thermal aspects". In: *Journal of Nanotechnology* 6, pp. 987–1007.

Lee, K.J., K. Smith, and G.H. Kim (Feb. 2011). *Three-Dimensional Thermal-Electrochemical Coupled Model for Spirally Wound Large-Format Lithium-Ion Batteries (Presentation)*. Golden, CO: Natioanl Renewable Energy Laboratory (NREL).

LeVeque, R. J. (2007). *Finite Difference Methods for Ordinary and Partial Differential Equations: steady-state and time-dependent problems*. Philadelphia, PA: Society for Industrial and Applied Mathematics. ISBN: 9780898716290.

Li, J. et al. (2011). "Potentiostatic Intermittent Titration Technique for Electrodes Governed by Diffusion and Interfacial Reaction". In: *The Journal of Physical Chemistry* 116, pp. 1472–1478.

Liang, L. et al. (2012). "Nonlinear phase-field model for electrode-electrolyte interface evolution". In: *Physical Review* 86, p. 051609.

Lin, N. et al. (2018). "Efficient Global Sensitivity Analysis of 3D Multiphysics Model for Li-Ion Batteries". In: *Journal of the Electrochemical Society* 165.7, A1169–A1183.

Lin, X. et al. (2013). "A Comprehensive Capacity Fade Model and Analysis for Li-Ion Batteries". In: *Journal of the Electrochemical Society* 160.10, A1701–A1710.

Liu, Q. et al. (2016). "Understanding undesirable anode lithium plating issues in lithium-ion batteries". In: *RSC Advances* 6, pp. 88683–88700.

Loveridge, M. et al. (2018). "Looking Deeper into the Galaxy (Note 7)". In: *Batteries* 4.3, p. 4010003.

Montella, C. (2002). "Discussion of the potential step method for the determination of the diffusion coefficients of guest species in host materials Part I. Influence of charge transfer kinetics and ohmic potential drop". In: *Journal of Electroanalytical Chemistry* 518, pp. 61–83.

Moura, S. J. et al. (2010). "Tradeoffs between battery energy capacity and stochastic optimal power management in plug-in hybrid electric vehicles". In: *Journal of Power Sources* 195.9, pp. 2979–2988.

Nagtegaal, J.C., D.M. Parks, and J.R. Rice (1974). "On Numerically Accurate Finite Element Solutions in the Fully Plastic Range". In: *Computer Methods in Applied Mechanics and Engineering* 4, pp. 153–177.

Newman, J. and K. E. Thomas-Alyea (2012). *Electrochemical Systems*. John Wiley & Sons. ISBN: 9780471478423.

Newman, J. and W. Tiedemann (1975). "Porous-Electrode Theory with Battery Applications". In: *AIChE Journal* 21.1, pp. 25–41.

Newman, J. and C. W. Tobias (1962). "Theoretical Analysis of Current Distribution in Porous Electrodes". In: *Journal of the Electrochemical Society* 109.12, pp. 1183–1191.

Nitta, N. et al. (2015). "Li-ion battery materials: present and future". In: *Materials Today* 18.5, pp. 252–264.

Owen, A. (2013). "Better Estimation of Small Sobol' Sensitivity Indices". In: *ACM Transactions on Modeling and Computer Simulation* 23.2, 11:1–11:17.

Pannala, S. et al. (2015). "Multiscale modeling and characterization for performance and safety of lithium-ion batteries". In: *Journal of Applied Physics* 118, p. 072017.

Park, S. et al. (2018). "Optimal Experimental Design for Parameterization of an Electrochemical Lithium-Ion Battery Model". In: *Journal of the Electrochemical Society* 165.7, A1309–A1323.

Peled, E. (1979). "The electrochemical behavior of alkali and alkaline earth metals in nonaqueous battery systems - the solid electrolyte interphase model". In: *Journal of the Electrochemical Society* 126, pp. 2047–2051.

Pinson, M. B. and M. Z. Bazant (2013). "Theory of SEI Formation in Rechargeable Batteries: Capacity Fade, Accelerated Aging and Lifetime Prediction". In: *Journal of the Electrochemical Society* 160.2, A243–A250.

Pozzi, A. et al. (2019). "Optimal Design of Experiments for a Lithium-Ion Cell: Parameters Identification of an Isothermal Single Particle Model with Electrolyte Dynamics". In: *Industrial & Engineering Chemistry Research* 58, pp. 1286–1299.

Ramadesigan, V. et al. (2010). "Optimal Porosity Distribution for Minimized Ohmic Drop across a Porous Electrode". In: *Journal of the Electrochemical Society* 157.12, A1328–A1334.

Reddy, S. R. et al. (2019). "Accerlerating parameter estimation in Doyle-Fuller-Newman model for lithium-ion batteries". In: *The International Journal for Computation and Mathematics in Electrical and Electronic Engineering* 38.5, pp. 1533–1544.

Richardson, G., G. Denuault, and C.P. Please (2012). "Multiscale modeling and analysis of lithium-ion battery charge and discharge". In: *Journal of Engineering Mathematics* 72, pp. 41–72.

Ryu, J. H. et al. (2004). "Failure Modes of Silicon Powder Negative Electrode in Lithium Secondary Batteries". In: *Electrochemical and Solid-State Letters* 7.10, A306–A309.

Safari, M. et al. (2009). "Multimodal Physics-Based Aging Model for Life Prediction of Li-Ion Batteries". In: *Journal of the Electrochemical Society* 156.3, A145–A153.

Saltelli, A. et al. (2004). *Sensitivity Analysis in Practice: A Guide to Assessing Scientific Models.* John Wiley & Sons, Ltd. ISBN: 0470870931.

Saltelli, A. et al. (2010). "Variance based sensitivity analysis of model output. Design and estimator for the total sensitivity index". In: *Computer Physics Communications* 181, pp. 259–270.

Salvadori, A., E. Bosco, and D. Grazioli (2014). "A computational homogenization approach for Li-ion battery cells: Part 1 – formulation". In: *Journal of the Mechanics and Physics of Solids* 65, pp. 114–137.

Salvadori, A., D. Grazioli, and M.G.D. Geers (2015). "Governing equations for a two-scale analysis of Li-ion battery cells". In: *International Journal of Solids and Structures* 59, pp. 90–109.

Salvadori, A. et al. (2015). "A multiscale-compatible approach in modeling ionic transport in the electrolyte of (Lithium ion) batteries". In: *Journal of Power Sources* 293, pp. 892–911.

Shi, D. et al. (2011). "Modeling stresses in the separator of a pouch lithium-ion cell". In: *Journal of Power Sources* 196, pp. 8129–8139.

Smith, R.B. and M.Z. Bazant (2017). "Multiphase Porous Electrode Theory". In: *Journal of the Electrochemical Society* 164.11, E3291–E3310.

Sobol', I.M. (2001). "Global sensitivity indices for nonlinear mathematical models and their Monte Carlo estimates". In: *Mathematics and Computers in Simulation* 55, pp. 271–280.

Taylor, R.L. and S. Govindjee (2020). *FEAP - - A Finite Element Analysis Program.* Version 8.6. University of California, Berkeley. 705 pp. August 2020.

Tiedemann, W. (2008). "Forty Years of Porous Electrode Theory with Battery Applications". In: *Journal of the Electrochemical Society* 16.13, pp. 23–37.

Tippmann, S. et al. (2014). "Low-temperature charging of lithium-ion cells Part I: Electrochemical modeling and experimental investigation of degradation behavior". In: *Journal of Power Sources* 252, pp. 305–316.

Trefethen, L. N. and D. Bau (1997). *Numerical Linear Algebra.* S.I.A.M. ISBN: 9780898713619.

Verma, A. et al. (2017). "Galvanostatic Intermittent Titration and Performance Based Analysis of LiNi$_{0.5}$Co$_{0.2}$Mn$_{0.3}$O$_2$ Cathode". In: *Journal of the Electrochemical Society* 164.13, A3380–A3392.

Verma, P., P. Maire, and P. Novák (2010). "A review of the features and analyses of the solid electrolyte interphase in Li-ion batteries". In: *Electrochimica Acta* 55, pp. 6332–6341.

Wang, A. et al. (2018). "Review on modeling of the anode solid electrolyte interphase (SEI) for lithium-ion batteries". In: *Computational Materials* 15.

Wang, S. (2016). "Entropy and heat generation of lithium cells/batteries". In: *Chinese Physical Society* 25.1, p. 010509.

Wang, Z. and K. Garikipati (2018). "A Multi-Physics Battery Model with Particle Scale Resolution of Porosity Evolution Driven by Intercalation Strain and Electrolyte Flow". In: *Journal of the Electrochemical Society* 165.11, A2421–A2438.

Wang, Z., J. Siegel, and K. Garikipati (2017). "Intercalation Driven Porosity Effects in Coupled Continuum Models for Electrical, Chemical, Thermal and Mechanical Response of Battery Electrode Materials". In: *Journal of the Electrochemical Society* 164.9, A2199–A2212.

Wen, C. J., B. A. Boukamp, and R. A. Huggins (1979). "Thermodynamic and Mass Transport Properties of LiAl". In: *Journal of the Electrochemical Society* 126.12, pp. 2258–2266.

Wen, C. J. et al. (1981). "Use of electrochemical methods to determine chemical-diffusion coefficients in alloys: application to LiAl". In: *Internation Metal Reviews* 26.1, pp. 253–268.

Weppner, W. and R. A. Huggins (1977). "Determination of the Kinetic Parameters of Mixed-Conducting Electrodes and Applications to the System Li$_3$Sb". In: *Journal of the Electochemical Society* 124, pp. 1569–1578.

Wu, B. (2019). "Modeling and Design of Lithium-Ion Batteries: Mechanics and Electrochemistry". PhD thesis. University of Michigan.

Wu, B. and W. Lu (2019). "A consistently coupled multiscale mechanical-electrochemical battery model with particle interaction and its validation". In: *Journal of the Mechanics and Physics of Solids* 125, pp. 89–111.

Yang X.G. amd Leng, Y. et al. (2017). "Modeling of lithium plating induced aging of lithium-ion batteries: Transition from linear to nonlinear aging". In: *Journal of Power Sources* 360, pp. 28–40.

Yao, N. P., L. A. Heredy, and R. C. Saunders (1971). "Emf Measurements of Electrochemically Prepared Lithium-Aluminum Alloy". In: *Journal of the Electrochemical Society* 118, pp. 1039–1042.

Ye, K.Q. (1998). "Orthogonal column Latin hypercubes and their application in computer experiments". In: *Journal of the American Statistical Association* 93.444, pp. 1430–1439.

Yurkiv, V. et al. (2018). "Phase-field modeling of solid electrolyte interface (SEI) influence on Li dendritic behavior". In: *Electrochimica Acta* 265, pp. 609–619.

Zemansky, M. W. and R. H. Dittman (1981). *Heat and Thermodynamics*. McGraw-Hill. ISBN: 0070728089.

Zhang, L. et al. (2013). "Thermal-Electrochemical Modeling and Parameter Sensitivity Analysis of Lithium-ion Battery". In: *Chemical Engineering Transactions* 33, pp. 943–948.

Zhang, X., A. Krischok, and C. Linder (2016). "A variational framework to model diffusion induced large plastic deformation and phase field fracture during initial two-phase lithiation of silicon electrodes". In: *Computer Methods in Applied Mechanics and Engineering* 312, pp. 51–77.

Zhao, Y. et al. (2019). "A review on modeling of electro-chemo-mechanics in lithium-ion batteries". In: *Journal of Power Sources* 413, pp. 259–283.

Zienkiewicz, O.C., R.L. Taylor, and J.Z. Zhu (2013). *The Finite Element Method: Its Basis and Fundamentals*. Burlington, MA: Elsevier Butterworth-Heinemann. ISBN: 9781856176330.